

Applications of Cone Beam Computed Tomography in Radiotherapy Treatment Planning

Kavitha Srinivasan



Thesis submitted for the degree of
Master of Philosophy (Science)
in the School of Chemistry and Physics
University of Adelaide

Supervisors:

Dr. Judith Pollard

Dr. Mohammad Mohammadi

Dr. Justin Shepherd

July 2014

Table of Contents

List of Figures.....	6
List of Tables.....	9
List of Abbreviations.....	10
I. Abstract.....	12
II. Declaration.....	14
III. Acknowledgements.....	16
IV. Publications.....	17
Chapter 1.....	18
Introduction.....	18
1.1 Background.....	18
1.2 Aims of the Current Thesis.....	18
1.3 Thesis Overview.....	19
Chapter 2.....	22
Current Status of CBCT in Radiotherapy.....	22
2.1 Cone beam Computed Tomography.....	22
2.2 Linac-mounted CBCT Devices.....	23
2.3 CBCT Components.....	23
2.3.1 CBCT Hardware.....	23
2.3.2 CBCT Software.....	26
2.4 CBCT Applications in Radiotherapy.....	29
2.4.1 CBCT for Image-guided Radiotherapy.....	30
2.4.2 CBCT for Adaptive Radiotherapy.....	32
2.5 Concerns in CBCT.....	33
2.5.1 Artefacts: Causes and Solutions.....	33
2.5.2 Image Quality.....	43
2.5.3 Dose Accumulation.....	44
2.6 Conclusions.....	47

Chapter 3	48
Comparison and Evaluation of PCT and CBCT Dose Distribution	48
3.1 Introduction	48
3.2 Materials	49
3.2.1 Varian OBI	49
3.2.2 Philips PCT.....	50
3.2.3 Treatment Planning Systems	52
3.2.4 Phantoms and Patients	52
3.3 HU Calibration	53
3.3.1 Method.....	53
3.3.2 HU Calibration Results.....	54
3.4 HU Profiles	55
3.4.1 Method.....	55
3.4.2 HU Profile Results.....	55
3.5 Dose Calculations and Evaluations	58
3.5.1 Method.....	58
3.5.2 Dose Calculations Results	58
3.6 Conclusions	65
Chapter 4	66
Investigation of Effect of Reconstruction Filters on Cone-Beam Computed Tomography	
Image Quality	66
4.1 Introduction	66
4.2 Catphan.....	67
4.3 Method of Acquisition.....	68
4.4 Procedure for Analysis	68
4.4.1 Pixel Stability	69
4.4.2 HU Uniformity	69
4.4.3 Contrast-to-Noise Ratio.....	70
4.4.4 Spatial Resolution.....	71
4.5 Results	71
4.5.1 Pixel Stability	71
4.5.2 HU Uniformity	71

4.5.3 Contrast-to-Noise Ratio.....	77
4.5.4 Spatial Resolution.....	77
4.6 Discussion and conclusion	80
Chapter 5.....	84
Implementation of the CBCT Image Reconstruction Algorithm	84
5.1 Introduction	84
5.2 Cone-Beam Data Acquisition and Pre-processing	84
5.2.1 Projection Data Acquisition.....	84
5.2.2 Normalisation of Projections	85
5.2.3 Calculation of Weighting Factors.....	86
5.2.4 Wiener2 – Two-dimensional Adaptive Filter.....	88
5.3 Cone-beam Reconstruction Algorithm.....	89
5.3.1 Implementation of 3D Cone-beam Reconstruction – FDK Algorithm	89
5.3.2 Creation of C++ MEX files	90
5.3.3 Hounsfield Unit Calibration	91
5.3.4 Summary of 3D Image Reconstruction Procedure.....	93
5.4 Discussion of Image Reconstruction	94
5.5 Conclusion.....	96
Chapter 6.....	98
Analysis of Cone-beam Rando Images Reconstructed using In-house Software	98
6.1 Introduction	98
6.2 Image Reconstruction.....	98
6.2.1 Rando Phantom	98
6.2.2 Reconstructed Rando Images	99
6.3 Radiotherapy Treatment Planning.....	100
6.3.1 Treatment Technique.....	100
6.3.2 Treatment Optimisation Parameters	102
6.3.3 Treatment Planning Parameters.....	102
6.3.4 Dose Calculation Algorithm.....	103
6.3.5 Treatment Plan Evaluation	106
6.4 Planning Results	107
6.5 Conclusion.....	112

Chapter 7	114
Iterative Reconstruction for Cone-beam.....	114
7.1 Iterative Reconstruction-Overview	114
7.2 Maximum-Likelihood Algorithm.....	115
7.3 Implementation of the OSEM Iterative Reconstruction Algorithm	117
7.4 Experimental Methods.....	118
7.4.1 Image Acquisition and Pre-processing.....	118
7.4.2 Distance Dependent Resolution (DDR) Corrections.....	119
7.4.3 Simple Transmission OSEM	121
7.4.4 Centre of Rotation (COR) Offset.....	122
7.5 Practical Applications of OSEM and Results.....	123
7.6 Discussion.....	127
Chapter 8	130
Conclusions	130
8.1 Summary and Conclusions	130
8.1.1 Current Status of Varian OBI-based Treatment Planning	130
8.1.2 Effect of Reconstruction Filters on CBCT Image Quality	131
8.1.3 CBCT Image Reconstruction Algorithm Development	131
8.1.4 Investigation of In-house Reconstructed Images for Treatment Planning	132
8.1.5 Iterative-based CBCT Reconstruction.....	132
8.2 Future Work.....	132
References	134
Appendix A Matlab Codes	144
Appendix B C++ Codes.....	152
Published Papers.....	145

List of Figures

Figure 2.1 Schematic view of CBCT geometry	22
Figure 2.2 Cone-beam systems mounted on medical linacs: (a) Varian OBI Imaging system (b) Elekta XVI system (c) Siemens MVision and (d) Mitsubishi VERO system.....	24
Figure 2.3 Bow-Tie filters used in (a) Varian OBI (Ding et al. 2007) (b) Elekta XVI.....	25
Figure 2.4 Flat-panel detector construction using a-silicon TFTs array.....	26
Figure 2.5 Geometric coordinates of CBCT scan with flat-panel detector	28
Figure 2.6 Procedures in a CBCT system.....	29
Figure 2.7 (a) Concentric rings (arrows) around the axis of rotation in the CBCT image, (b) fan-beam CT image without ring artefact	34
Figure 2.8 (a) a dark smudge (arrows) at the centre of the homogeneous phantom due to cupping artefact, (b) CBCT image of density phantom showing dark streaks (see arrows) around high density inserts and (c) fan-beam CT image of density phantom without streaks.....	40
Figure 2.9 (a) Blurring induced by breathing motion, (b) streaks induced from the movement of bowel gas and (c) double contours induced by patient movement during cone-beam acquisition process.....	41
Figure 2.10 (a) Typical aliasing patterns (arrows) in CBCT datasets; (b) without aliasing in fan-beam CT image.....	42
Figure 2.11 (a) Opposing dark and bright crescents seen on CBCT datasets of Catphan and (b) fan-beam image of Catphan without crescent artefacts.....	43
Figure 3.1 Varian Clinac iX unit with OBI, Varian Medical system	50
Figure 3.2 Philips CT scanner, Philips Medical system.....	51
Figure 3.3 Calibration curves for PCT and CBCT	54
Figure 3.4 CBCT scanning of phantom along Z-axis.....	56
Figure 3.5 Cone-beam HU profiles of (a) Water phantom, (b) Norm head phantom and (c) Norm body phantom along Z-axis	57
Figure 3.6 Cone-beam HU dependence on phantom dimensions along thickness (L) and diameter (D) of phantom	57

Figure 3.7 Dose distributions on an axial slice of Catphan acquired using PCT (a1) and CBCT using curve2 (a2); on an axial slice of Norm body phantom acquired using PCT (b1) and CBCT using curve2 (b2).....	60
Figure 3.8 DVHs comparison of the PTV for (a) Density phantom, (b) Water phantom, (c) Catphan and (d) Norm body phantom obtained with PCT, CBCT using density calibration curve (curve 1) and by using Catphan calibration curve (curve 2).....	61
Figure 3.9 Comparison of PCT and CBCT dose distributions and dose profiles using gamma map for (a) Catphan and (b) Norm body phantom using Catphan calibration curve 2.....	62
Figure 3.10 Dose distributions on an axial slice of patient A (a1 and a2) and patient B (b1 and b2) prostate cases using PCT and CBCT respectively.....	63
Figure 3.11 DVHs comparison of the PTV and Femoral head for two prostate patients (a) Patient A and (b) Patient B, obtained with PCT, CBCT using density calibration curve (curve 1) and using Catphan calibration curve (curve 2).....	63
Figure 3.12a Dose distribution, gamma map and dose profile comparisons for patient A using MapCHECK.....	64
Figure 3.12b Dose distribution, gamma map and dose profile comparisons for patient B using MapCHECK.....	64
Figure 4.1 Illustration of Catphan® 504 phantom.....	67
Figure 4.2 Frequency response curves for various reconstruction filters.....	69
Figure 4.3 Image of CTP 486 module of Catphan with ROIs drawn.....	70
Figure 4.4 Central profiles of reconstructed axial slices for full- and half-fan mode using Ram-Lak filter.....	76
Figure 4.5 CTP 404 slice of Catphan reconstructed for full- fan (a and b) and half-fan (c and d) modes using Ram-Lak (a and c) filter and Hamming filter (b and d).....	77
Figure 4.6 CTP 528 slice of Catphan reconstructed using (a) Ram-Lak, (b) Hamming (c) Shepp-Logan, (d) Cosine and (e) Hann filters showing the number of line pairs seen. ..	79
Figure 4.7 MTF calculated for (a) half-fan mode and (b) full-fan mode.....	80
Figure 4.8 Flowchart providing guideline to choose the reconstruction filter.....	81
Figure 5.1 Typical I0 calibration data (1024 × 768) for full-fan mode with bow-tie filter taken on a Clinac iX unit.....	86
Figure 5.2 scanning geometry utilized for fan-beam.....	87
Figure 5.3 An axial attenuation coefficient image of the CTP404 module of the Catphan 504 phantom obtained from in-house reconstruction used for HU calibration.....	92

Figure 5.4 HU calibration curve for CBCT of Catphan in full-fan mode	92
Figure 5.5 Reconstructed axial slices of Catphan in insert and line pair modules (top) and the same slices reconstructed by Varian software (bottom).....	93
Figure 5.6 MTF calculated using Droege’s method for Varian and in-house reconstructed images.....	95
Figure 6.1 (a) Rando male phantom and (b) its sections.....	99
Figure 6.2 Reconstructed axial slices from head and neck regions of Rando using Varian software (top) and in-house (bottom).....	101
Figure 6.3 Schematic diagram of IMRT treatment planning process.....	102
Figure 6.4 IMRT parameters window from Pinnacle TPS.....	103
Figure 6.5 IMRT dose distributions computed on planning CT images in axial, sagittal and coronal slices	108
Figure 6.6 IMRT dose distributions computed on Varian CBCT images in axial, sagittal and coronal slices	109
Figure 6.7 IMRT dose distributions computed on in-house reconstructed CBCT images in axial, sagittal and coronal slices.....	110
Figure 6.8 The planar dose maps from (a) PCT, (b) in-house reconstructed CBCT are compared to produce (c) Gamma dose map showing failed points in blue colour and (d) profiles generated across x-axis of the planar dose maps (black line- PCT; yellow circles- CBCT)	111
Figure 7.1 Catphan@504 phantom used for CBCT scans	119
Figure 7.2 Cone-beam projection of a thin wire seen on IDL program	120
Figure 7.3 FWHM for the flat-panel detector as a function of distance between source and detector.....	121
Figure 7.4 Transmission- and emission-based geometries.....	122
Figure 7.5 (a) Blade calibration plate and (b) setup	123
Figure 7.6 Catphan projection displayed using IDL program.....	123
Figure 7.7 Reconstructed axial slices of high contrast section of Catphan (containing line pairs) with DDR and COR corrections	127
Figure 7.8 Reconstructed axial slice of high contrast section of Catphan (containing line pairs) with scatter correction	128
Figure 7.9 FDK-based reconstruction of high contrast section of Catphan (containing line pairs).....	129

List of Tables

Table 2.1 Source specifications of gantry-mounted CBCT devices.....	25
Table 2.2 List of studies on dosimetric investigation of CBCT	36
Table 2.3 CBCT dose studies based on Varian OBI and Elekta XVI.....	46
Table 3.1 Image acquisition parameters for CBCT and PCT for head and body scans	51
Table 3.2 Dimensions of phantoms used for this study.....	52
Table 4.1 Insert materials present in Catphan CTP 404 modules and their expected and measured HU values.....	72
Table 4.2 Uniformity Index measurements on a reconstructed slice of Catphan using five different filters in full- and half-fan modes.....	76
Table 4.3 Summary of contrast-to-noise (CNR) measurements for (a) half-fan and (b) full-fan acquisition mode of CBCT using five different filters.....	78
Table 4.4 Summary of the MTF measurement for (a) half-fan and (b) full-fan CBCT imaging protocol using five different reconstruction filters. The frequencies corresponding to MTF values of 0.5 and 0.1 are shown.....	79
Table 5.1 Default calibrated Varian CBCT full-fan mode summarising the scan and reconstruction parameters	85
Table 5.2 Nominal and measured HU values for sensitometry inserts in the CTP404 module of the Catphan 504 phantom and their relative density.....	91
Table 6.1 CBCT scan and reconstruction parameters	100
Table 6.2 IMRT plan summary for Rando PCT and CBCT scans	104
Table 7.1 FWHM measurements of a thin wire at various distances from the detector	121
Table 7.2 Interfile header created to feed into OSEM algorithm	125

List of Abbreviations

ACA: Adaptive Convolution Algorithm
ART: Adaptive Radiotherapy
CBCT: Cone Beam Computed Tomography
CNR: Contrast-to-Noise Ratio
COR: Centre of Rotation
CPU: Central Processing Unit
3D-CRT: Three- dimensional Conformal Radiotherapy
CT: Computed Tomography
CTV: Clinical Target Volume
DDR: Distance Dependent Resolution
DICOM: Digital Imaging and Communications in Medicine
DMPO: Direct Machine Parameter Optimisation
DVH: Dose Volume Histogram
DQE: Detective Quantum Efficiency
2D: Two-dimensional
3D: Three-dimensional
FBP: Filtered Back Projection
FDK: Feldkamp Davis Kress
FOV: Field of View
FPI: Flat-Panel Imager
fps: frames per second
FWHM: Full-Width at Half Maximum
GPU: Graphical Processing Unit
H&N: Head and Neck
HU: Hounsfield Unit
IGRT: Image-Guided Radiotherapy
IMRT: Intensity Modulated Radiotherapy
IQ: Image Quality
kVp: Peak kilovoltage
lp/cm: line pair /centimetre

mAs: milli-ampere second
MEX: Matlab Executable
MLC: Multi leaf Collimator
MLEM: Maximum-Likelihood Expectation-Maximisation
MRI: Magnetic Resonance Imaging
MTF: Modulation Transfer Function
MU: Monitor Unit
OAR: Organs at Risk
OBI: On-Board Imager
OSEM: Ordered Subset Expectation Maximisation
PCT: Planning Computed Tomography
PET: Positron Emission Tomography
PTV: Planning Target Volume
QA: Quality Assurance
ROI: Region of Interest
SAD: Source-to-Axis Distance
SBRT: Stereotactic Body Radiotherapy
SD: Standard Deviation
SDD: Source-to-Detector Distance
SNR: Signal-to-Noise Ratio
SPECT: Single Photon Emission Computed Tomography
SSD: Source-to-Surface Distance
TFT: Thin-Film Transistor
TPS: Treatment Planning Systems

I. Abstract

In recent years Image-Guided Radiotherapy (IGRT) has experienced many technical advances. One of the most significant has been the widespread implementation of kilovoltage imagers attached to the gantry of linear accelerators (LINACs); these units are capable of 2D planar imaging, fluoroscopy and 3D Cone Beam Computed Tomography (CBCT) imaging. With CBCT imaging, the treatment plan can be modified based on patient's anatomy just before the treatment session. This method of Adaptive Radiotherapy (ART) helps in managing a patient's treatment by compensating for the effect of daily setup variation and changes to the tumour during the course of radiotherapy. Currently the image quality of CBCT is sufficient for patient set-up verification; however the use of CBCT for dose calculations requires reproducible CT numbers in order to be used effectively during ART. The aim of this project was to investigate methods to improve the image quality of CBCT datasets in order to facilitate their use in dosimetric calculations.

The project was divided into two major parts. In the first part, the conventional Feldkamp-Davis-Kress (FDK) cone-beam reconstruction algorithm was implemented in Matlab. The algorithm was then modified using weighting factors for data redundancy and for non-equal cone angles. A 2D adaptive filter was used to remove noise and to compensate for the loss of resolution. A modified in-house reconstruction algorithm was developed and the image quality obtained was comparable to reconstructed images obtained using the Varian OBI system software. The images are free of crescent artifacts and showed a maximum spatial resolution of 7 line pairs/cm. The effect of different reconstruction filters on CBCT image quality was also studied and guidelines were produced for different anatomical sites to assist in choosing appropriate filters to achieve optimal reconstructed image quality.

In the next part of the research, a comparative study between Varian and in-house reconstructed images was performed using Planning CT (PCT) images as a reference dataset. The feasibility of using the Varian and in-house reconstructed images for treatment planning was investigated by acquiring CBCT images of the Rando anthropomorphic phantom. An Intensity-Modulated Radiotherapy (IMRT) treatment plan was generated using both sets of reconstructed images using the Pinnacle³ treatment planning system.

Planar dose distributions were extracted from both the datasets in order to evaluate dose distributions quantitatively based on 3%/3mm Gamma analysis criteria. These distributions were then compared against the reference PCT image and it was found that in-house reconstructed images showed good agreement with the PCT images with a gamma passing rate of 99.8%. Although several pre-processing steps performed on the Varian images were not included during in-house reconstruction, the results demonstrated the potential for use of in-house reconstructed CBCT image for treatment planning.

As an alternative to FDK reconstruction, iterative reconstruction using Maximum Likelihood solutions was also investigated. Since the Ordered Subsets Expectation Maximisation (OSEM) package used in this study is intended for fan-beam geometry, only the slices from the central plane of cone-beam were chosen. The projections were corrected for distance-dependent resolution and centre of rotation offset. When the number of iterations was increased to 16, the algorithm converges well and showed more uniform images. However, the images were not comparable to FDK-based images due to the intrinsic difference in data handling. The OSEM program was developed initially for emission-based measurements and did not model the scatter component effectively for transmission-based measurements. Including the scatter component more effectively may make it more realistic for CBCT geometry.

II. Declaration

I certify that this work contains no material which has been accepted for the award of any other degree or diploma in my name, in any university or other tertiary institution and, to the best of my knowledge and belief, contains no material previously published or written by another person, except where due reference has been made in the text. In addition, I certify that no part of this work will, in the future, be used in a submission in my name, for any other degree or diploma in any university or other tertiary institution without the prior approval of the University of Adelaide and where applicable, any partner institution responsible for the joint-award of this degree.

I give consent to this copy of my thesis when deposited in the University Library, being made available for loan and photocopying, subject to the provisions of the Copyright Act 1968.

The author acknowledges that copyright of published works contained within this thesis resides with the copyright holder(s) of those works.

I also give permission for the digital version of my thesis to be made available on the web, via the University's digital research repository, the Library Search and also through web search engines, unless permission has been granted by the University to restrict access for a period of time.

Signature:

Date:

III. Acknowledgements

Many people have helped me along the way to this thesis and I am pleased to express my appreciation here. I wish to acknowledge the Australian Postgraduate Award/scholarship from Australian government, which made this project possible.

I am extremely grateful to my supervisors, Mohammad Mohammadi, Justin Shepherd and Judith Pollard who have always provided encouragement, guidance and good advice throughout my time here at Royal Adelaide Hospital and the University of Adelaide, and especially on this thesis project.

Next, I received invaluable assistance from the staff of the Medical Physics department at the Royal Adelaide Hospital: Raelene Nelligan, Scott Penfold, Kim Quach, Daniel Ramm and John Lawson. They taught me the operations and the functions of linac machines, and were always there to help when the unexpected happened. Among the physicists, Justin Shepherd helped me in understanding and working of Pinnacle treatment planning system and in the image management (ARIA®) issues.

I would like to thank Joshua Moores for sharing his knowledge of CBCT with me. I would also like to express my gratitude to the chief of Medical Physics department, Dr. Eva Bezak for her valuable advices over the course of my project work. My sincere thanks go to Leighton Barden and Daniel Badger for their invaluable assistance in using the iterative reconstruction software available at the Queen Elizabeth hospital.

My special thanks to Ramona Adorjan from University of Adelaide who helped in installing software and solving many technical problems that I came across. My friendship with my fellow research students has made it a pleasant place to study and work during my candidature. I would like to thank the University of Adelaide and Australasian College of Physical Scientists and Engineers for providing me the fund to attend the EPSM conference held in Darwin (2011) and EPI2k12 conference (2012) held in Sydney.

My final thanks, as always, go to my family, whose love and support are so important to me.

IV. Publications

Journal Papers

1. Srinivasan, K, Mohammadi, M, Shepherd, J 2014, 'Applications of linac-mounted kilovoltage cone-beam computed tomography in modern radiation therapy: A review', *Polish Journal of Radiology*, vol. 79, pp. 181-193.
2. Srinivasan, K, Mohammadi, M, Shepherd, J 2014, 'Cone Beam Computed Tomography for adaptive radiotherapy treatment planning', *Journal of Medical and Biological Engineering*, vol. 34(4), pp. 377-385.
3. Srinivasan, K, Mohammadi, M, Shepherd, J 2014, 'Investigation of effect of reconstruction filters on cone-beam computed tomography image quality', *Australasian Physical & Engineering Sciences in Medicine*, vol. 37, pp. 607-614.

Conference Presentations

1. Use of Cone Beam Computed Tomography for Radiotherapy Treatment Planning, EPSM 2011, held in Darwin.
2. Varian CBCT for Adaptive Radiotherapy Tasks, EPI2k12, held in Sydney, March 2012.
3. Investigation of effect of reconstruction filters on image noise and resolution in Varian Cone-beam Computed Tomography, EPSM 2012, held in Gold coast, 2012.

Chapter 1

Introduction

1.1 Background

The aim of radiotherapy is to maximize damage to the tumour while minimizing damage to normal tissues. Identification of the tumour volume is a challenging issue in radiotherapy. In order to ensure precise dose delivery to the tumour volume, the target volume delineated during the treatment planning should be reduced to spare normal tissues and to enable dose escalation. However, this demands accurate imaging. As a golden standard, Computed Tomography (CT) images are used for treatment planning (hence the term planning CT or PCT). These images provide us with anatomical information that helps in localizing the tumour volume precisely. Though CT-based planning is accurate for treatment, it is restricted by changes to the patient during the course of treatment e.g. weight loss, tumour shrinkage. Hence, a technique that accounts for these changes during the radiotherapy course is required. Adaptive Radiotherapy (ART) is a technique that can successfully account for these patient changes by re-optimizing the plan during treatment. Using this technique, any dosimetric variations can be corrected during replanning and thereby the prescribed dose can be delivered to the target volume more precisely and uniformly. In order to achieve the accuracy of dose delivery, imaging devices are essential in the therapy room (in-room) to reduce patient set-up errors and to track tumour margins. Hence an x-ray image guidance tool, Cone- Beam Computed Tomography (CBCT), is designed and attached to a linear accelerator for patient set-up verification. This study mainly focuses on the use of CBCT for radiotherapy treatment planning by improving image quality.

1.2 Aims of the Current Thesis

This study used the Varian Clinac iX unit with CBCT capability available in the Royal Adelaide Hospital. The primary objectives of this thesis were as follows:

- To provide a detailed investigation of available CBCT images for applications in radiotherapy treatment planning and to quantify the percentage of dose difference when comparing it to dose calculated on PCT images

- To develop and implement a modified three-dimensional cone-beam reconstruction algorithm that minimises CBCT artefacts and improves CBCT image quality
- To assess the effects of reconstruction filters on CBCT datasets in order to provide an optimal image quality without increasing the dose to patients
- To evaluate the modified in-house algorithm on CBCT projections of the Catphan and Rando phantoms
- To measure and compare the dose distributions calculated on reconstructed CBCT images of Rando to that of PCT images of Rando.

1.3 Thesis Overview

Chapter 1 outlines the main aims and structure of this thesis.

Chapter 2 reviews the design, structural components of CBCT, hardware and software, and its applications in modern radiotherapy. The major concerns in CBCT such as artefacts, image quality and dose are discussed.

Chapter 3 presents an evaluation of the treatment plans obtained from Varian CBCT datasets. The feasibility of CBCT for radiotherapy treatment planning has been investigated and the study extended to clinical situations is included. This helps in assessing the base line performance of CBCT compared to a conventional fan-beam PCT.

Chapter 4 investigates the effect of reconstruction filters on cone-beam image quality in order to provide an optimal image quality based on the anatomical region. Based on these findings, a set of guidelines has been developed to select the most suitable reconstruction filter for a given region of interest.

Chapter 5 describes the procedure adopted to implement and modify the cone-beam reconstruction algorithm that has been used in this project. Acquisition, processing and reconstruction of cone-beam projections of Catphan are explained in detail.

Chapter 6 deals with the clinical approaches of the developed algorithm using Rando phantom scans. The cone-beam projections of the Rando head portion were acquired in full-fan mode with bow-tie filters. The projections were then pre-processed by applying weighting factors for incomplete datasets and for non-equal cone angles. Then a low-pass adaptive filter was used to filter the high frequency components of the image. The in-house developed FDK algorithm was used to reconstruct the Rando datasets. Further the reconstructed images were utilized for dose calculations and the dose distributions were evaluated using MapCHECK™ software.

Chapter 7 discusses iterative-based CBCT reconstruction technique using Maximum-likelihood solution. The scans were acquired after positioning Catphan to yield projections of the section of interest at the central plane which have fan-beam properties. The projections were pre-processed and corrections for distance dependent resolution, centre of rotation offset and transmission-based scatter were incorporated into the OSEM algorithm to achieve the best estimate of the true object.

Chapter 8 summarizes the findings of this thesis and gives a general discussion with respect to the benefits and limitations of the method presented.

Chapter 2

Current Status of CBCT in Radiotherapy

The use of CBCT in radiotherapy is increasing due to the widespread implementation of kilovoltage systems on currently available linear accelerators. Kilovoltage imagers for improved patient set-up are now commonly used to perform CBCT scans for three-dimensional (3D) matching.

2.1 Cone beam Computed Tomography

Cone-beam CT is an Image-guided Radiotherapy (IGRT) tool to manage patient set-up and tumour motion in order to reduce field margins and to optimise the treatment plan. CBCT was first commercially available for dentomaxillofacial imaging in 2001. The term “cone-beam” refers to the cone-shaped x-ray beam from the source (Figure 2.1) which covers the entire field of view in a single rotation around the patient. The transmitted x-rays are detected by a 2D detector called flat-panel imager (FPI). The 2D projections acquired from CBCT are reconstructed to enable volumetric imaging of the patient.

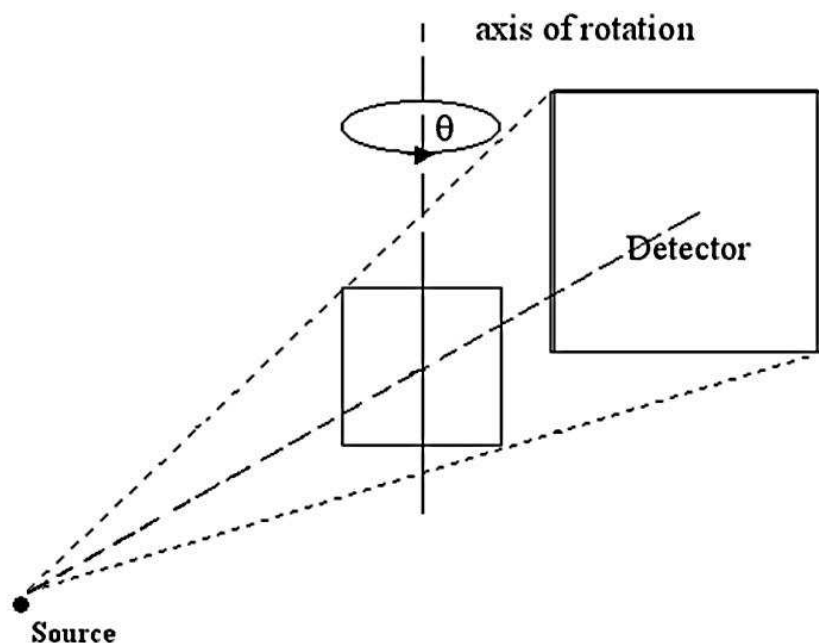


Figure 2.1 Schematic view of CBCT geometry

2.2 Linac-mounted CBCT Devices

At present, there are three gantry-mounted cone-beam devices available. They are the Varian On Board Imager (OBI) (Varian Medical Systems, USA), Elekta XVI (Elekta Oncology Systems, UK) and Siemens MVision (Siemens Medical solutions, Germany) (Figure 2.2 a, b & c respectively). The Varian and Elekta systems are kV-CBCT imaging modalities (30-140 kV), in which the kV x-ray source (kVS) and a kV detector (kVD) are attached to the linac gantry at a 90° offset from the treatment beam. Siemens has developed both kilovoltage cone-beam (kVision™) and megavoltage cone-beam imaging tools (MVision) (1-6 MV) for patient position verification and adjustments. MVision megavoltage cone-beam imaging uses the same source as the treatment beam for 3D target imaging. A more recent device developed for image-guided stereotactic body radiation therapy (SBRT) is the MHI-TM2000/VERO system (Figure 2.2d), a joint product of MHI (Mitsubishi Heavy Industries Ltd., Tokyo, Japan) and BrainLAB (BrainLAB AG, Feldkirchen, Germany). It utilizes a rotating, rigid ring structure to integrate a beam delivery platform and image guidance system. The Vero system uses kV-CBCT registration and optical tracking of infrared reflective markers in order to locate and correct the patient position before and during treatment.

Images produced by kV-CBCT show superior high contrast resolution compared to MV devices due to the importance of the photoelectric effect (dependence on atomic number Z to the power 3-4) at kV energies. At MV energies, since the dominant interaction is Compton scattering (inversely proportional to the photon energy and nearly independent of the atomic number Z) the image contrast is reduced for tissue equivalent materials. To further understand the advantages, disadvantages and practical considerations of CBCT in radiotherapy, the hardware and the software components of CBCT are reviewed below. As this study used Varian Clinac iX, the majority of the description is based on Varian OBI unless otherwise specified.

2.3 CBCT Components

2.3.1 CBCT Hardware

(i) X-ray Source

The x-ray source is either kilovoltage (30-140 kV) or megavoltage (1-6 MV). The various attributes of CBCT such as the field size, the target angle and the focal spot size depend

upon the x-ray tube design. The Varian OBI has an oil-cooled rotating anode x-ray tube with 14° target angle and two focal spot sizes (0.4 mm and 0.8 mm). Once the beam exits the window, it is modified first by a fixed primary collimator and then by two pairs of movable lead blades which adjust the field size. In addition, Varian uses two specially designed aluminium filters called full- and half-bow-tie filters (Figure 2.3a) that equalise the x-ray intensity laterally across the detector for two different modes of acquisition (full-fan and half-fan).

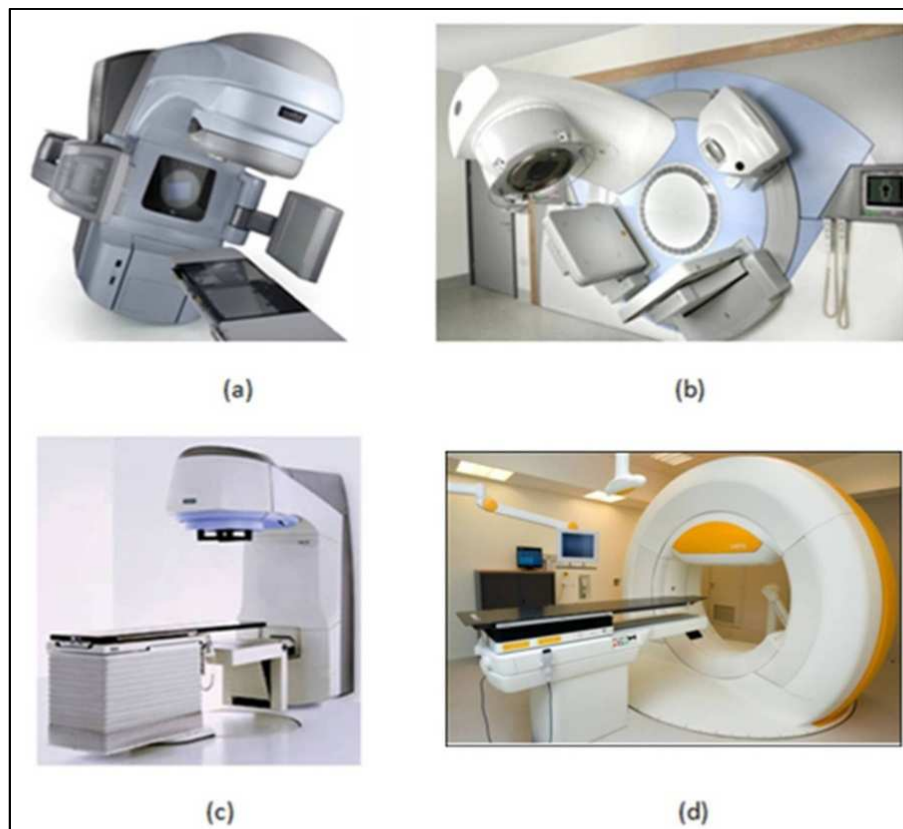


Figure 2.2 Cone-beam systems mounted on medical linacs: (a) Varian OBI Imaging system (courtesy and Copyright ©2007, Varian Medical systems, Inc); (b) Elekta XVI system (courtesy and Copyright© 2008, Elekta AB (publ)); (c) Siemens MVision (courtesy and Copyright© Siemens AG, 2002-2008) and (d) Mitsubishi VERO system (courtesy and Copyright MHI Ltd., Tokyo, Japan)

The Elekta kV source is a fan-cooled x-ray tube which can be positioned at three different field of view (FOV) positions, namely, S (small FOV), M (medium FOV) and L (Large FOV). The Elekta bow-tie filter (Figure 2.3b) is inserted between the source and the patient to reduce intensity variations across the detector. Siemens MVision utilizes the treatment beam from a conventional linac and obtains an accurate representation of the patient in the

treatment position using an electronic portal imager. Table 2.1 shows the standard geometric specifications of three linac-mounted CBCT devices where the source to axis distance (SAD = 100 cm) is constant.

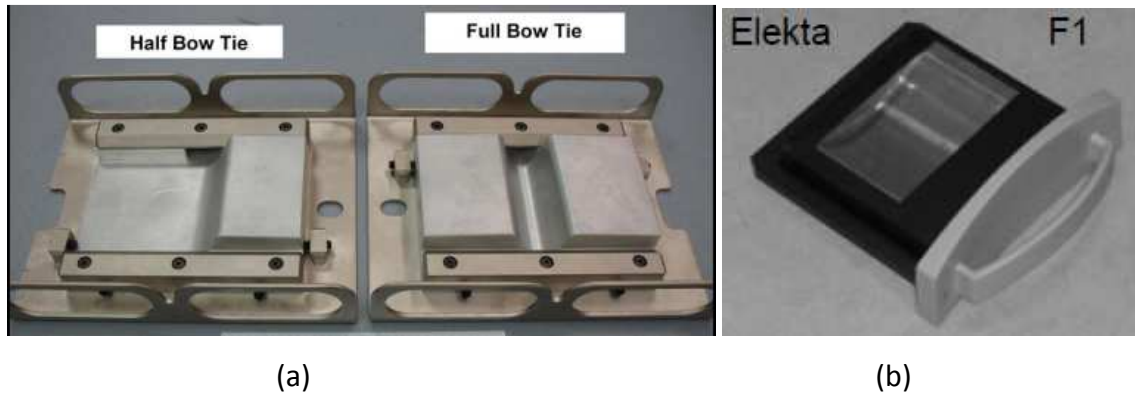


Figure 2.3 Bow-Tie filters used in (a) Varian OBI (Ding et al. 2007) (b) Elekta XVI

Table 2.1 Source specifications of gantry-mounted CBCT devices

CBCT devices	Varian OBI	Elekta XVI	Siemens MVision
Source angle with respect to treatment beam	90°	90°	180°
Source to detector distance (SDD) (cm)	150	153.6	145
Tube voltage	30-140 kVp	70-150 kVp	6 MV
Exposure per projection (mAs)	2*	0.1-3.2	--

*read-only value, depends on current settings on mA, ms and kV

(ii) Flat-Panel Imager

The flat-panel imager technology used in CBCT was first investigated by Jaffray and Siewerdsen (2000). This technology is based upon fabricating a 2D matrix of hydrogenated amorphous silicon (a-Si) thin-film transistors (TFTs) on a large area of scintillating material (Thallium doped Caesium Iodide). Such systems (Figure 2.4) demonstrate excellent optical coupling efficiency (the efficiency of converting light photons to

electrical signals) and hence improved imaging is possible with high optical absorption, high uniformity over a large area and high Detective Quantum Efficiency (DQE) of ~60%. The Varian imaging system has 2048×1536 pixels, for a total physical size of $39.73 \times 29.80 \text{ cm}^2$. The system also has an anti-scatter grid in front of the scintillator layer. The imager has several readout modes for use in 2D imaging, fluoroscopy and CBCT applications. The mode used for CBCT applications is called “Dynamic Gain” and has a 16-bit dynamic range. In this mode pixels are grouped together in 2×2 squares which acts as a 1024×768 array of pixel size 0.388 mm. The maximum frame rate in this mode is 30 frames per second (fps).

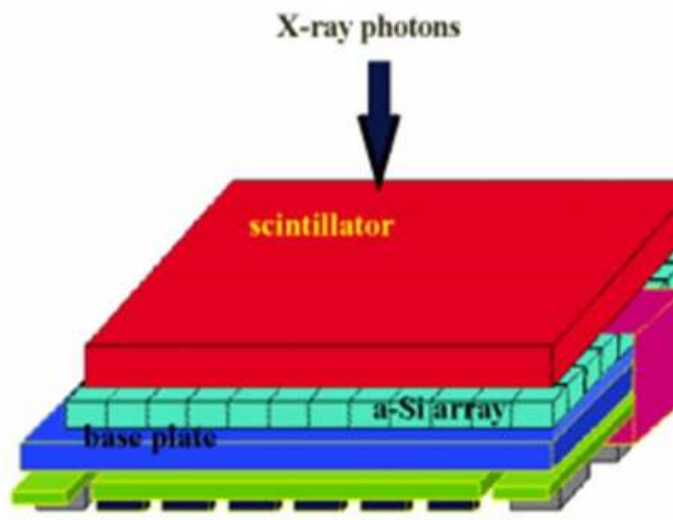


Figure 2.4 Flat-panel detector construction using a-silicon TFTs array (courtesy and Copyright ©2007, Varian Medical systems)

The imaging performance of FPIs is quantified and the geometric nonidealities in gantry rotation are measured and corrected during reconstruction and evaluated using phantoms (Jaffray & Siewerdsen 2000; Jaffray et al. 2002). These systems produce images with improved soft tissue contrast at acceptable imaging doses.

The Elekta imager has a matrix of $1024 \times 1024 \times 16$ bits (of physical size $41 \times 41 \text{ cm}^2$) with nominal frame rate of 5.5 fps. Siemens MVision has a detector of size $41 \times 41 \text{ cm}^2$ imaging a volume of approximately $27 \times 27 \times 27 \text{ cm}^3$.

2.3.2 CBCT Software

In conventional fan-beam geometry, individual axial slices of the object are sequentially reconstructed to give the volumetric data. Filtered Back Projection (FBP) is the most widely used reconstruction technique in CT. In this technique, the projected data

(measured attenuation values) are convolved with filtering kernels and then backprojected to build up the image using Fourier Transforms.

In cone-beam geometry, however, 3D volumetric data can be directly reconstructed from the two-dimensional projection data. This is referred to as cone-beam reconstruction. The Feldkamp, Davis and Kress (FDK) algorithm is the most popular approximate reconstruction technique for cone-beam projections about a fixed isocentre acquired along a circular trajectory (Feldkamp, Davis & Kress 1984). The FDK algorithm is an extension of FBP reconstruction. Figure 2.5 shows the cone-beam trajectory of the source, O' along the circular orbit with centre of rotation, O(x, y, z). In FDK method, the measured 2D cone-beam projections are pre-weighted, filtered and finally back projected along the same ray geometry as initially used for forward projection. During pre-weighting, the angle by which the cone-beam plane is tilted with respect to the central ray is corrected in order to compensate for the increased attenuation of photons along the periphery. The pre-weighted factor is geometrically interpreted as the cosine of the angle ϕ between the cone-beam ray and the central ray of the projection and is calculated using equation 2.1 as,

$$\frac{D}{\sqrt{D^2+s^2+v^2}} \quad \text{----- (2.1)}$$

where D is the distance between the source (O') and the detector plane and (s,v) are the detector coordinates.

FDK method assumes that the data are from a planar detector and the projection data are filtered row by row. If $p(s, v, \beta)$ are the gathered projection data for the projection angle β , then the pre-weighted data convolved with the 1-D ramp-filter, $h(s)$ along the radius of trajectory can be expressed as in equation 2.2,

$$\tilde{p}(s, v, \beta) = \left(\frac{D}{\sqrt{D^2+s^2+v^2}} \cdot p(s, v, \beta) \right) * h(s) \quad \text{----- (2.2)}$$

Finally, the pre-weighted projection data $\tilde{p}(s, v, \beta)$ for each projection angle are back projected and then summed to a reconstruction volume of coordinates (x, y, z) as,

$$f(x, y, z) = \int_0^{2\pi} \frac{D^2}{U(x,y,\beta)^2} \cdot (\tilde{p}(s, v, \beta)) d\beta \quad \text{----- (2.3)}$$

where the factor $U(x,y,\beta)$ is the distance between the source and the reconstructed voxel (x,y,z) projected onto the central ray. It is independent of the z -coordinate of the voxel and depends only on the distance (D) between the source and the detector plane.

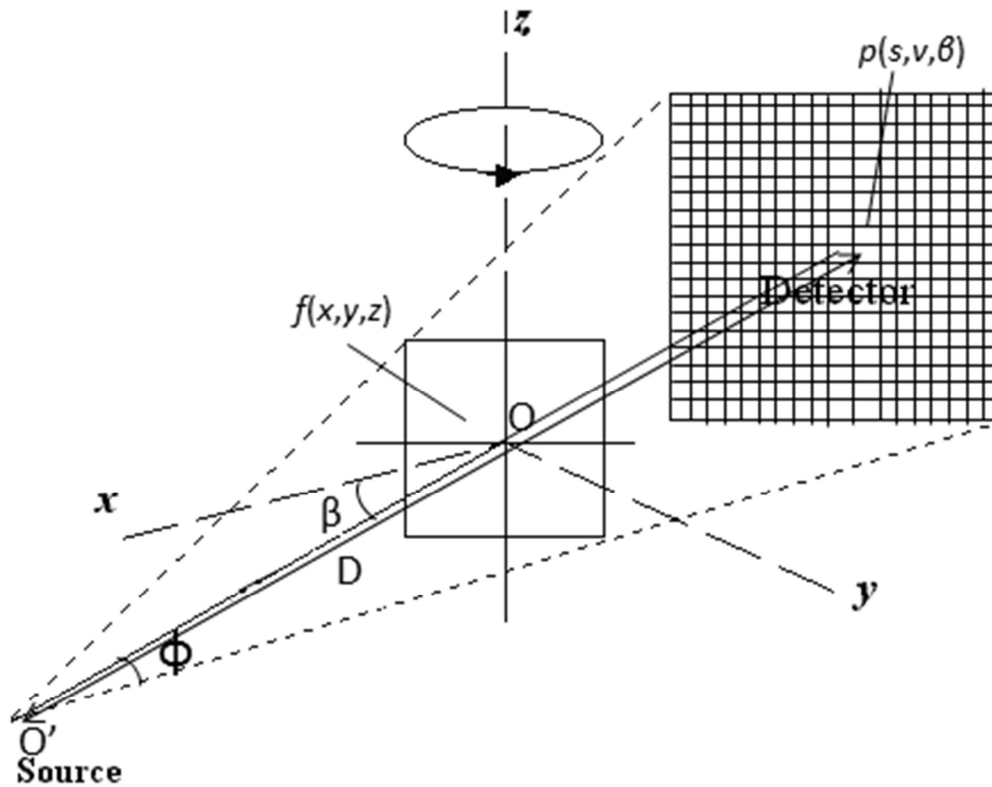


Figure 2.5 Geometric coordinates of CBCT scan with flat-panel detector

These reconstructed images are saved as DICOM¹ files and are available for analysis. Though this algorithm is easy to implement, the projection data acquired along circular orbits are insufficient for accurate reconstruction (Yu, Pan & Pelizzari 2004). This is due to violation of Tuy's condition requiring that every plane intersecting the object under study must intersect the focal trajectory. Also the implementation of the Radon transform for discrete instead of continuous data sampling and the approximations of line integrals make the algorithm inaccurate for planes away from the midplane. As a consequence, cone-beam image quality degrades with increasing cone angles (Feldkamp, Davis & Kress 1984) and images are more prone to artefacts (Soimu, Buliev & Pallikarakis 2008). This led to the

¹ DICOM (Digital Imaging and Communications in Medicine) is a standard for handling, storing, printing, and transmitting information in medical imaging. It includes a format definition and a network communications protocol.

investigation of cone-beam iterative reconstruction algorithms employing several methods such as penalised weighted least squares principles (Wang, Li & Xing 2009), optimising parameters (Qiu et al. 2010) and GPU-based algorithm using tight frame regularization (Jia et al. 2011). These algorithms enable a clinically acceptable image quality to be produced from reduced and noisy CBCT datasets. However, these iterative methods have high computational loads and hence are not practical for clinical situations unless a significant speed-up of the method can be achieved. Thus at present FDK reconstruction remains the most widely used algorithm to provide a quick volume image due to its fast computation time and smaller artefacts for small cone angles. Figure 2.6 uses a block diagram to show the procedures involved in a CBCT acquisition.

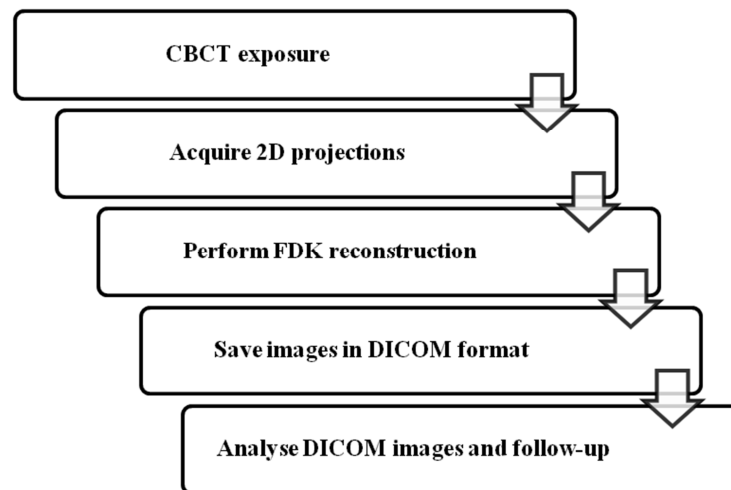


Figure 2.6 Procedures in a CBCT system

2.4 CBCT Applications in Radiotherapy

The primary application of CBCT on linacs is for image guidance purposes (IGRT). However it can additionally be employed for ART tasks as it provides CT numbers, also known as Hounsfield Unit (HU) values that can be calibrated to physical density for use in treatment planning.

Hounsfield Unit is an arbitrary unit of x-ray attenuation used for CT scans. CT images are normalised to these HU values relating the linear attenuation coefficient (μ) of a material i.e. tissue (μ_{tissue}) with the attenuation coefficient of water (μ_{water}). The HU value in each pixel is converted using the following expression (Bushberg et al. 2002):

$$HU = \left(\frac{\mu_{tissue} - \mu_{water}}{\mu_{water}} \right) 1000 \text{ ----- (2.4)}$$

The value of μ_{water} is about 0.195 for the x-ray beam energies typically used in CT scanning. This normalisation results in HU values ranging from -1000 to +3000, where -1000 corresponds to air, soft tissues ranges from -300 to -100, water is 0 (reference) and dense bone and areas filled with contrast agent range up to +3000. CBCT images are produced by high energy x-ray beam, with an average energy of about 100 kVp. At this energy 95% of x-ray interactions are Compton scatter. Therefore the HU values and hence the cone-beam image derives its contrast from the physical properties of tissue that influence Compton scatter.

2.4.1 CBCT for Image-guided Radiotherapy

Highly conformal treatment techniques such as Intensity Modulated Radiotherapy (IMRT) and 3D-Conformal Radiation Therapy (3DCRT) require an advanced imaging modality for localisation of target and organs at risk (OAR). Cone-beam CT enables radiation therapists to correct for changes of the target position prior to treatment and allows monitoring of complex changes of the patient and tumour anatomy, typically caused by patient weight loss and tumour regression. Developments in large area flat-panel detectors and computing capacity have made CBCT the most common platform for high precision 3D IGRT tasks (Jaffray et al. 2002). Thus CBCT as an IGRT tool is popular in verifying patient set-up and tumour position (McCarthy et al. 2006). The use of CBCT-based IGRT has improved the accuracy of radiotherapy treatment at various treatment sites such as prostate, lung and head & neck (Boda-Heggemann et al. 2011; Guckenberger et al. 2007; Létourneau et al. 2005) and in cranial treatment of immobilised patients (Guckenberger et al. 2007).

Cone-beam CT-based IGRT in prostate phantom studies has shown high accuracy with residual errors less than 1 mm. However, in clinical situations, the inter-observer variability was greater than 2 mm for cases without implanted markers. The strategy of daily replanning reduces these uncertainties. The advantage of CBCT-based IGRT over 2D techniques is that it helps in evaluating OAR geometry, for example, bladder filling enables reduction of the dose delivered to OARs and allows significant reduction in the Planning Target Volume (PTV) margin from 8 mm to 4 mm (Pawlowski et al. 2010).

The practice of CBCT-based IGRT for lung cancer is challenging because respiratory motion causes significant motion artefacts. Cone-beam CT can be used to verify tumour motion as a function of respiratory motion when imaging lung and abdominal tumours. However, the tumour motion has to be managed based on the individual breathing pattern. Several approaches to CBCT-based imaging for lung cancer have been practiced. These include a breath-hold technique (Blessing et al. 2010; Wertz et al. 2010), slow scanning (Lagerwaard et al. 2001) and respiration-correlated imaging (Dietrich L & Oelfke 2006; Sonke et al. 2005). In the case of modern CT scanners the gantry rotation is fast compared to the breathing cycle (0.5 second or less). Thus a 3D CT scan can sample different respiratory phases and 4D CT data can be obtained by selecting the slices corresponding to a particular breathing phase. However, in the case of CBCT, the slow gantry rotation (~1 min/rotation) causes blurring of the moving object within all slices. Nevertheless, respiratory-correlated CBCT provides information on tumour motion. This procedure yields 2D projections of CBCT that correspond to a certain respiratory phase by means of retrospective sorting. These projections are then reconstructed into a 4D CBCT dataset (Sonke et al. 2005). Thus 4D CBCT provides information on the 3D trajectory of the moving structures. In addition, it enables safe delivery of gated radiotherapy with small treatment margins. Methods have been developed to investigate the influence of organ motion on 4D CBCT images based on phase binning of CBCT projection data (Li et al. 2006; Lu et al. 2007). Li et al. (2006) concluded that 4D CBCT images can be obtained without increasing the dose to the patient as compared to the current 3D CBCT scan. The inter- and intra-fractional tumour motion in lung cancer as a function of respiration was investigated by Bissonnette et al. (2009) and Gottlieb et al. (2010) to evaluate the tumour motion amplitude over a course of SBRT. Grills et al. (2012) reported a high two-year local control rate of 94% and low toxicity for more than 500 stage I-IIb non-small cell lung cancer (NSCLC) patients for CBCT-based SBRT.

For head & neck cases, conventional methods such as block or mask-based approaches reduce the set-up accuracy. Cone-beam CT-based IGRT technique helps to reduce the set-up time substantially (Boda-Heggemann et al. 2011) and enable a 50% reduction in Clinical Target Volume (CTV) to PTV margins (Den et al. 2010) which could facilitate dose escalation and/or improved toxicity reduction. Since large set-up errors were measured in anatomical sub regions (Li et al. 2008; Polat et al. 2007; van Kranen et al. 2009), image registration should be considered to give high set-up accuracy. Thus the

rationale for CBCT as IGRT is to help in reducing set-up errors by verifying the patient position.

2.4.2 CBCT for Adaptive Radiotherapy

The precision of dose delivery over a treatment course using a single reference PCT can be limited due to changes in the patient's anatomy through weight loss or gain and the tumour shrinkage and displacement. Hence, information about the patient and tumour anatomy immediately before each treatment fraction is of extreme importance for improving the therapy outcome. Adaptive Radiotherapy is a technique in which the treatment prescription parameters such as field margins and number of fractions are modified based on any changes in tumour anatomy and/or patient anatomy. Cone-beam CT has the potential to become a useful tool for online ART (Ding et al. 2007) as it helps to localise the position of the tumour in 3D and to register any changes in tumour and patient anatomy during the treatment. This is done by fusing CBCT images with PCT images using image registration algorithms (rigid or deformable registration) and evaluating the differences. If required, the dose distribution is recalculated using the Treatment Planning Software (TPS) or the software provided with the imaging system. Thus, optimal treatment plans can be obtained using CBCT scans adaptively.

Several studies have used CBCT datasets for adaptive plans to reduce the planning and target margins during the course of treatment. The first clinical results of CBCT as ART evaluated for prostate cancer were found to reduce the PTV margin by 29% on average and the mean dose to the anal wall was reduced by 4.8 Gy (Nijkamp et al. 2008). The study of CBCT as an ART tool for muscle-invasive bladder cancer (Foroudi et al. 2011) was found to reduce the volume of irradiated normal tissue by 29% compared to conventional radiotherapy without reducing the CTV. Hawkins et al. (2010) investigated the considerable reduction in OAR doses during treatment of oesophageal cancer by using PTVs generated from composite CBCT volumes. The dose to lungs was reduced from 15.6 Gy to 10.2 Gy and mean dose to heart was reduced from 26.9 Gy to 20.7 Gy for the adaptive plan. A novel re-optimization technique was demonstrated for prostate IMRT plans and it was found that a CBCT plan solution can be achieved within 2 minutes (Wu et al. 2008). Thus the rationale for using CBCT as ART is to account for the daily changes in tumour anatomy during dose delivery in order to reduce the volume of normal tissue being irradiated and to reduce dose to organs at risk.

Richter et al. (2008) reported that the cone-beam geometry (large volume of x-ray exposure) and associated scatter radiation can cause large variations in the HU values of CBCT. This fluctuation in HU values affects the dose calculation accuracy since the HU values are related to electron density distributions which are used in dose calculation algorithms. Table 2.2 summarises the studies that have investigated the dosimetric accuracy of three linac-mounted CBCT devices for ART using different calibration phantoms and methods. The results were compared with conventional PCT as a reference. Although studies that investigated CBCT for treatment planning showed good agreement with PCT of within 1-3% for phantoms and within 2% for prostate patients using deformable image registration, the level of accuracy breaks down with changes in patient/phantom size (Hatton, McCurdy & Greer 2009). Thus the results cannot be assumed to be the same for all volumes of scanned object.

2.5 Concerns in CBCT

The increased use of CBCT in imaging has led researchers to explore patient imaging dose. Cone-beam geometry covers a large field of view in one rotation and this contributes a larger scattered radiation component when compared to fan-beam CT. The total amount of detected scattered radiation in CBCT exceeds the primary radiation leading to low HU values in the middle of the reconstructed images. This leads to artefacts which impact on image quality metrics such as homogeneity, contrast and noise in the reconstructed CBCT image. Care should be taken when acquiring CBCT images to keep image artefacts to a minimum by selection of optimum scanning parameters and careful patient positioning and stabilisation. Daily images from CBCT add significant dose to the patient, ranging from 3 to 28 cGy depending upon the scan protocol and the region of study (refer Table 2.3). Thus having accurate knowledge of CBCT dosimetry is essential because the accumulated dose from the use of this modality may be significantly higher than that from PCT. The three major concerns in CBCT, artefacts, image quality and patient dose are discussed in the following sections.

2.5.1 Artefacts: Causes and Solutions

The most commonly observed artefacts in CBCT - ring, scatter and noise, beam hardening, aliasing and crescent artefacts are discussed here.

Ring artefacts

The ring artefact is a mechanical artefact that occurs due to miscalibrated detector elements or manufacturing defects. Since CBCT uses a 2D FPI, manufacturing defects in the semiconductor array can result in corrupted cone-beam projections which will affect the reconstructed image with ring-like artefacts. They appear as a number of dark concentric rings centred on the axis of rotation. In order to cover large CBCT volumes, the detector is shifted laterally to the centre of rotation (COR) such that it acquires images in half-fan mode.

This shift in the detector causes a transition between central and peripheral regions of the reconstructed volume in the FOV and may result in a ring shaped artefact in the axial plane (Schulze et al. 2011). Figure 2.7a shows concentric rings in a uniform water phantom as indicated by the red arrow. These rings impair the diagnostic quality of the image by creating a dark smudge at the centre of the image. Although the cause for these ring artefacts have been determined and methods to suppress them were developed (Anas et al. 2011; Ashrafuzzaman, Lee & Hasan 2011; Tang et al. 2001), enhanced reconstruction methods will be required in future to reduce these artefacts further.

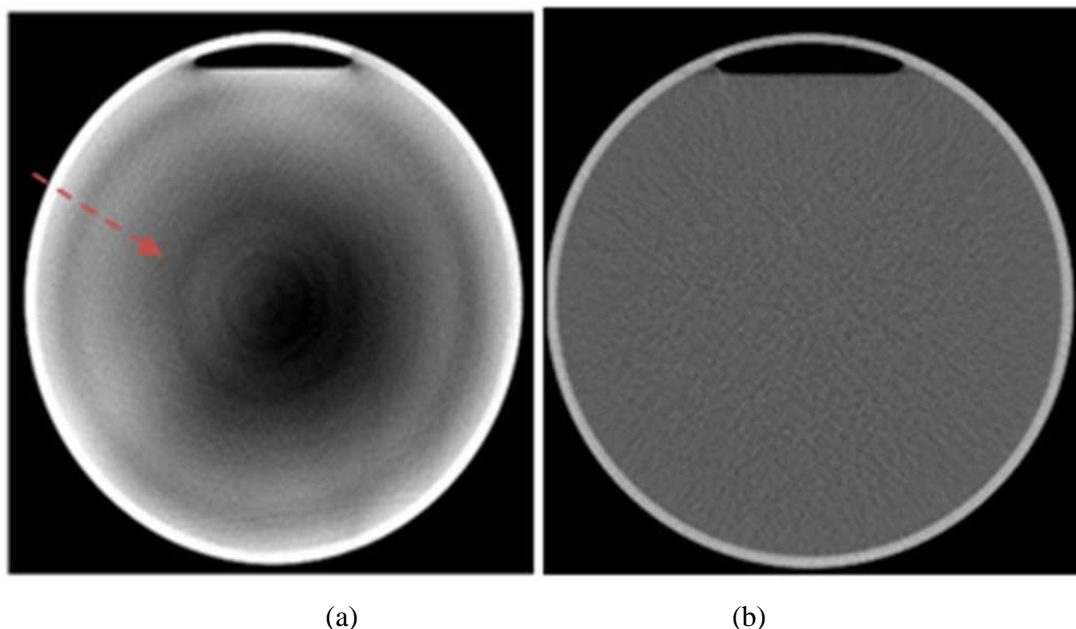


Figure 2.7 (a) Concentric rings (arrows) around the axis of rotation in the CBCT image, (b) fan-beam CT image without ring artefact

Table 2.2 List of studies on dosimetric investigation of CBCT

CBCT devices	Author/ Year	Phantoms/ Patients	Regions	Phantoms used for HU Calibration	Methods	% dose difference between CBCT and PCT plans
Varian OBI	Yoo & Yin (2006)	4 patients	brain and lung	Catphan	direct use of CBCT datasets	brain-1%; lung- large
	Yang et al. (2007)	4 patients	lung and prostate	Catphan	B-spline deformable image registration	lung- large; prostate-<1.5%
	Hatton et al. (2009)	Phantom study	N/A	Catphan 600, CIRS model 62, Gammex RMI 467	direct use of CBCT datasets	Using Catphan calibration 1-5%; CIRS - poor
	Padmanaban et al. (2010)	Phantom study	head& neck; thorax	Catphan	direct use of CBCT datasets	head & neck-<1%; thorax- <3%
Elekta XVI	Houser et al. (2006)	Phantom study	N/A	Gammex RMI 467	with and without heterogeneity correction	without correction- 1%; with correction for non-bolused plans- 14%
	Van Zijtveld et al. (2007)	5 patients	head & neck	--	HU mapping by non-rigid registration	head & neck-1%
	Richter et al. (2008)	33 patients	head, thorax and pelvis	Catphan	Generated HU-density tables for four correction strategies	head- $1.5 \pm 2.5\%$; thorax- $1.8 \pm 1.6\%$; pelvis- $0.9 \pm 0.9\%$;
Siemens MVision	Morin et al. (2007)	2 patients	head and neck	CIRS model 62	Cupping artefact correction applied	better than 3% and 3 mm criteria
	Petit et al. (2008)	Phantom study	N/A	Water cylinders, IMRT phantoms, Rando head phantom	Cupping artefact correction applied	Using water phantom calibration -1%; IMRT phantoms – 2%
	Petit et al. (2010)	Phantoms + 5 patients	thorax (lung) and abdomen (rectum)	Cylindrical water phantom with missing anatomy from PCT	Cupping and truncation correction method applied	Phantoms - within 1%; Patients - 3-4%

-- data not provided; N/A- Not Applicable; PCT- Planning CT; RMI- Radiation Measurements Inc.

Figure 2.7b shows the corresponding reconstructed slice of a water phantom acquired from a 16-slice fan-beam CT scanner (Philips Medical Systems, Cleveland, Ohio, USA) under similar scanning conditions for comparison purposes. Since the acquisition and formatting of projection data for PCT is different from that of CBCT, the reconstructed PCT image is free of ring artefacts and shows enhanced image quality and hence HU uniformity.

Scatter and Noise

The CBCT images include a larger amount of scatter than fan-beam CT and this has been identified as one of the major limiting factors for current image quality in flat panel-based CBCT (Sharpe et al. 2006; Siewerdsen, J & Jaffray 2001). The larger contribution of scatter in CBCT is due to the large FOV of cone-beam geometry (Yang, Schreiber & Li 2007). These scattered photons increase the amplitude of the inhomogeneities towards the centre of the object causing the well-known 'cupping' artefact. Also this low-energy scattered radiation decreases the measured attenuation coefficient values in each detector pixel such that there is a deviation in HU values in each reconstructed voxel. Thus scatter represents the most severe cause of HU variation for flat detector based CBCT. In addition, scatter contributes to noise resulting in degradation of contrast in CBCT images. Several scatter correction algorithms have been proposed to control these artefacts. They can be grouped into three categories, namely, scatter reduction techniques, measurement-based scatter correction and software-based scatter correction (Ning, Tang & Conover 2004; Siewerdsen et al. 2006; Siewerdsen et al. 2004; Zhu et al. 2009). The use of anti-scatter grids and bow-tie filters (Graham et al. 2007; Mail et al. 2008) are the cone-beam scatter reduction techniques that are adopted by CBCT manufacturers. The techniques used for measurement-based scatter compensation are intended to correct for the scatter effects either before viewing the projections or by post processing the acquired projections. Software-based scatter correction adopts convolution filtering with the assumption that the distribution of scatter signal in an image is equivalent to a blurred version of the distribution of primary signals.

Noise is an unwanted signal distributed either randomly or non-randomly in an image. Generally, there are two major types of noise in x-ray projections: Gaussian (electrical noise) and Poisson noise (quantum noise). The Poisson noise (fluctuation of photons exiting the object) in CBCT is high because CBCT machines are operated at low tube

current values for the purpose of dose reduction. Thus the signal-to-noise ratio (SNR) is much lower in CBCT than in fan-beam CT. When images with such low SNR are reconstructed it leads to inconsistent linear attenuation coefficient values and hence HU numbers. Thus the low contrast resolution is reduced due to the high noise level (Steinke & Bezak 2008) leading to loss of diagnostic information. Zhu et al. (2009) proposed a penalised weighted least-squares algorithm to suppress the noise in the CBCT projections after scatter correction. The algorithm is shown to improve the CNR on the Catphan phantom by a factor of 3.6 and reduce the reconstruction error in the scatter corrected image from 10.6% to 1.7%. However, one concern about the noise suppression algorithm is a possible resolution loss due to smoothing and hence a practical solution to suppress noise is not yet developed.

Beam hardening

The x-ray beam is said to be hardened as the low energy components of the polyenergetic spectrum suffer from substantial attenuation in the centre of the object. This results in a decrease in the attenuation values, showing a cupping artefact, a dark area at the centre of the scanned object as seen in the image of the homogeneous phantom in Figure 2.8a. Overcorrections for beam hardening results in a slight increase in HU values at the centre of the object causing the ‘capping’ artefact. The second type of artefact relating to beam hardening is the dark streaks which are seen around high density objects within the FOV. The larger FOV of cone-beam geometry results in recording of high intensity near inhomogeneous materials in reconstructed images leading to streak artefacts (as shown in Figure 2.8b, density phantom). Streak artefacts are very similar to those caused by scatter radiation. Beam hardening effects are minimized by calibrating CBCT scanners for different tube voltages and by using correction algorithms (Hsieh et al. 2000; Wei et al. 2011).

The correction factor obtained reduces bands between bone structures and reduces cupping artefacts in the reconstructed images. Figure 2.8c shows the corresponding reconstructed slice of a CIRS density phantom acquired from a fan-beam 16-slice CT scanner (Philips Medical Systems, Cleveland, Ohio, USA) under similar scanning conditions for comparison purposes. There are no streaks seen around high density materials on the fan-beam image indicating the absence of beam hardening effects.

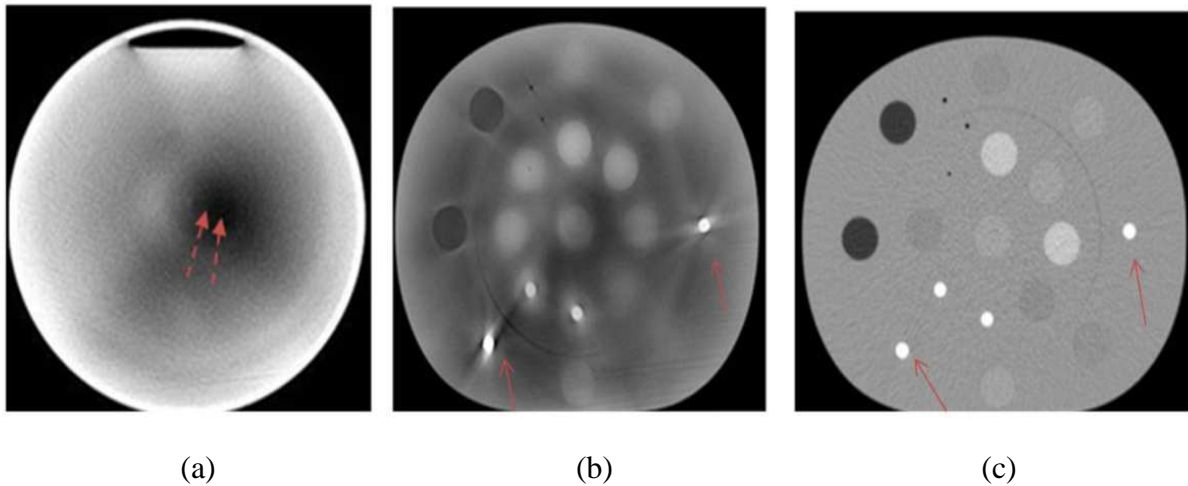


Figure 2.8 (a) a dark smudge (arrows) at the centre of the homogeneous phantom due to cupping artefact, (b) CBCT image of density phantom showing dark streaks (see arrows) around high density inserts and (c) fan-beam CT image of density phantom without streaks

Motion and misalignment artefacts

In addition to the above-mentioned routine artefacts in CBCT, motion and/or misalignment artefacts are also a problem in CBCT (Schulze et al. 2011). The linac gantry has limited rotational speed that makes CBCT images more prone to motion artefacts due to the extended acquisition time. In patient scans, the motion of the structures during scanning leads to streaks from high contrast objects like bones and air cavities (Yoo, Sua et al. 2007). The blurring (Sonke et al. 2005) or streaking effects (Baker 2006) due to moving structures are shown in Figures 2.9a and 2.9b respectively. The large physical displacements cause double contours (Figure 2.9c) on the images ('ghost' images). Patient motion artefacts can be reduced by using positioning aids, and by choosing appropriate protocols to prevent blurring due to respiratory motion. A misalignment in the source-to-detector position relative to the stationary object causes inconsistencies during the back projection process leading to blurring of images. This kind of misalignment errors can be minimised by appropriate quality assurance of the mechanical stability of the systems.

Aliasing artefacts

In cone-beam geometry, the number of rays reaching each voxel decreases with the distance of the slice from the source. As a result, voxels that are nearest to the source

collect more rays than those closest to the detector. This undersampling of the data (large interval between projections) by the divergence of the cone-beam (Schulze et al. 2011) leads to misregistration of information. This results in line patterns in CBCT datasets, called aliasing artefacts, where lines seem to diverge from the centre towards the periphery (Figure 2.10a).

Aliasing may also be introduced by crude interpolation during backprojection in approximating the length of the ray that traverses the voxel. This artefact is greatly reduced by using more sophisticated projection and backprojection techniques (Mueller, Yagel & Wheller 1999a, 1999b) and could be further reduced by having a larger number of projections per rotation and by using a better interpolation method that matches more closely with the physical measurement conditions.

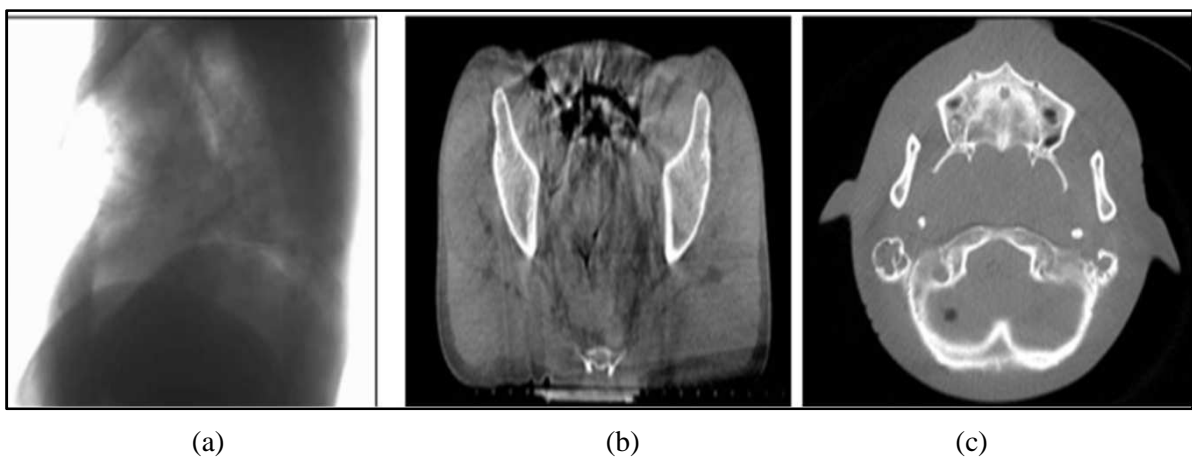


Figure 2.9 (a) Blurring induced by breathing motion, (b) streaks induced from the movement of bowel gas and (c) double contours induced by patient movement during cone-beam acquisition process

However, the need of massive computational power prevents these methods from being used in commercial scanners. Figure 2.10b shows the corresponding reconstructed slice of phantom acquired from a fan-beam 16-slice CT scanner (Philips Medical Systems, Cleveland, Ohio, USA) without aliasing artefacts.

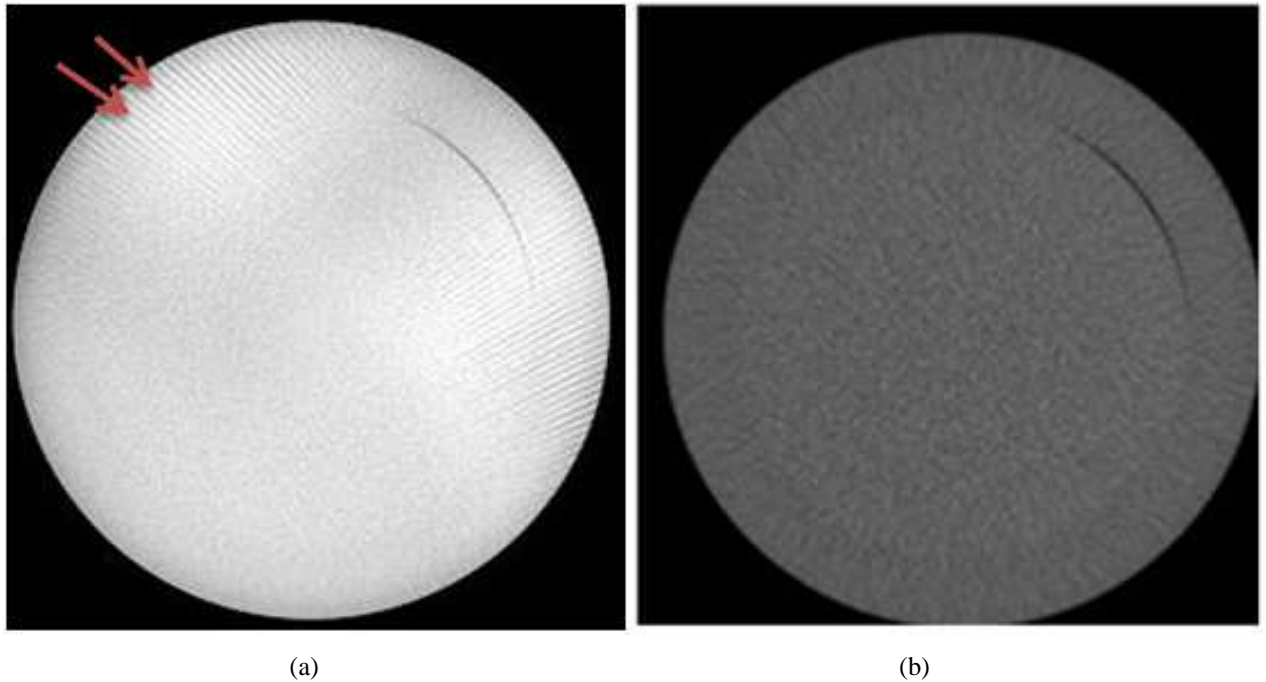
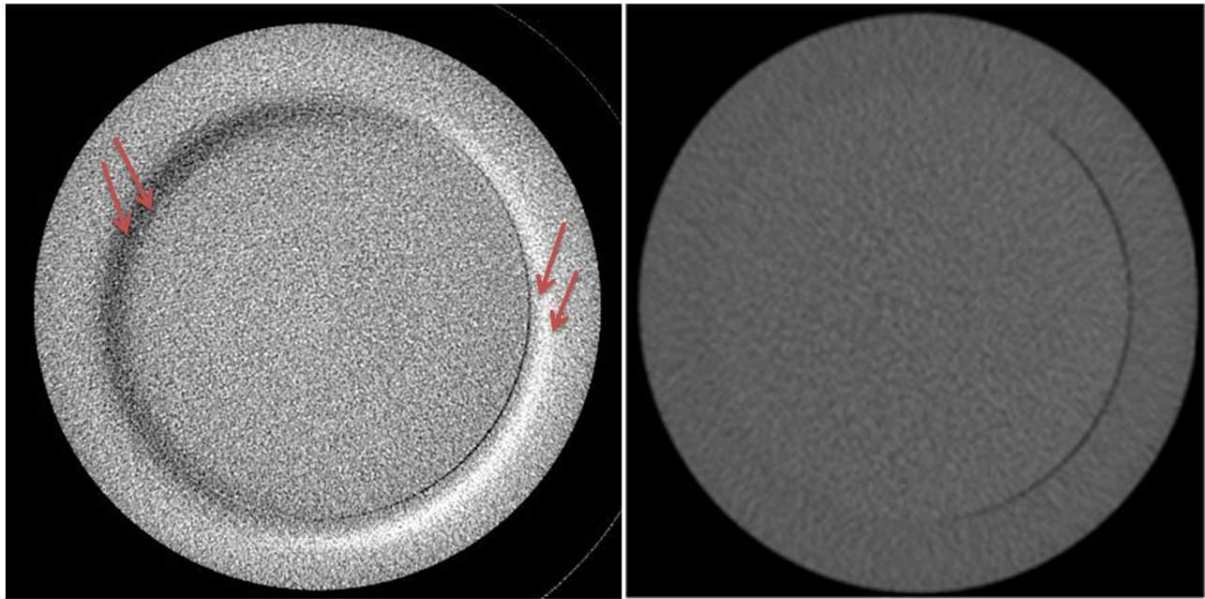


Figure 2.10 (a) Typical aliasing patterns (arrows) in CBCT datasets; (b) without aliasing in fan-beam CT image

Crescent artefacts

CBCT images from the Varian OBI exhibit a crescent-shaped artefact (Figure 2.11a), which is very prominent in homogeneous objects scanned using the full-fan mode of acquisition. The artefact consists of dark and bright crescents located on opposite sides of a circle around the isocentre. These crescents cause a CT number variation of up to ± 100 HU which would lead to erroneous dose values when used for treatment planning. As stated in the Varian OBI reference guide, these artefacts are most likely to occur due to minor mechanical instabilities, such as a small tilt of the x-ray tube assembly or a shift of the focal spot. Figure 2.11b shows the corresponding reconstructed slice of phantom acquired from a fan-beam CT scanner (Philips Medical Systems, Cleveland, Ohio, USA) without crescent artefacts.

In general, many technical developments are in progress to reduce these cone-beam artefacts. As most of the errors occur during reconstruction, an effective approach to avoid these artefacts is to use sophisticated algorithms that account for large FOV volumes.



(a)

(b)

Figure 2.11 (a) Opposing dark and bright crescents seen on CBCT datasets of Catphan and (b) fan-beam image of Catphan without crescent artefacts

2.5.2 Image Quality

Cone-beam CT is used to assess patient positioning at the time of treatment through image registration. Thus the image quality parameters of these devices such as high-contrast resolution, low-contrast resolution, contrast-to-noise ratio and image uniformity are of great importance. Current CBCT systems have limitations due to image resolution and sensitivity of the detector. Projection geometry (Scarfe & Farman 2007) is also an issue because the lower number of cone-beam projections from circular orbits is insufficient for accurate reconstruction of the volume. Also, due to computational limitations, all CBCT machines currently available make use of a FDK reconstruction algorithm which simply approximates the line integral without computing the original distance that the ray traverses between the source and the detector.

Although the kV-CBCT technique is clinically well established, intensified scatter artefacts lower the image quality and hence the diagnostic information. Image quality studies for different CBCT acquisition modes have been performed to find parameters that affect the image quality (Elstrøm et al. 2011; Kamath et al. 2011). A comprehensive study of the relation between dose and image quality in low dose CBCT (Yan et al. 2012) showed that

image quality degradation becomes evident when the imaging dose is decreased below 100 mAs and becomes dramatic when the dose is less than 40mAs. Thus the method to reduce radiation dose may involve trade-offs in CBCT image quality and thereby image quality acts as a potential limiting factor in terms of patient dose.

2.5.3 Dose Accumulation

The daily use of CBCT as an online image guidance tool would cause the additional dose to the patients to be substantial. To date the dose from CBCT for imaging is not taken into account in the treatment planning process. Table 2.3 summarises studies that reported on Varian CBCT and Elekta CBCT dose measured using several phantoms and validated by simulation techniques. These studies were investigating CBCT dose to several organs utilizing default head and body protocols of Varian and Elekta; they reported that the use of CBCT for daily imaging would result in considerable dose leading to an increased risk of secondary cancers.

To prevent deleterious effects of these additional doses on patients it is essential to quantify the dose from CBCT imaging for patients undergoing therapy by physical measurements. Further the dose received by patients must be evaluated by simulating the CBCT spectrum and a virtual human phantom using Monte Carlo techniques. Kan et al. (2008) compared the effective patient doses for Varian CBCT and fan-beam CT, and found that in standard mode (125 kVp, 80 mA, 25 ms, 150cm SDD) there is a significant difference in effective dose to the patient. The results were also higher than those for the Elekta XVI system showing that there is considerable variation among CBCT devices. Hyer et al. (2010) studied organ and effective dose of both Varian OBI and Elekta XVI systems with factory installed protocols for head, chest and pelvis using an in-house adult male anthropomorphic phantom. With an in-house fibre-optic coupled dosimetry system, the doses to several organs and tissues were measured and basic image quality metrics were also evaluated. They reported that Varian exhibited superior image quality (8 line pair/cm resolution for head scan and 4 mm low contrast detectability for chest and pelvis scans) but yielded higher doses for head scans (effective dose is 0.12 mSv) and pelvis scans (effective dose is 4.34 mSv) compared to Elekta XVI (effective dose for head scan is 0.04 mSv and pelvis scan is 3.73 mSv). It is well known that CBCT imaging dose results in significantly more dose to patients (Table 2.3) than fan-beam CT.

Table 2.3 CBCT dose studies based on Varian OBI and Elekta XVI

Studies	Author / Year	Phantoms	# Patients	Dose measurements	Dose calculations	Dose measured (cGy)	Conclusion
VARIAN OBI	Ning et al. (2007)	Rando phantom	7 prostate cases	TLDs	--	<u>Phantoms</u> : 10 - 11 cGy (left hip); 6 - 7 cGy (right hip) <u>Patients</u> : 3- 6 cGy (AP); 4 cGy (left lateral); 2.6 cGy(right lateral)	Left lateral dose is 40% higher than right lateral dose
	Song et al. (2008)	Uniform acrylic phantoms (18cm and 30 cm diameter)	--	0.6 cc farmer ion chamber	Weighted-CTDI equations	8.5 ± 0.12 (HS) ; 4.1 ± 0.09 (BS)	Average dose from 1.1-8.3 cGy is received with highest measured for full-fan mode
	Kan et al. (2008)	Female Anthropomorphic phantom	--	TLDs	--	3.8 - 5.9 (HS) with exclusion of higher doses to thyroid (11.1), skin (6.7) ,lens (6.2); 3.8 - 6.2 (BS)	Increase in secondary cancer risk by 2-4%
	Ding et al. (2008)	RSVP head and pelvis phantoms	3	Thimble ion chamber (0.13 cc)	Monte Carlo simulation	<u>Phantoms</u> : 7.92 (HS) ; 4.33 (BS)	Integral dose is significant
	Kim et al. (2008)	Head (16 cm) Body phantoms (32 cm)	--	TLDs	Weighted-CTDI equations	9.74 ± 0.52 (HS) 2.53 ± 0.06 (BS)	CBCT dose level could increase the secondary cancer risk
	Ding et al. (2009)	--	8 (5- adults ; 3- child –CT images)	--	Monte Carlo (VMCBC algorithm)	<u>Adult</u> : 5 (Br); 18 (CV); 3 (Pr); 7 (F) <u>Child</u> : 6 (Br); 23(CV); 7 (Pr); 17 (F)	Dose from full-fan mode is 10-20% less than half-fan mode
	Palm et al. (2010)	Alderson phantom, CTDI body phantom	--	TLDs ; CT Dose Profiler (CTDP)	--	<u>Alderson (TLD)</u> : 4.65 - 5.12 (HS) ; 3.05 - 3.18 (BS) <u>CTDI body phantom</u> : 2.14 (TLD) ;1.90 (CTDP)	Imaging doses are significantly lower in Varian OBI v1.4 version compared to OBI v1.3
ELEKTA XVI	Islam et al. (2006)	Water phantom	--	0.6 cc farmer ion chamber, MOSFET	--	23 - 29 (H) 18 - 23 (B)	Employ low kVp and small FOV to reduce patient dose
	Amer et al. (2007)	phantom, Standard CTDI phantom	9	TLDs; 0.125cc Ion chambers	ImPACT CT patient dosimetry calculator	3 (H); 15 (L); 35 (P)	Develop low dose CBCT techniques to reduce imaging dose
	Downes et al. (2009)	Plastic phantom	3	NE 2571 farmer IC	Monte Carlo simulation	50 (H) ; 20 - 25 (B)	Dose to bone is 2-3 times higher than tissues

H-Head; B-Body; L-Lungs; P-Pelvis; HS-Head scan; BS-Body scan; Br-Brain; CV-cervical vertebrae; Pr-Prostate; F-Femoral head; --No data; VMCBC-Vanderbilt-Monte-Carlo-Beam-Calibration; RSVP-Radiosurgery Verification Phantoms

With daily CBCT imaging for 30 treatment fractions, organ doses in some cases, such as the testes, exceed 1Gy (Hyer et al. 2010) and would reach their tolerance dose limits before the inclusion of the dose due to the treatment beam. Choosing an appropriate protocol suited for a clinical task is one of the easiest ways to reduce patient dose. For example, in a head & neck study where positioning can be done using bony anatomy, soft tissue contrast is often not required. Thus one can opt for a low dose CBCT mode which is sufficient for positioning (Kan et al. 2008; Sykes et al. 2005). However if the study needs soft tissue contrast, then higher CBCT doses are required. Further reducing x-ray tube current (mA) or pulse width settings (ms) just before an individual patient is scanned would result in reducing the dose below the default settings while reducing image quality to some extent. Thus studies are ongoing to determine the measures to reduce the CBCT dose in order to set up image guidance regimens that are more effective and efficient (Murphy et al. 2007).

2.6 Conclusions

CBCT is, in principle, an effective image guidance and adaptive radiotherapy tool. However, in practice, the presence of artefacts caused by the image acquisition and reconstruction techniques employed have been shown to have a negative effect on CBCT image quality giving rise to reduced uniformity and low contrast resolution. In addition, the CBCT dose to patients may be increased significantly if used on a daily basis and hence an accurate knowledge on CBCT dosimetry is essential. A review on applications of linac-mounted CBCT in modern radiotherapy has been published recently (Srinivasan, Mohammadi & Shepherd 2014).

Chapter 3

Comparison and Evaluation of PCT and CBCT Dose Distribution

3.1 Introduction

Cone-beam CT datasets can be used for treatment planning and dose calculations (Richter et al. 2008) if the HU information provided is reliable and accurate. For accurate dose calculations, knowledge of the relationship between HU and density is essential. Cone-beam CT images include a larger amount of scatter compared to that in fan-beam CT images (Sharpe et al. 2006; Siewerdsen, J & Jaffray 2001), resulting in a larger variation in HU values, which limits the HU calibration accuracy and reliability (Tucking, Nill & Oelfke 2006; Yang, Schreiber & Li 2007). Thus, to date treatment plans based on PCT image sets (fan-beam geometry) are still superior to those based on CBCT image sets (Lo et al. 2005). The magnitude of the scattered radiation in CBCT depends on the size of the scanned object (Siewerdsen, J & Jaffray 2001; Yang, Schreiber & Li 2007; Yoo, S. & Yin 2006) and hence soft tissue contrast becomes dependent on object size. In addition, limited gantry rotation speed and large FOV in a single rotation pose problems for image quality. Many methods have been developed to improve the image quality of CBCT (Depuydt et al. 2006; Morin et al. 2007; van Zijtveld, Dirkx & Heijmen 2007; Wong et al. 2007). It was reported that the number of projections (400-700) from cone-beam geometry is insufficient for image reconstruction, leading to variations in HU values (Richter et al. 2008). Apart from the geometrical limitations, the FDK algorithm used for cone-beam reconstruction has the limitation of approximating the line integrals and hence the image quality degrades as the plane moves away from the central axis (Schulze et al. 2011).

Despite these drawbacks, many studies have investigated the use of Varian's CBCT datasets for dose calculations using Catphan (see Table 2.2) and found that the difference in dose can vary up to 5% between CBCT- and PCT-based treatment plans. Guan & Dong et al. (2009) found dosimetric differences up to 6.7% if Catphan was used for HU calibration. For bone inhomogeneities, the difference in dose goes up to 20% for two different beam energies (Hatton, McCurdy & Greer 2009). Other approaches of using CBCT datasets for dose calculations are to generate specific HU-density tables (Richter et

al. 2008) and mapping of HU values of PCT with that of CBCT values using pixel correction strategies from look-up tables (Depuydt et al. 2006; Tucking, Nill & Oelfke 2006) or using rigid registration algorithms (van Zijtveld, Dirkx & Heijmen 2007). Several scatter correction methods have been developed (Ning, Tang & Conover 2004; Poludniowski et al. 2009; Rinkel et al. 2007; Siewerdsen et al. 2006; Siewerdsen et al. 2004; Zhu et al. 2009; Zhu, L, Wang & Xing 2009) in order to make CBCT-based dosimetry reliable. However, to date CBCT-based planning is not clinically acceptable due to the large variations in HU values with scanned object dimensions (refer section 2.4.2). Thus the results cannot be assumed to be the same for all volumes of scanned object.

This chapter investigates the use of Varian CBCT-based treatment planning for different phantom dimensions by studying the relationship between HU values, scanned object dimensions, and dose distributions. The variation in HU values along phantoms of different thicknesses is compared. Parameters that affect the uniformity of the HU values and their impact on dose calculations are investigated. The dosimetric accuracy of kV-CBCT-based dose calculations is evaluated by extending the study to clinical situations.

3.2 Materials

3.2.1 Varian OBI

This study used the Varian OBI (Varian Medical Systems, Palo Alto, CA, USA), which has been attached to linac at 90° with respect to the treatment beam. Three modes of imaging are available in Varian OBI, namely kV radiography, CBCT, and fluoroscopy. The OBI consists of a kV X-ray source (0.4 and 0.8 mm focal spots) and a kV amorphous silicon digital imaging detector, which faces the X-ray source (Figure 3.1). For reconstruction diameters of up to 24 cm, a full-fan mode is used, where the beam central axis passes through the detector centre in order to acquire full projections of the entire object in a single rotation. A total of 360 projections during the 200° gantry rotation are obtained in full-fan acquisition. Imaging in full-fan mode uses standard head protocol with 100 kVp, 20 mA and 20 ms. For larger reconstruction diameters (up to 45 cm), the CBCT acquisition is switched to half-fan mode in which the detector is offset by 14.8 cm to acquire 655 projections during 360° gantry rotation. In this mode, one half of the projections are obtained from one half-fan projections and the other half is obtained from the other half-fan projections from the other direction. Imaging in half-fan mode uses

pelvis protocol with 125 kVp, 80 mA, and 13 ms. A bow-tie filter (refer section 2.3.1) is added to the kV source while scanning. The CBCT version used is 2.1 and the OBI version is 1.5.



Figure 3.1 Varian Clinac iX unit with OBI, Varian Medical system

3.2.2 Philips PCT

A Philips Brilliance Big Bore CT scanner (Philips Medical Systems, Cleveland, OH, USA) version 2.2 was used in this study to acquire reference CT images (Figure 3.2). It is a 16-slice helical scanner that has an 85-cm-diameter bore and modulates the tube current during the scan based on patient anatomy.

In order to take CT images for radiotherapy treatment planning, the patient is positioned on a flat-top couch of a CT scanner in the treatment position. Alignment of the patient is made with lateral wall lasers and a sagittal laser. A pilot (scout view) scan is then taken to determine the region over which axial slices are required. The target volume and isocentre are identified by the radiation oncologist from the scan information while the patient remains in the treatment position. The patient is marked with reference points where the laser projection illuminates the skin and finally the patient is removed from the couch. Table 3.1 shows the scan protocols for CBCT and PCT for the head and body scans used in this study. The slice thickness can be selected based on the study and depends on which collimation aperture and resolution mode are chosen. Several filters, including standard,

high and ultra-high resolution filters, are available for each mode to optimize image quality. Depending on the FOV and resolution mode, the pixel resolution is determined by choosing the size of the matrix, which can be 512×512, 768×768, or 1024×1024.



Figure 3.2 Philips CT scanner, Philips Medical system

Table 3.1 Image acquisition parameters for CBCT and PCT for head and body scans

Parameters	CBCT		PCT	
	Head	Body	Head	Body
Scan mode	Head	Body	Head	Body
Bow-tie filter	Full	Half	--	--
X-ray Voltage (kVp)	100	125	90	120
X-ray Current (mA)	20	80	250	133
Exposure time*	20 ms	13 ms	800 ms	750 ms
Source-to-Imager distance (cm)	150	150	--	--
Number of projections	360	655	--	--
Detector configuration (cm ²)	30×40	30×40	16×1.5	16×1.5
Field of view (cm ²)	25×25	45×45	25×25	35×35

*Exposure time for CBCT is per projection and for PCT is per rotation

3.2.3 Treatment Planning Systems

The data acquired from CBCT and PCT is transferred to the TPS where the dose delivery from each beam is accurately calculated using an algorithm, taking 3D scatter and inhomogeneities into account. The TPS displays the complete 3D dose distribution and also evaluates the plan using dose-volume histograms (DVH).

The TPS used in this study is Pinnacle³ (ADAC Laboratories, Milpitas, CA, USA) version 8.0m. Collapsed cone convolution (CCC) is the model-based algorithm (Ahnesjo 1989) used for dose calculations. It has built-in tissue heterogeneity corrections, handles 3D anatomical information and allows accurate dose calculations in heterogeneous conditions.

3.2.4 Phantoms and Patients

Phantoms of different dimensions were used to evaluate the dose distribution from CBCT. They are shown in Table 3.2.

Table 3.2 Dimensions of phantoms used for this study

Phantoms	Thickness (cm)	Diameter (cm)
Catphan	20	20
CIRS density	5	33
Water	8.8	25
Norm head	27	25
Norm body	28	45

- The Catphan 504 phantom (The Phantom Laboratory, NY, USA) uses tissue substitute materials and is cylindrical in shape measuring 20 cm diameter and 20 cm thickness. It has several modules. The module used for this study (CTP404) contains inserts of different densities.
- The CIRS density phantom model 062 (CIRS Tissue Simulation Technology, Norfolk, VA, USA) uses water and tissue equivalent epoxy materials. It is a homogeneous ellipsoidal phantom (33 cm × 5 cm × 27 cm) with 17 small cylindrical parts that can be separated out. The dense bone insert in this phantom is represented by hydroxyapatite, whose mineral composition is similar to that of animal bones. It has a removable central circular section that enables this phantom to be used for both the head and the abdomen.

- Other homogeneous phantoms studied to evaluate HU uniformity were: a water phantom (8.8 cm thick and 25 cm in diameter), a Varian Norm phantom for head scans (made of polyethylene 27 cm thick and 25 cm in diameter) and a Varian Norm phantom for body scans (made of polyurethane 28 cm thick and 45 cm in diameter).

CBCT scans of two prostate patients which were acquired during the course of their treatment were utilised for evaluating CBCT-based dose calculations. Both patients had similar dimensions, with an anterior-posterior separation of 21 cm and a lateral separation of 34 cm.

3.3 HU Calibration

3.3.1 Method

Initially images of the above-mentioned phantoms were acquired from two volumetric imaging systems: the PCT as a reference and the CBCT. Both systems were operated under similar scanning conditions (tube voltage, tube current, and phantom positioning). Once the images were acquired, they were imported into Pinnacle³ TPS for HU-density calibration.

Dose distributions were calculated based on the density distribution of the irradiated tissue. Since a CT scanner measures HU values, a calibration function must be derived to determine the physical densities of region of interest. In order to obtain a calibration curve for a CT scanner, the CIRS density phantom, which is specifically manufactured to obtain a precise relationship between HU numbers and electron densities, was used. Since the volumetric imaging of CBCT includes large fields of view, the use of the thin CIRS density phantom for CBCT calibration may lead to more scatter contribution compared to PCT. Hence, this study used both the density phantom and the Catphan for CBCT calibration and compared with the PCT calibration to evaluate a suitable CBCT calibration curve for treatment planning.

Central slices from the density phantom and from the CTP 404 module of Catphan were selected in Pinnacle³ and the circular regions of interests were drawn within particular insert to measure the average HU values. Once the HU values were measured, they were plotted against the known density of the tissue inserts for both PCT and CBCT data. Thus,

the HU values in each voxel of the reconstructed image were calibrated to the density values for tissue inhomogeneities.

3.3.2 HU Calibration Results

The relationship between HU values and physical densities of Catphan inserts was established for PCT and CBCT. Routine planning was performed using a PCT calibration curve obtained using the CIRS density phantom (i.e., the reference curve). Figure 3.3 shows the calibration curves obtained for PCT, CBCT using the density phantom (curve 1) and CBCT using the Catphan phantom (curve 2). Error bars are the standard deviations of the HU values within the inserts of the phantom.

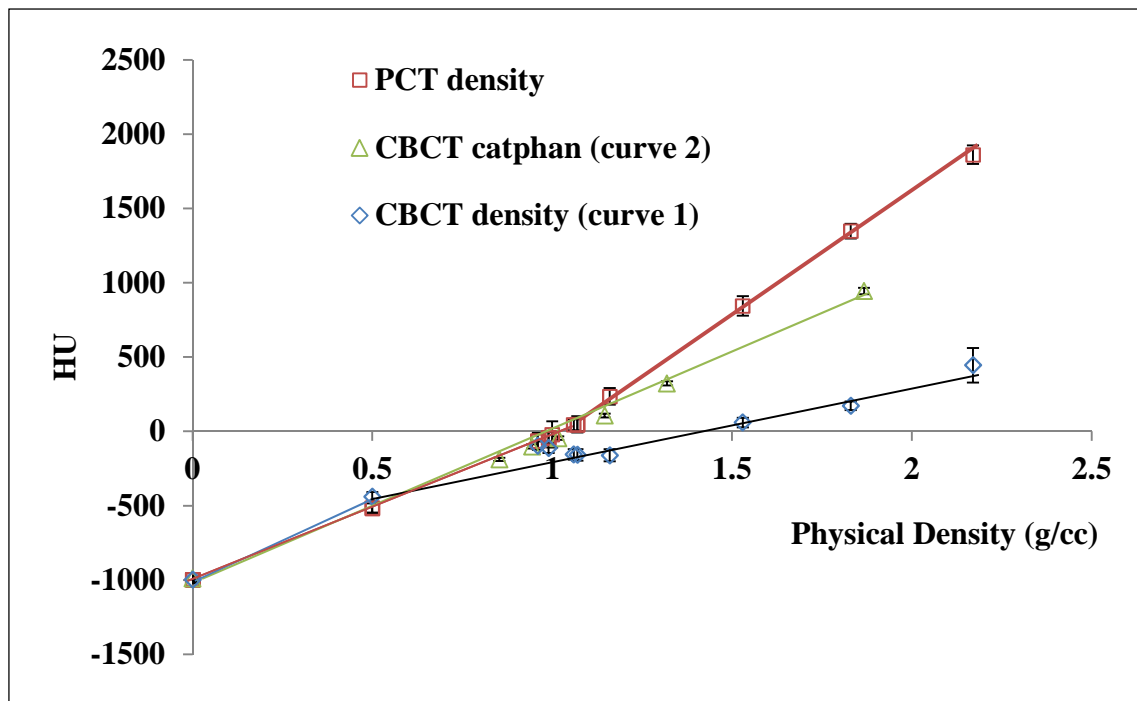


Figure 3.3 Calibration curves for PCT and CBCT

The PCT curve shows a bilinear relation between HU and density. Above the water equivalent density (1g/cc), there is a higher gradient in HU values because in humans, high density regions such as bone have higher effective atomic number than soft tissues. Since the probability of photoelectric effect increases with increase in atomic number the linear attenuation of photons and hence the HU values increase steeply beyond the soft tissue region. The CBCT curve 1 was found to diverge from the corresponding PCT curve, showing reduced values of HU due to a large scatter contribution from CBCT. The density phantom, which is designed for fan-beam CT, is very thin (5 cm thickness) compared to

the large FOV of CBCT. This causes a greater amount of scattered radiation to reach the detector. As a result, the apparent attenuation of photons and hence the HU values are reduced. Comparing the PCT and CBCT calibration curve 1, the HU values agree up to ~0.5 g/cc. The deviation in HU linearity for curve 1 is greater than that for curve 2. Since the HU calibration on the Varian OBI system was performed using the Catphan phantom, the CBCT calibration curve 2 agrees well with the PCT curve for the low-density region up to 1 g/cc (water), after which the values gradually diverge below those of the PCT curve. This reduction in HU values is due to the contribution of scattered radiation around high-density materials. However, the variations in cone-beam HU values of each Catphan inserts are within the nominal HU value tolerance of ± 40 . Thus, the curve 2 is more reliable for treatment planning based on CBCT datasets.

3.4 HU Profiles

3.4.1 Method

The variation in HU values along the Z axis of the scanned object (Figure 3.4) is of more concern when dose delivery is based on 3D dose distributions. The HU profiles along the thickness of four different phantoms, density phantom, water phantom, Catphan and Norm body were extracted using ImageJ software (National Institutes of Health) from CBCT data and the percentage variation in HU values was determined. In the same way, the HU profiles along the diameter of the Catphan, Norm head, Water and Norm body phantoms were extracted to determine the percentage of variation in HU values. The percentage of HU variation as a function of phantom dimensions (thickness and diameter) was then examined.

3.4.2 HU Profile Results

Figure 3.5 shows the cone-beam HU profiles of the water phantom, Norm head phantom, and Norm body phantom. The HU profile of the water phantom (Figure 3.5a) exhibits a large variation in HU values, with higher values at the centre and lower values towards the periphery. This difference in HU values is suggestive of the “capping” artefact caused by overcorrection for beam hardening effects. This artefact reduces the reconstructed image quality, leading to poor low-contrast resolution. With an increase in the thickness of the phantoms (Norm head and body phantoms), the HU fluctuation was significantly reduced (Figure 3.5b and 3.5c), leading to flatter profiles. The results showed that the HU profiles

were dependent on scanned object size. In contrast, the PCT HU profiles of water phantom, Norm head and Norm body phantoms were found to be stable ($\leq 1\%$ HU variation) and were independent of scanned object dimension (figure not shown).

Figure 3.6 shows the percentage of HU variation as a function of phantom dimensions. It was found that when the thickness of the object is less than the scanning length (standard cone-beam scan length = 16 cm), the scatter contribution leads to high HU variation. Similarly, the HU variation is higher for phantoms of lesser diameter. Thus it was found that there is a minimum percentage of HU variation for scanned phantoms whose dimensions are larger compared to the calibration phantom.

When the thickness of the scanned object is less than that of the Catphan calibration phantom (20 cm thickness), there is about 0.8-1% variation in HU values along the z-axis of the phantom. When the diameter of the scanned object is twice as large as that of the calibration phantom, the variation in HU values reduces to 0.1%. This shows that cone-beam HU values depend on phantom geometry and hence appropriate CBCT calibration curves are required for specific anatomical sites. Thus different phantoms with the size of the scanned object (anatomical site) are required in order to provide different calibration curves for different clinical studies.

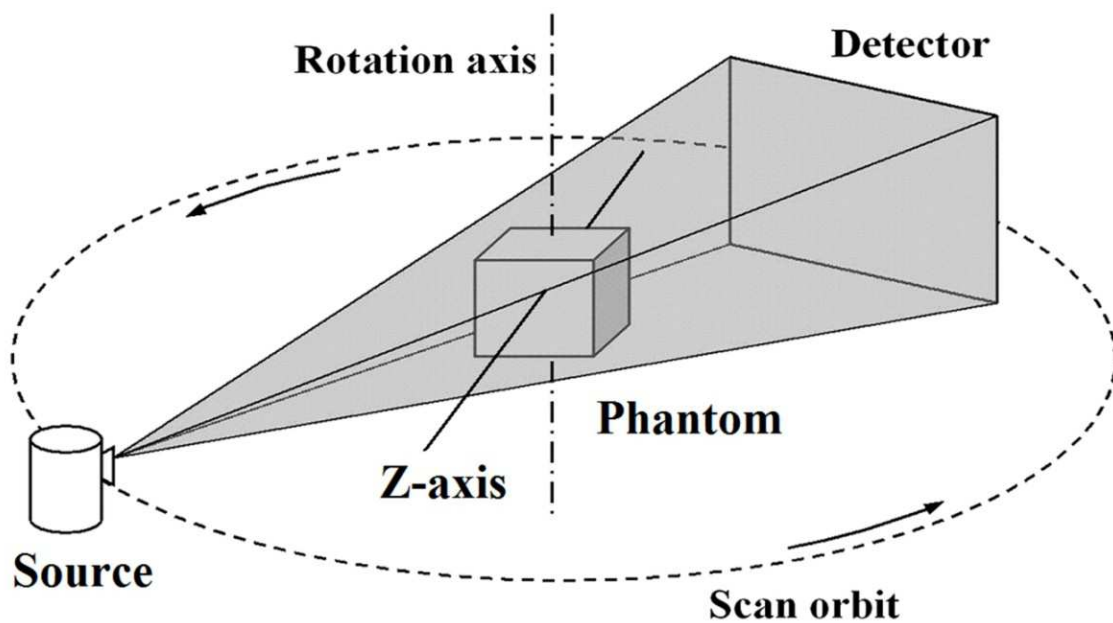


Figure 3.4 CBCT scanning of phantom along Z-axis

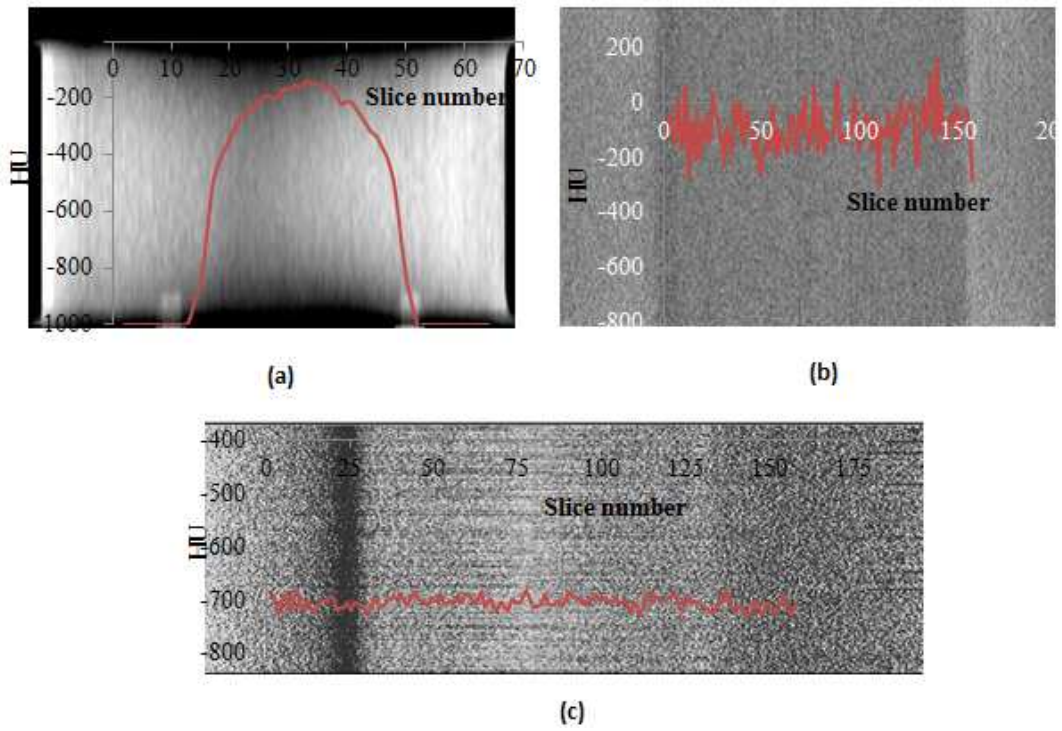


Figure 3.5 Cone-beam HU profiles of (a) Water phantom, (b) Norm head phantom and (c) Norm body phantom along Z-axis (background of each profile is the axial slices of respective phantoms)

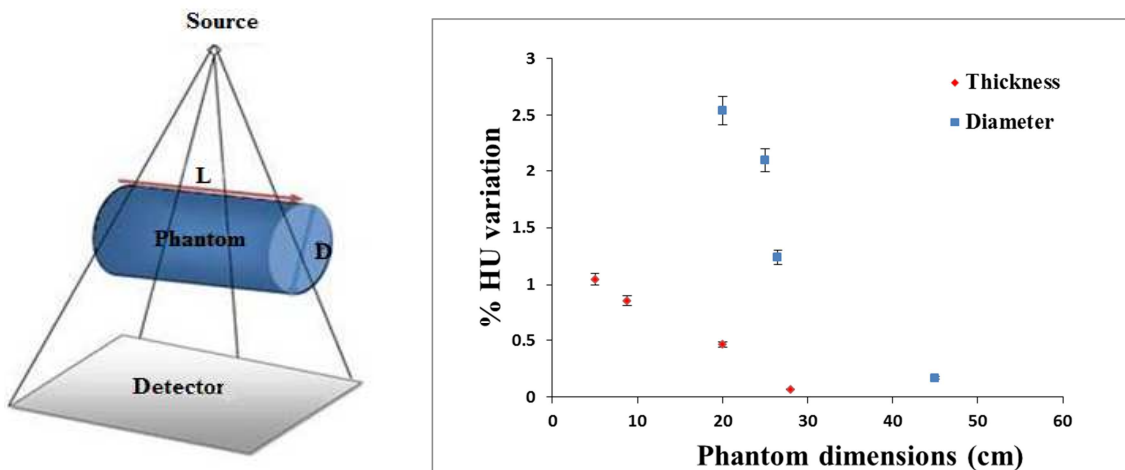


Figure 3.6 Cone-beam HU dependence on phantom dimensions along thickness (L) and diameter (D) of phantom

3.5 Dose Calculations and Evaluations

3.5.1 Method

A PTV of the same size (3 cm diameter) and shape (spherical) was contoured in both PCT and CBCT datasets to ensure similar planning conditions for comparison purposes. The PTV for the Catphan, water, and Norm body phantoms was chosen to be at the centre of the phantoms. For the density phantom, the PTV is the breast equivalent insert material (physical density = 0.99 g/cc) at the periphery of the phantom. To calculate the dose distributions in the region of interest, a single 6-MV photon beam with a field size of $10 \times 10 \text{ cm}^2$ was generated using the source to axis distance (SAD) technique for PCT and CBCT data. The resultant dose distributions and the plot of cumulative DVH that summarizes the radiation distribution within the volume of interest were obtained and compared.

Planar dose distributions of various phantoms obtained from Pinnacle were imported into MapCHECK™ software (SUN NUCLEAR Corporation, Melbourne, FL, USA) in order to compare and analyze the PCT and CBCT dose distributions quantitatively. The gamma analysis method (Low et al. 1998) with a dose difference threshold of 3% and distance-to-agreement (DTA) criterion of 3 mm (3%/3mm) was used to compare the CBCT dose distribution with that obtained using PCT (refer section 6.3.5).

To evaluate the CBCT-based dose calculation, the CBCT scans, selected as described in section 3.2.4, were transferred to Pinnacle³ TPS. The target region included the prostate gland with a margin of 6 mm. Femoral heads were included during planning as organs at risk. Static plans using five 6-MV photon beams of equal weighting with gantry angles of 0° , 55° , 130° , 230° , and 310° were adopted for the two cases. Cone-beam CT images were acquired with the patient in the treatment position. The images were saved to the record and verify (R&V) system and then analyzed. The PCT- and CBCT-based treatment plans were compared under conditions similar to those for the phantoms.

3.5.2 Dose Calculations Results

The PCT and CBCT dose distributions (coloured lines) obtained in the axial slices of the Catphan and Norm body phantom are shown in Figure 3.7. The isodose lines were calculated using a single 6-MV $10 \times 10 \text{ cm}^2$ photon beam. An identical spherical target (red

circle) with a 3-cm diameter and of similar volume was delineated in axial slices of PCT and CBCT images. The dosimetry results were evaluated for each study using DVHs, which are shown in Figure 3.8. The results show that the agreement with the PCT dose distribution obtained is better using CBCT calibration curve 2 than using CBCT calibration curve 1. However, for Norm body phantom, the shift in the 50% isodose line (figure 3.7b2) produces an observable variation in distribution of dose within the defined volume (figure 3.8d). This indicates that CBCT dose distributions are dependent on phantom dimensions.

To evaluate the results the planar dose distributions in each phantom obtained from PCT and the corresponding slice from CBCT were extracted and compared by gamma analysis. The results are shown in Figure 3.9. In the 4-window comparison panel of MapCHECK™ software, the dose distributions obtained from PCT and CBCT are in the top two panels. In the lower-left panel, the comparison dose map (denoted as PCT-CBCT in Figures 3.9a and 3.9b) indicates all the measurement points that are not in agreement with 3%/3mm criteria. Further the points that record a lower value are shown in blue (Figure 3.9b). In the lower-right panel, depth-dose profiles along the high-dose gradient region between the PCT and CBCT dose distributions are compared. The gamma analysis comparison shows a dose discrepancy within $\pm 1\%$ using Catphan calibration curve 2. The same procedure was adopted for the other four phantoms. For the Norm body phantom, there is a shift in the isodose lines that causes variations in dose of up to 5% (figure 3.8d) when density calibration curve 1 is used. However, the dose discrepancy is reduced to within 3% (Figure 3.9b) by using Catphan calibration curve 2. The overall results show that Catphan calibration curve 2 gives better agreement with PCT than curve 1.

Figure 3.10 shows PCT and CBCT axial slices of the two prostate studies with isodose curves superimposed. A comparison of DVHs of the prostate and femoral heads is presented in Figure 3.11. The gamma analysis with 3%/3mm criteria for both the patients (Figure 3.12a and 3.12b) show 100% pass when the Catphan calibration curve 2 was used, with dose differences within $\pm 1\%$. The dose agreement remains clinically acceptable (98% pass) even with 2%/2.5 mm criteria. Catphan calibration curve 2 was used for several phantom studies to investigate various situations that limit the use of CBCT datasets in clinical treatment planning. In Figure 3.7, it was shown that the PCT dose distribution of Catphan agrees well with that of CBCT using Catphan calibration curve 2 (Figure 3.7a1 and a2) except for Norm body phantom (Figure 3.7b1 and b2) where the difference is high.

This difference in DVH for Norm body phantom is further evaluated quantitatively using gamma analysis (Figure 3.9b).

The dose calculated using CBCT calibration curve 1 and curve 2 was compared with PCT datasets to study the status of Varian OBI CBCT for treatment planning without correcting for HU values. The doses agreed well (within $\pm 1\%$) with that of PCT if CBCT Catphan calibration curve 2 was utilized for dose computations. However, there was a maximum dose discrepancy of 3% (Figure 3.9b) on the Norm body phantom with a diameter twice as large as that of the calibration phantom. The reason is, in order to cover large FOVs; half-fan acquisition mode was adopted. In this mode, the detector is shifted laterally to the centre of rotation to cover the large volume. As a consequence, the central part of the phantom is scanned over a complete 360° rotation while the peripheral parts are scanned only over a 180° half-rotation.

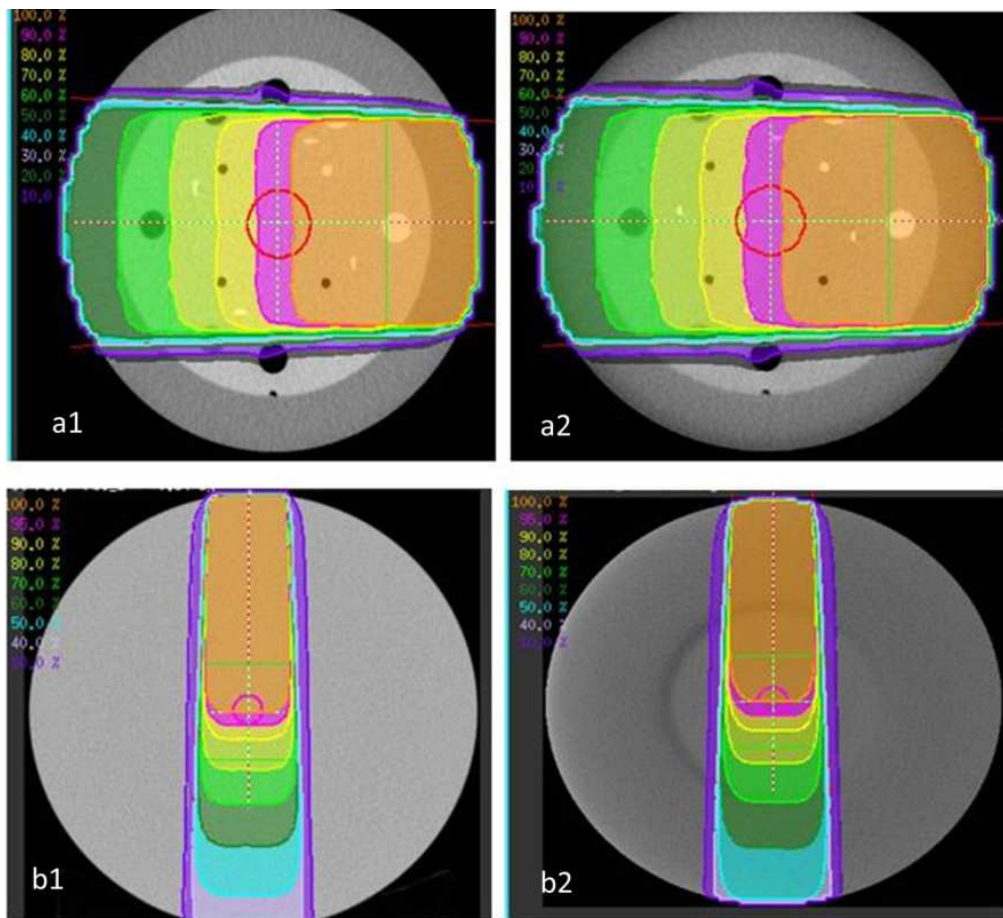


Figure 3.7 Dose distributions on an axial slice of Catphan acquired using PCT (a1) and CBCT using curve2 (a2); on an axial slice of Norm body phantom acquired using PCT (b1) and CBCT using curve2 (b2)

This results in an artefact in the images of the Norm body phantom (background of Figure 3.5c) leading to underestimation of the overall HU values during cone-beam reconstruction. This relative variation in HU values when compared to those obtained with PCT causes a shift in the isodose curves, resulting in pronounced variation ($\pm 3\%$) in the dose distributions when compared to those obtained with PCT. Although HU profiles are stable for Norm body phantoms (Figure 3.5c), there is a maximum dose discrepancy of up to 3%.

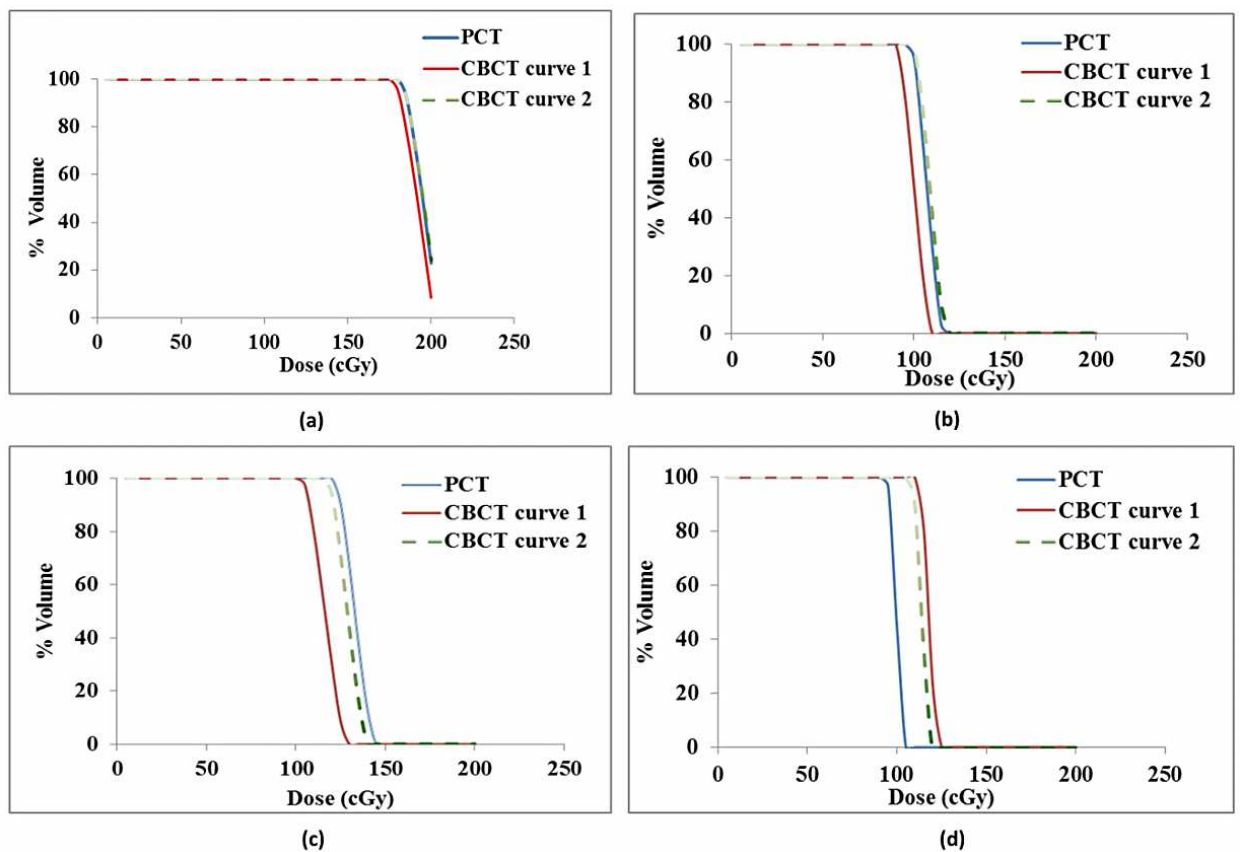


Figure 3.8 DVHs comparison of the PTV for (a) Density phantom, (b) Water phantom, (c) Catphan and (d) Norm body phantom obtained with PCT, CBCT using density calibration curve (curve 1) and by using Catphan calibration curve (curve 2)

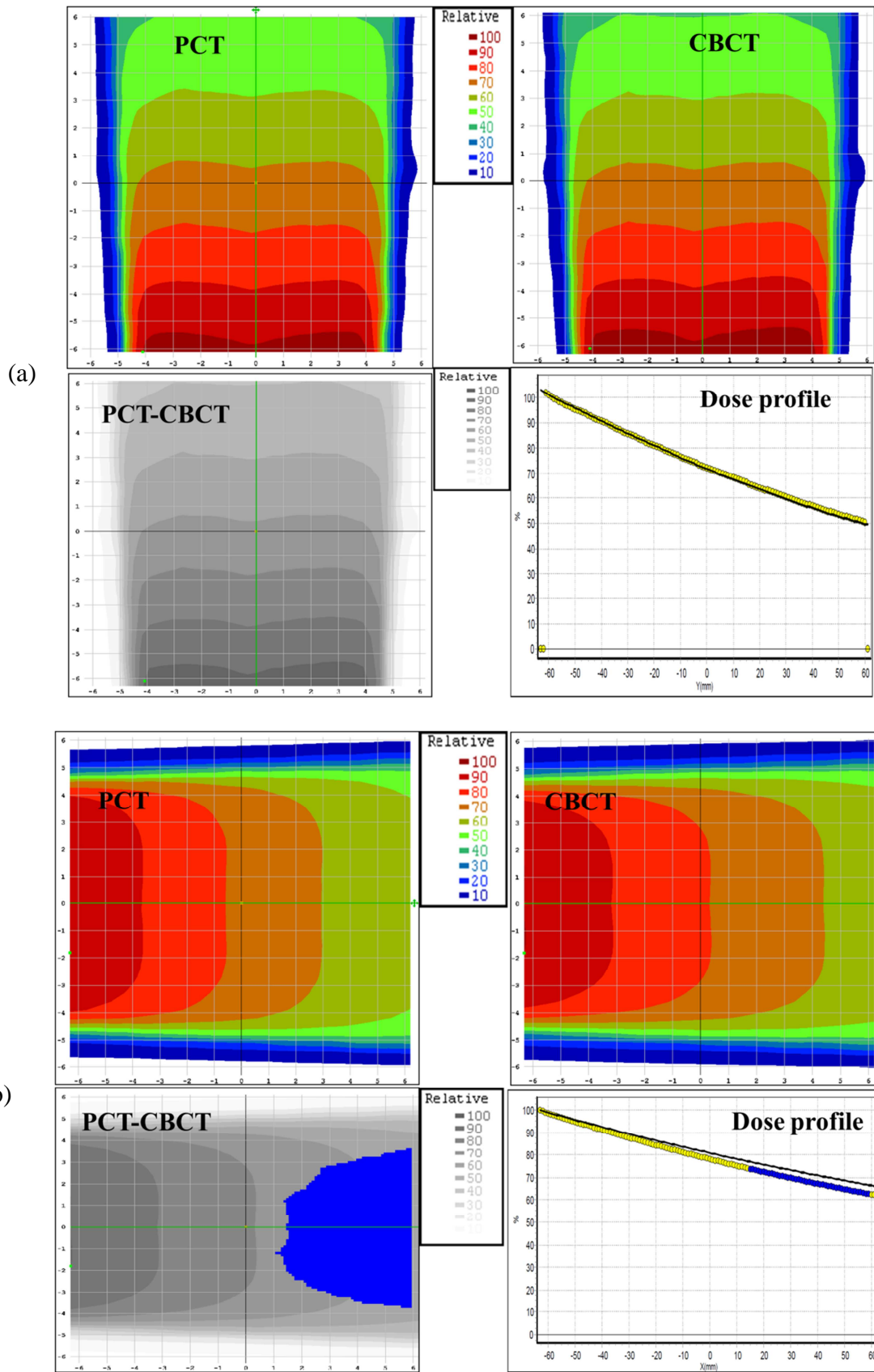


Figure 3.9 Comparison of PCT and CBCT dose distributions and dose profiles using gamma map for
 (a) Catphan and (b) Norm body phantom using Catphan calibration curve 2

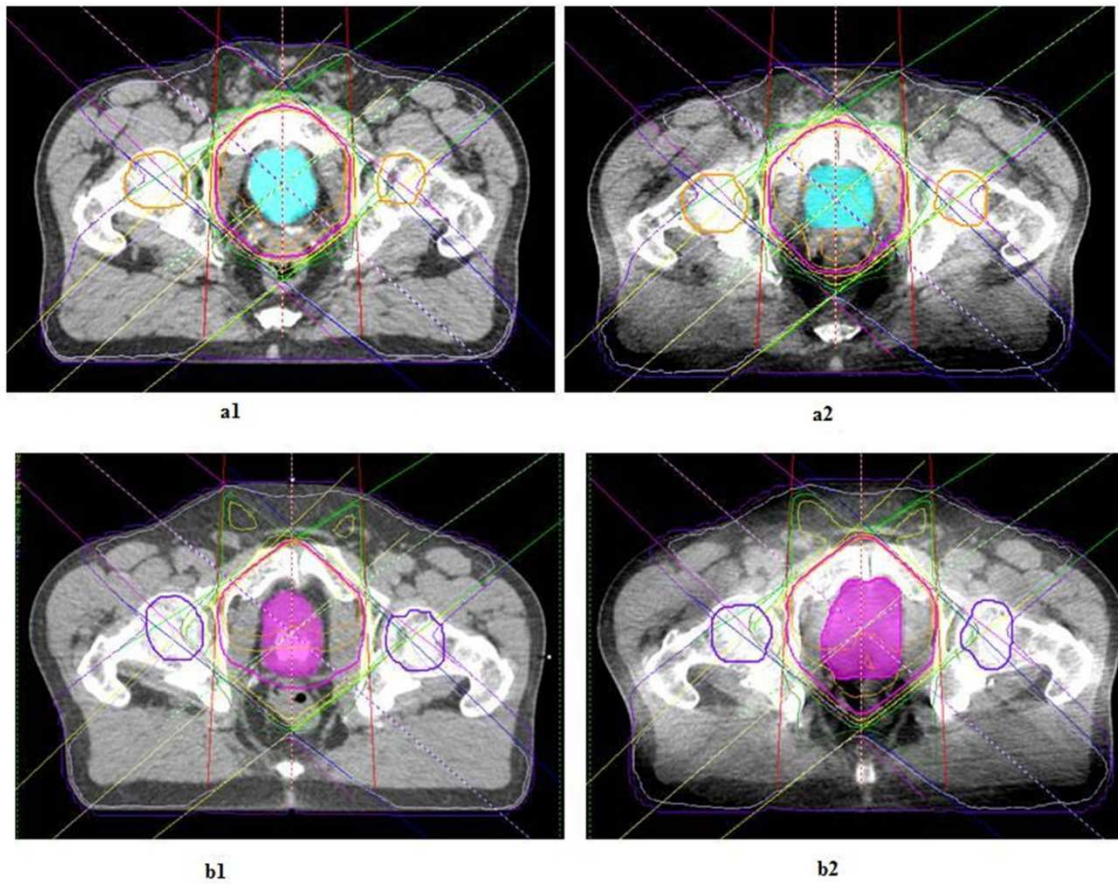


Figure 3.10 Dose distributions on an axial slice of patient A (a1 and a2) and patient B (b1 and b2) prostate cases using PCT and CBCT respectively

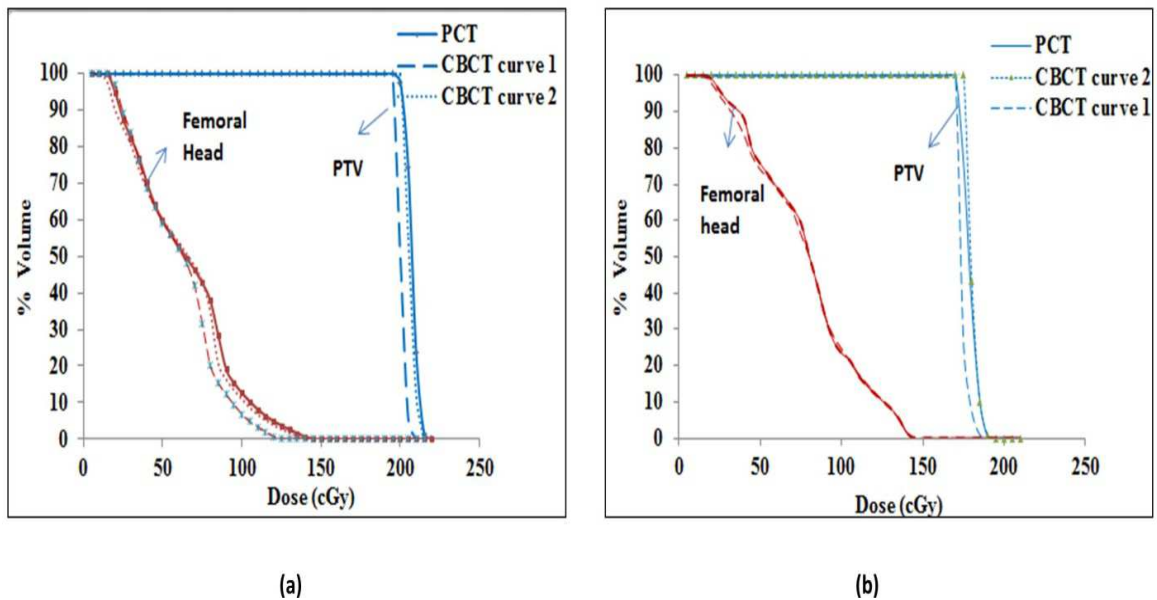


Figure 3.11 DVHs comparison of the PTV and Femoral head for two prostate patients (a) Patient A and (b) Patient B, obtained with PCT, CBCT using density calibration curve (curve 1) and using Catphan calibration curve (curve 2)

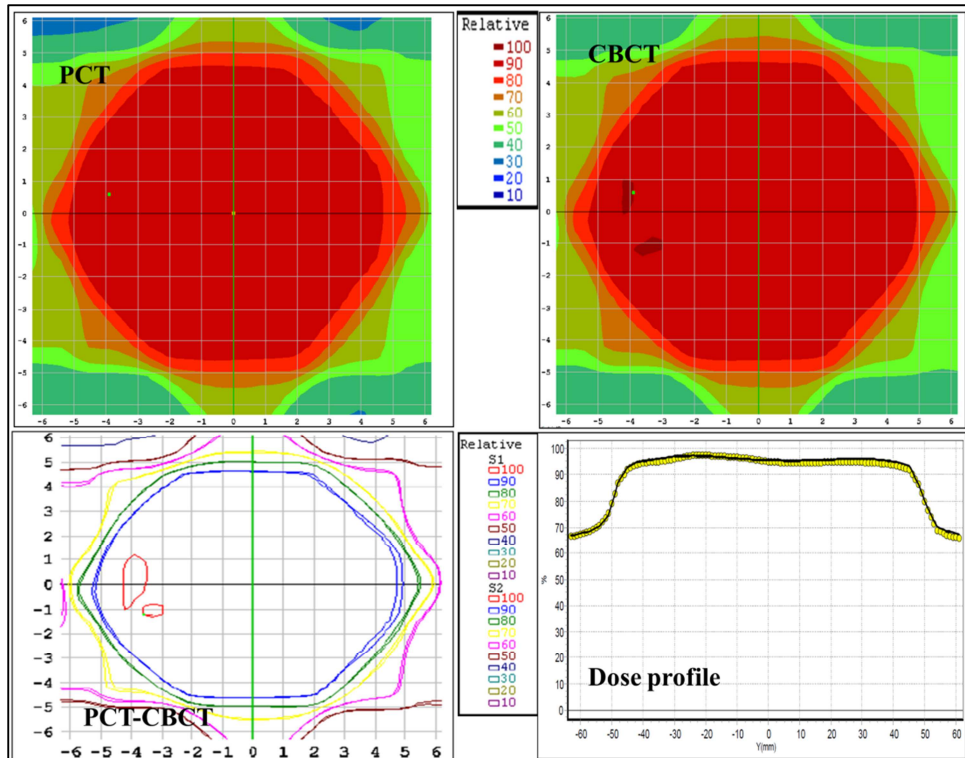


Figure 3.12a Dose distribution, gamma map and dose profile comparisons for patient A using MapCHECK

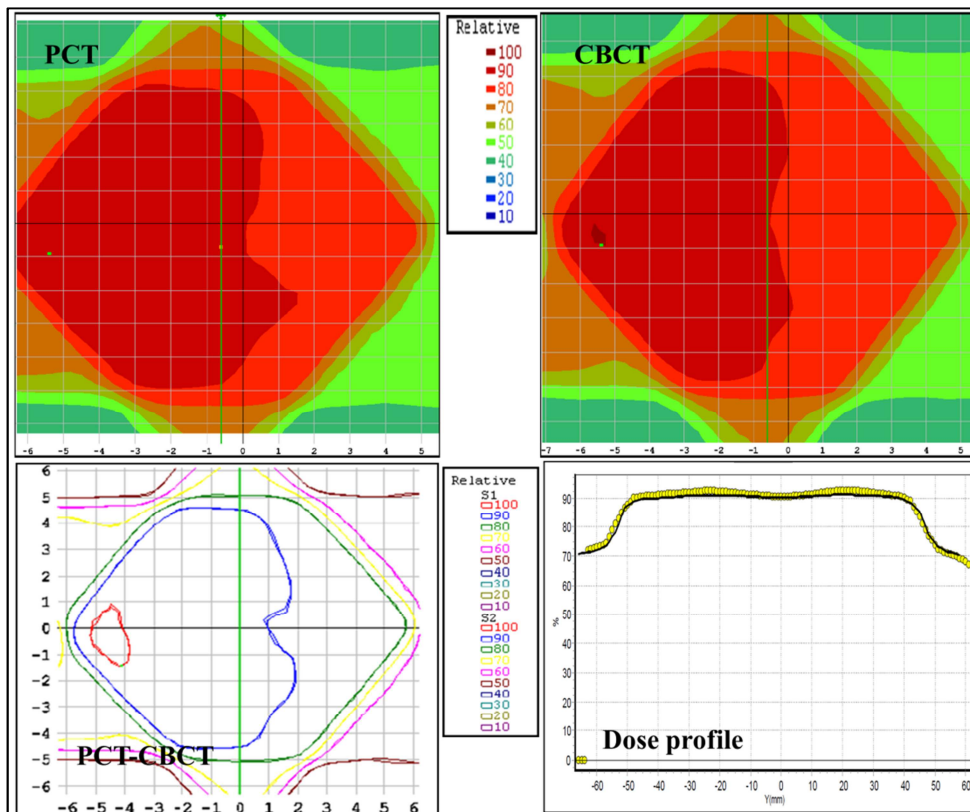


Figure 3.12b Dose distribution, gamma map and dose profile comparisons for patient B using MapCHECK

In the patient studies, the resultant dosimetric deviations were found to be $\pm 5\%$ in the high-gradient dose region for both the cases when the CBCT calibration curve 1 was used. The discrepancy was reduced by using the CBCT calibration curve 2. This further confirms that the use of suitable calibration curves results in better dose agreement. Thus, for major clinical treatment sites such as the prostate, lung and head and neck, at least three different CBCT calibrations curves based on dimensions of that region are required for planning the corresponding anatomical site.

3.6 Conclusions

In order to use CBCT image sets for dose calculations, reliable HU-density calibration is required. This study showed that the density phantom used for PCT calibration is not appropriate for CBCT dose calculations. Treatment plans created with CBCT images using CBCT calibration curve 2 (using Catphan) agreed well with PCT plans. However the CBCT dose distributions were found to depend on the phantom dimensions. This indicates the need for calibration phantoms that match the size of the treatment site to be imaged (e.g., prostate). When CBCT HU calibration curves that are appropriate for a particular treatment site are used for planning, CBCT can potentially be used for adaptive radiotherapy treatment planning. This work has been published recently (Srinivasan, Mohammadi & Shepherd 2014).

Chapter 4

Investigation of Effect of Reconstruction Filters on Cone-Beam Computed Tomography Image Quality

4.1 Introduction

Cone-beam CT using kV imagers integrated with linear accelerators is now widely used in verifying patient position during radiation therapy using its 3D imaging capabilities. Current CBCT acquisition protocols have lowered tube current to keep the imaging dose to a minimum. This affects the usability of CBCT data sets in treatment planning by reducing the soft tissue contrast and accuracy of HU values. If CBCT datasets are to be useful for treatment planning and ART (refer chapter 3), optimal image quality is essential to localise the position of the tumour in 3D and to register any changes in tumour and patient anatomy during the treatment. For disease sites like lung, liver and prostate, where intrafractional motion is significant, fusion of CBCT images with PCT images based on soft tissue anatomy can be performed using deformable image registration algorithms (Elstrom et al. 2010; Lawson et al. 2007). However, the accuracy with which a deformable registration algorithm can recover the deformations depends on image quality.

A quality assurance (QA) program for image quality of CBCT guidance has been established in order to address the unique performance of each CBCT system (Bissonnette, JP, Moseley & Jaffray 2008). This QA tool helps to demonstrate the high linearity of HU values and the uniformity and spatial resolution of several CBCT systems, and provides a tolerance limit for each parameter. Several studies have evaluated the image quality characteristics such as noise and spatial resolution of CBCT based on the QA program. In these studies, the image quality parameters have been compared for different tube current settings (Kamath et al. 2011) and different reconstruction methods (Elstrøm et al. 2011). Many studies (Chen et al. 2008; Endo et al. 2001; Jaffray & Siewerdsen 2000; Yang, K et al. 2008) have evaluated the CBCT image quality when influenced by noise and resolution. However, the relationship between image noise and resolution in a clinical CBCT system due to the effect of reconstruction filters has not been evaluated so far. In CBCT, apart

from scanner geometry and characteristics (tube voltage, tube current, focal spot size and ms), the reconstruction filters also influence the image quality with greater effects on noise and resolution than on image uniformity (Kalender 2011). Hence it is essential to assess the effect of different reconstruction filters on noise and spatial resolution. This study uses the Varian OBI CBCT images of the phantom Catphan 504. Image quality parameters of CNR, HU uniformity, pixel stability and spatial resolution were assessed for full-fan and half-fan acquisition modes of CBCT using different reconstruction filters. The resultant images were evaluated quantitatively to examine the effects of reconstruction filters on image quality.

4.2 Catphan

The Catphan® 504 phantom (The Phantom Laboratory, New York, USA) is a cylindrical phantom build of several modules that can be used to measure various image quality indices. Figure 4.1 illustrates the Catphan® 504 model. The phantom has a diameter of 20 cm and length of 20 cm. The CTP 404, CTP 486 and CTP 528 modules of Catphan were used for this study. CTP404 module containing inserts of different densities was used for HU linearity - this includes air, polystyrene, low-density polyethylene, acrylic, Delrin and Teflon with densities in the range 0-2.16 g/cm³. CTP 486 has a uniform water equivalent disk of 150 mm diameter to evaluate HU uniformity. CTP 528 was used to evaluate spatial resolution with up to 21 lp/cm.

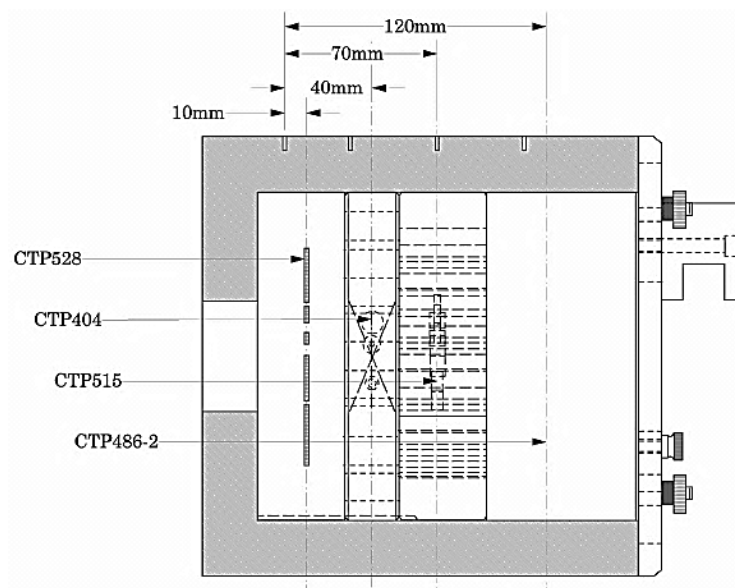


Figure 4.1 Illustration of Catphan® 504 phantom

4.3 Method of Acquisition

All scans presented in this study were acquired using Varian OBI integrated with Clinac iX at 90° with respect to the treatment beam (OBI version 1.5, Varian Medical Systems, Palo Alto, CA). Imaging in full-fan mode used 100 kVp, 20 mA and 20 ms to acquire a total of 360 projections during the 200° gantry rotation. For half-fan mode, the detector is offset by 14.8 cm and acquires 655 projections during a 360° gantry rotation (refer section 3.2.1). Imaging in half-fan mode used 125 kVp, 80 mA and 13 ms. A full- or half-bow-tie filter was added to the kV source while scanning depending on the acquisition mode.

4.4 Procedure for Analysis

The 2D projection data of the Catphan 504 phantom were acquired four times for both full-fan and half-fan modes of CBCT. Using the Radon transform in Matlab (The MathWorks Inc., Natick, MA), the sinograms of the image intensity along the radial line for the specified angle were generated. These sinograms were then utilised for reconstructing the images in Matlab using different filters. The various steps involved in this study were described below:

1. Acquisition of CBCT projections of Catphan phantom
2. Reconstruction of CBCT projections using FDK algorithm
3. Export of CBCT DICOM files to Matlab
4. Generation of sinograms using Radon function
5. Application of five different reconstruction filters on sinograms
6. Backprojection of filtered sinograms

Five different filters (Ram-Lak, Shepp-Logan, Cosine, Hamming and Hann) were applied during back projection to manipulate the reconstructed images. Each filter was defined by modifying the ideal Ramp filter (which is the Ram-Lak filter) in the spatial frequency domain according to the window needed to deemphasize high frequencies (Kak 2001). For a function H of the form shown in equation 4.1,

$$H(\omega) = |\omega|W(\omega) \quad \dots\dots\dots (4.1)$$

ω is the spatial frequency and $W(\omega)$ is defined for each filter as follows:

Ram-Lak filter: $\text{rect}(\omega/2)$

Shepp – Logan filter: multiplies the Ram-Lak filter by a sinc function, $\text{sinc}(\omega/2)$,

Cosine filter: multiplies the Ram-Lak filter by a cosine function, $\cos(\omega/2)$,

Hamming filter: multiplies the Ram-Lak filter by a Hamming window, $0.54 + 0.46 \cos(\omega)$,

Hann filter: multiplies Ram-Lak filter by a Hann window, $0.5 + 0.5 \cos(\omega)$

The frequency response curves for various reconstruction filters are given in Figure 4.2. Image quality analysis was performed using ImageJ software (National Institute of Health, USA). The various tests performed and the Catphan modules involved in these tests are given below.

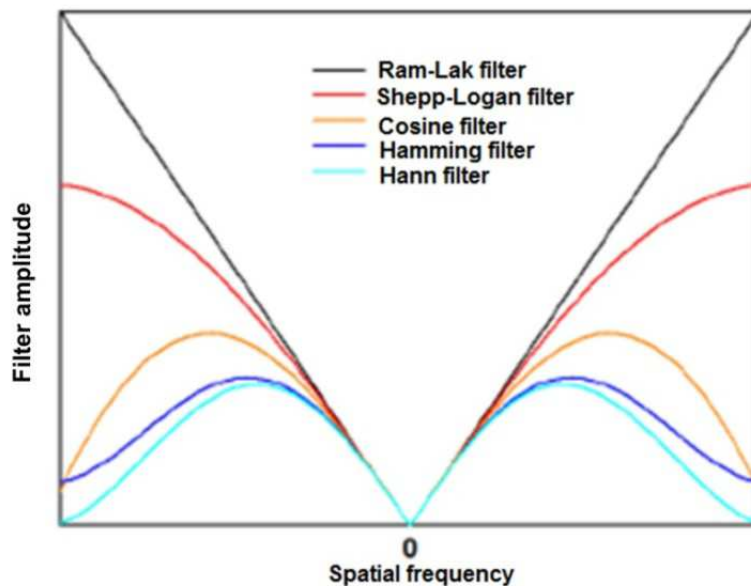


Figure 4.2 Frequency response curves for various reconstruction filters

4.4.1 Pixel Stability

The reconstructed slice of CTP 404 module of the Catphan was used to assess the pixel value stability for each of the inserts. The means and standard deviation of seven different inserts were computed. Ideally, the mean value computed for the region of interest is indicative of HU values and the SD represents noise (σ) in that region.

4.4.2 HU Uniformity

The CTP 486 module of the Catphan containing a homogenous material was used to quantify the image uniformity. Circular ROIs, each containing about 300 pixels were selected at the centre and four peripheral regions on the same slice of the Catphan image

(Figure 4.3). The mean HU values of each ROI was calculated to evaluate the uniformity of the image.

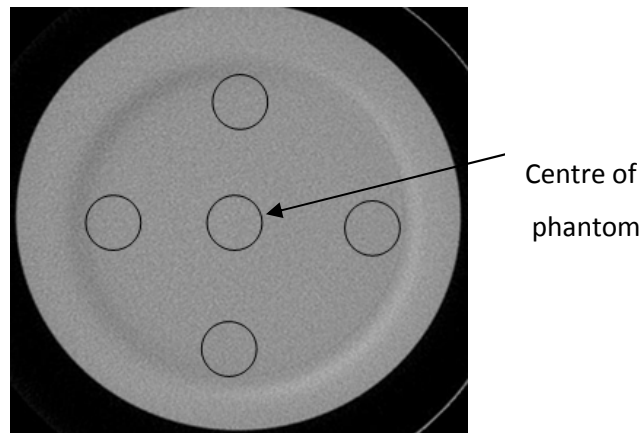


Figure 4.3 Image of CTP 486 module of Catphan with ROIs drawn

The difference of pixel values from the peripheral region to the centre of an image slice defines the image uniformity. Thus the image uniformity is evaluated using the Uniformity Index (UI) as defined in equation 4.2.

$$UI = \frac{(HU_{\text{periphery}} - HU_{\text{centre}})}{HU_{\text{centre}}} \times 100 \quad \dots\dots (4.2)$$

where $HU_{\text{periphery}}$ is the average HU value of all the four peripheral ROIs and HU_{centre} is the average HU value from the central ROI. If the UI is positive, this is indicative of the “cupping” artefact, where the HU numbers in the centre are lower than at the periphery of the phantom. If the UI is negative, then it would indicate the “capping” artefact which occurs due to overcompensation for the beam hardening effects (refer section 2.5.1). Profiles generated over the uniform section of the Catphan for two different modes of CBCT acquisition were analysed for image uniformity.

4.4.3 Contrast-to-Noise Ratio

In this study, CNR is defined as the difference between the average HU values in the insert and background, divided by average noise of the insert (σ_{insert}) and the background ($\sigma_{\text{background}}$). CNR is calculated for an insert as follows:

$$CNR = 2 \times \frac{|HU_{\text{insert}} - HU_{\text{background}}|}{\sigma_{\text{insert}} + \sigma_{\text{background}}} \quad \dots\dots (4.3)$$

4.4.4 Spatial Resolution

The CTP 528 module containing 1 through 21 lp/cm was used to evaluate the spatial resolution. The Modulation Transfer Function (MTF) which represents a measure of the spatial resolution in the imaging system was evaluated according to the method outlined by Droege et al (1982). In this study the MTF was calculated based on the change of density across each line pair pattern using equation,

$$MTF = \frac{\frac{\pi}{\sqrt{2}} * \sqrt{M^2 - N^2}}{|CT_1 - CT_2|} \dots\dots\dots (4.4)$$

where M is the SD within the line pair patterns, N is the SD within a uniform region of the image and CT_1 & CT_2 are the mean pixel values within uniform regions of different thickness or densities. The resolution obtainable for a given system is specified at 50% and 10% MTF i.e., frequency at which the contrast has dropped to 50% and 10% respectively of the maximum value obtained at 0 lp/cm.

4.5 Results

HU values were calculated independently for each of the tests and for each filter.

4.5.1 Pixel Stability

The measured average pixel values for 0.5 cm diameter circular ROIs in various inserts of the Catphan module, CTP 404, for full-fan and half-fan modes are reported in Table 4.1. The pixel values of inserts were stable when mAs were varied for OBI except for one or two outliers. In general, full-fan mode measures a higher HU difference compared to estimated HU values. Also it is seen that with increase in HU values, i.e., with increase in relative densities, the difference in HU between the measured and expected values increases. The highest density insert, Teflon, showed huge HU difference of 117 HU for full-fan mode when compared to the expected values. However, the effect of different reconstruction filters on measured HU values was not significant. Hann and the Hamming filter give the least noise with the SD reduced by more than 65% relative to the default Ram-Lak filter.

4.5.2 HU Uniformity

The Uniformity Index (UI) was measured using the circular ROIs defined at the centre and the periphery of the phantom.

Table 4.1 Insert materials present in Catphan CTP 404 modules and their expected and measured HU values

(a) half-fan mode

Inserts	Expected HU (HU _{ex})	Ram-Lak filter			Hamming filter			Shepp-Logan filter			Cosine filter			Hann filter		
		Measured HU (HU _{mea})	HU* difference	SD**	Measured HU (HU _{mea})	HU difference	SD	Measured HU (HU _{mea})	HU difference	SD	Measured HU (HU _{mea})	HU difference	SD	Measured HU (HU _{mea})	HU difference	SD
Air	-1000	-984.94	-15.0	14.50	-993.7	-6.30	5.90	-985.70	-14.30	13.01	-982.39	-17.61	9.74	-984.36	-15.64	5.50
PMP	-200	-189.46	-10.54	14.72	-193.74	-6.26	5.75	-192.30	-7.70	10.12	-191.38	8.62	8.78	-190.88	-9.12	5.28
LDPE	-100	-98.83	-1.17	17.80	-104.71	4.71	5.18	-101.90	1.90	10.84	-101.89	1.89	8.80	-103.09	3.09	5.07
Poly-styrene	-35	-44.81	9.81	11.99	-50.21	15.21	4.11	-49.90	14.90	9.03	-49.18	14.18	6.34	-50.11	15.11	4.02
Acrylic	120	105.94	14.06	15.14	103.94	16.06	4.67	102.75	17.25	8.68	101.58	18.42	7.09	101.94	18.06	4.60
Delrin	340	323.77	16.23	15.16	316.05	23.95	5.70	312.70	27.30	15.09	316.34	23.66	8.66	314.84	25.16	5.63
Teflon	990	944.29	45.71	19.76	940.32	49.68	4.70	916.49	73.51	18.58	936.77	53.23	8.68	937.19	52.81	4.59

*HU difference = HU_{ex} - HU_{mea}

**SD is the noise measured within each insert

(b) full-fan mode

Inserts	Expected HU (HU _{ex})	Ram-Lak filter			Hamming filter			Shepp-Logan filter			Cosine filter			Hann filter		
		Measured HU (HU _{mea})	HU * Difference	SD**	Measured HU (HU _{mea})	HU difference	SD	Measured HU (HU _{mea})	HU difference	SD	Measured HU (HU _{mea})	HU difference	SD	Measured HU (HU _{mea})	HU difference	SD
Air	-1000	-969.21	-30.79	37.04	-977.28	-22.72	22.72	-967.00	-33.00	33.63	-967.00	-33.00	25.89	-961.67	-38.30	21.59
PMP	-200	-211.46	11.46	39.37	-215.88	15.88	27.00	-212.85	12.85	39.71	-216.59	16.59	31.86	-215.5	15.50	25.71
LDPE	-100	-120.38	20.38	38.40	-120.98	20.98	22.05	-120.23	20.23	35.24	-121.20	21.20	27.10	-121.97	21.97	21.09
Poly-styrene	-35	-58.72	23.72	41.82	-57.92	22.92	27.08	-56.96	21.96	38.76	-56.23	21.23	31.11	-57.04	22.04	25.14
Acrylic	120	95.42	24.58	45.76	96.78	23.22	25.58	97.21	22.79	36.21	93.81	26.19	28.02	97.37	22.63	24.33
Delrin	340	289.66	50.34	41.13	284.41	55.59	21.24	283.36	56.64	33.3	284.98	55.02	26.41	284.66	55.34	20.24
Teflon	990	872.74	117.26	52.21	858.65	131.35	26.25	860.39	129.6	39.05	860.14	129.86	31.02	859.84	130.16	24.28

*HU difference = HU_{ex} - HU_{mea}

**SD is the noise measured within each insert

Table 4.2 shows the UI measurements on a reconstructed slice of Catphan using five different filters in full- and half-fan modes. It is observed that for both full-fan and half-fan modes, HU values at the peripheral ROI were greater than that of central ROI, so that there is a ‘cupping artefact’. The effect was more pronounced for full-fan scans. In general, the image uniformity of each mode was found to be minimally affected with different reconstruction filters.

Table 4.2 Uniformity Index measurements on a reconstructed slice of Catphan using five different filters in full- and half-fan modes

Filters	Uniformity Index (UI) (%)	
	Full-fan mode	Half-fan mode
Ram-Lak	3.14 ± 4.7	0.36 ± 4.39
Hamming	2.15 ± 3.07	0.48 ± 3.01
Shepp-Logan	3.59 ± 4.62	0.24 ± 4.19
Cosine	3.89 ± 3.11	0.29 ± 3.53
Hann	5.89 ± 2.1	0.26 ± 2.95

The central profiles of the image uniformity module in the Catphan were produced using different acquisition modes and are shown in Figure 4.4. The profile of the image reconstructed with higher tube current was found to have smaller fluctuations than with lower tube current.

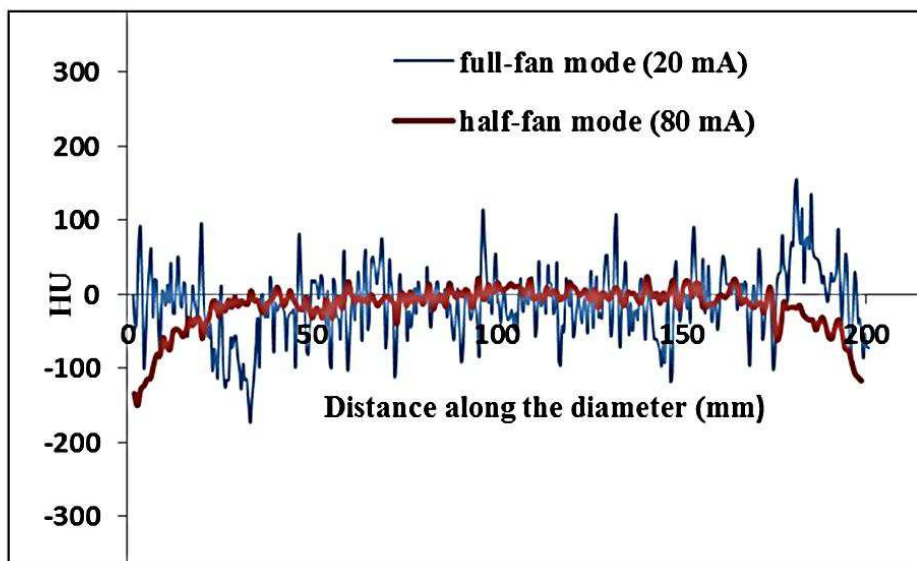


Figure 4.4 Central profiles of reconstructed axial slices for full- and half-fan mode using Ram-Lak filter

4.5.3 Contrast-to-Noise Ratio

The axial slice of the Catphan reconstructed using the Ram-Lak and Hamming filters for full- and half-fan mode is shown in Figure 4.5.

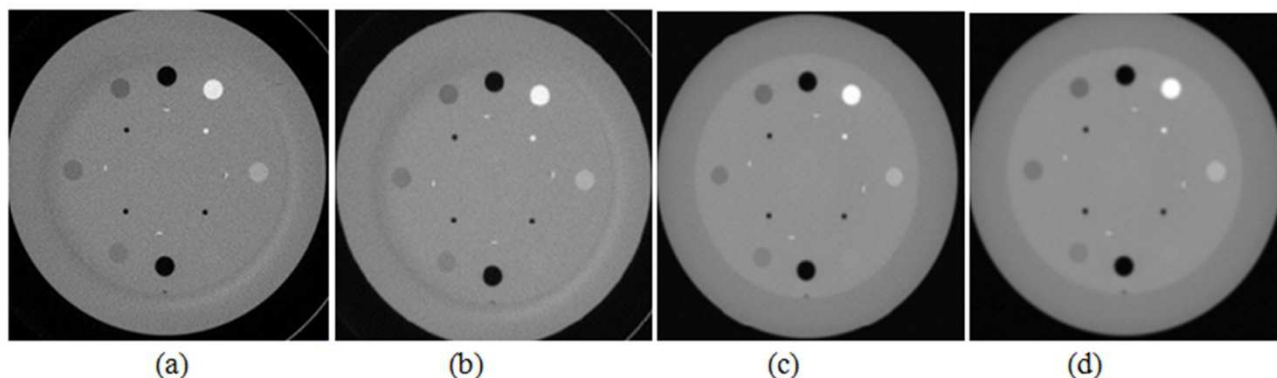


Figure 4.5 CTP 404 slice of Catphan reconstructed for full- fan (a and b) and half-fan (c and d) modes using Ram-Lak (a and c) filter and Hamming filter (b and d)

The CNR was calculated for the acrylic insert (since it has low effective atomic number similar to water) using five different filters and is shown in Table 4.3. It was found that, in general, CNR was higher for half-fan mode by a factor of 3-4 times than for full-fan mode. In half-fan mode, the Hamming filter gives the least noise with the CNR higher by a factor of 2.7 times when compared with the Ram-Lak filter and higher by a factor of 1.5 to 2 times when compared with Shepp-Logan, Cosine and Hann filters. In full-fan mode, the Hamming and the Hann filter yields a higher CNR by a factor of 2 when compared to Ram-Lak filter.

4.5.4 Spatial Resolution

Figure 4.6 shows axial slices of the reconstructed CTP 528 module with line pairs using different filters. MTF measurements using five different filters for full- and half-fan modes are shown in Table 4.4. It was found that the spatial resolution of the image at 10% MTF was decreased by 25% when the tube current was increased by four times from full-fan mode (for head protocol) to half-fan mode (for Pelvis protocol).

The relation between MTF and line pairs per centimetre for five different reconstruction filters for half-fan and full-fan modes are shown in Figures 4.7 (a) & (b) respectively.

Table 4.3 Summary of contrast-to-noise (CNR) measurements for (a) half-fan and (b) full-fan acquisition mode of CBCT using five different filters

(a) half-fan mode

Filters	ROI	Mean HU	SD (σ)	CNR
Ram-Lak filter	Acrylic insert	107.11	14.69	2.11
	background	76.32	14.57	
Hamming filter	Acrylic insert	103.94	4.67	5.76
	background	74.35	5.6	
Shepp-Logan filter	Acrylic insert	102.75	8.69	2.81
	background	77.4	9.38	
Cosine filter	Acrylic insert	101.58	7.09	3.50
	background	78.33	6.2	
Hann filter	Acrylic insert	100.39	7.3	3.39
	background	76.88	6.57	

(b) full-fan mode

Filters	ROI	Mean HU	SD (σ)	CNR
Ram-Lak filter	Acrylic insert	96.65	58.17	0.506
	background	69.43	49.44	
Hamming filter	Acrylic insert	99.78	24.1	1.286
	background	69.77	22.59	
Shepp-Logan filter	Acrylic insert	96.72	37.45	0.758
	background	69.14	35.29	
Cosine filter	Acrylic insert	90.89	32.72	0.742
	background	66.97	31.75	
Hann filter	Acrylic insert	90.87	31.79	0.826
	background	65.26	30.25	

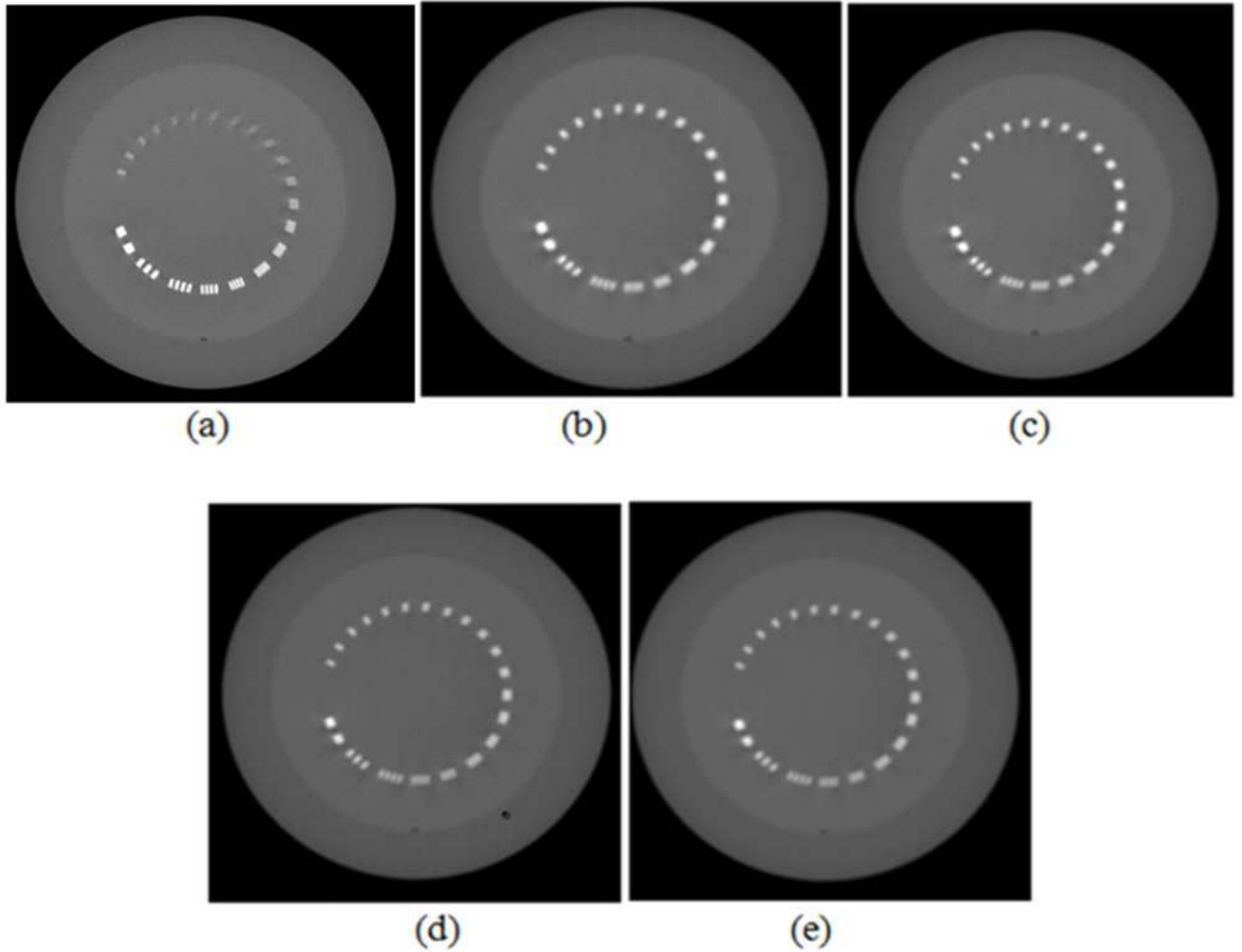


Figure 4.6 CTP 528 slice of Catphan reconstructed using (a) Ram-Lak, (b) Hamming (c) Shepp-Logan, (d) Cosine and (e) Hann filters showing the number of line pairs seen.

Table 4.4 Summary of the MTF measurement for (a) half-fan and (b) full-fan CBCT imaging protocol using five different reconstruction filters. The frequencies corresponding to MTF values of 0.5 and 0.1 are shown.

(a) half-fan mode

	Ram-Lak filter	Hamming filter	Shepp-Logan filter	Cosine filter	Hann filter
$f_{0.5}$ (cm^{-1})	2.3	2.0	2.2	2.1	1.8
$f_{0.1}$ (cm^{-1})	5.6	4.4	5.4	4.6	4.0

(b) full-fan mode

	Ram-Lak filter	Hamming filter	Shepp-Logan filter	Cosine filter	Hann filter
$f_{0.5}$ (cm^{-1})	3.6	3.0	3.6	3.3	3.0
$f_{0.1}$ (cm^{-1})	7.2	5.9	6.9	6.3	5.9

In both full-fan and half-fan modes, at 50% MTF, the number of line pairs measured by all the filters show minimal variation (~ 3 lp/cm for full-fan and ~ 2 lp/cm for half-fan). However, at 10% MTF, the variation in spatial resolution is larger. In half-fan mode, maximum spatial resolution was given by the Ram-Lak filter (5.6 lp/cm) and minimum (4 lp/cm) by the Hann filter. In full-fan mode, at 10% MTF, the maximum spatial resolution of 7.2 lp/cm was seen using the Ram-Lak filter and minimum was seen using the Hann filter (5.9 lp/cm). This indicates that spatial resolution is influenced by the reconstruction filter and hence the spatial resolution can be improved by using a filter that emphasizes high-frequency components.

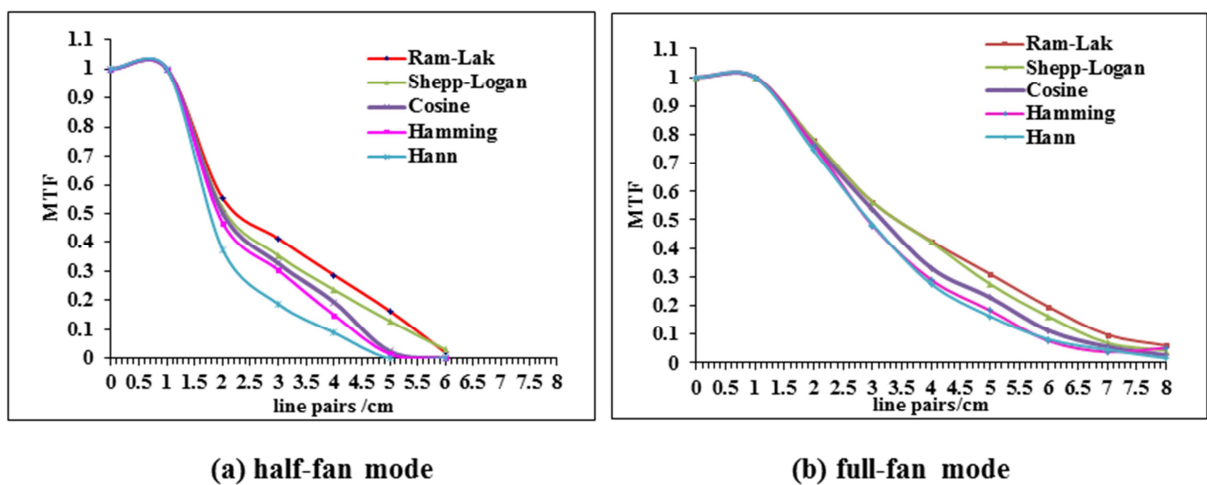


Figure 4.7 MTF calculated for (a) half-fan mode and (b) full-fan mode

4.6 Discussion and conclusion

In this study, the image quality parameters of the Varian CBCT imaging system were evaluated in a quantitative way to assess the optimum acquisition mode and reconstruction filters to be used on volumetric imaging protocols. The low-contrast resolution of an image, which distinguishes between materials of similar densities, was not studied as this depends on the reconstructed thickness of the slice.

For the studied CBCT system, the HU variation and SD was high for full-fan mode, indicating a higher noise level due to lower tube current. Comparing all five filters, the Hamming and Hann filters are found to be optimal for noise reduction as they provide the least variation ($<5\%$) in the average pixel values with CNR increased by a factor of 2.7 when compared to Ram-Lak filter. The SD of pixels was reduced by 67% compared to the

Ram-Lak as this filter emphasizes high frequencies making it sensitive to noise. However, the spatial frequency response using the Hamming and Hann filters was very low for high frequency components as they eliminate the high frequency components.

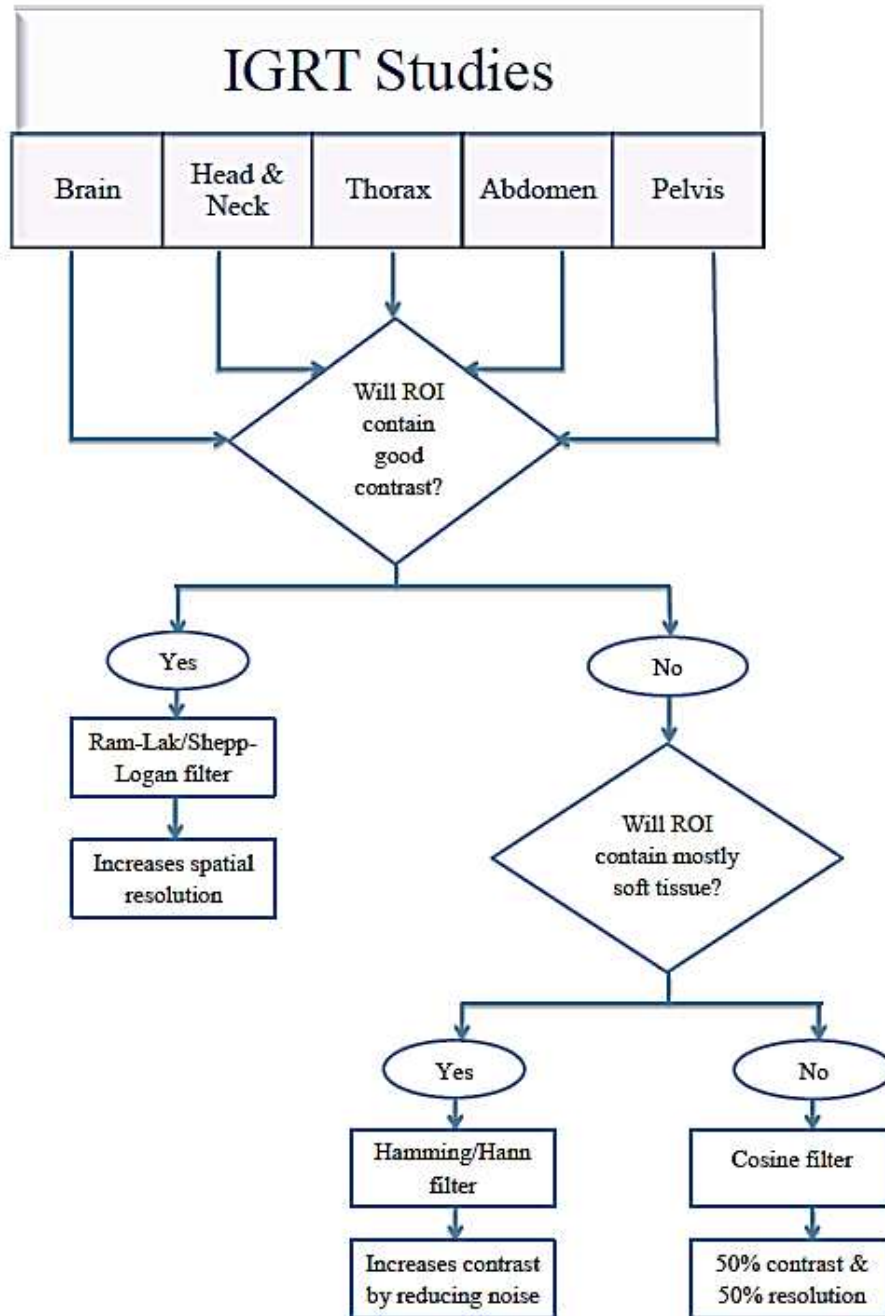


Figure 4.8 Flowchart providing guideline to choose the reconstruction filter

Comparing all five filters used, the spatial resolution at 10% MTF ($f_{0.1}$) given by the Ram-Lak is the highest and that given by the Hann is the lowest. In half-fan mode, spatial resolution at 10% MTF given by the Ram-Lak filter was 28% higher than that given by the Hann filter. From Figure 4.4, the number of projections is found to have a significant

effect on image noise but less influence on the spatial resolution. These findings show that we can improve different aspects of image quality by using different reconstruction filters and this can be used to our advantage for different treatment sites.

IGRT studies may be roughly divided into five protocols based on the anatomical site being imaged: brain, head & neck, thorax, abdomen and pelvis. The choice of different reconstruction filters for different protocols could improve image quality allowing the radiation oncologists to contour structures more effectively. Depending upon the requirements of image quality, the choice of filter can improve either spatial resolution or contrast but not both. Also depending upon the choice of filters, the tube current may be reduced to decrease the dose to patients. For example, in the thorax region, the disease site may be in the breast, chest wall or lung. In these cases there is generally high contrast already present in the images so a filter could be chosen to improve spatial resolution. In the case of abdomen, however, organs like the liver, pancreas, stomach, and bladder are soft tissues and hence the image needs to have more contrast to distinguish two regions of similar densities. The flowchart in Figure 4.8 provides a guideline in making a decision to select a suitable reconstruction filter depending upon the region of interest (ROI). For regions surrounded by bones, high spatial resolution is desired and hence Ram-Lak or Shepp-Logan filters can be used. For anatomical sites with a combination of tissues and bones, like thorax, Cosine would be an option, as it acts as a standard filter to provide balance between the spatial resolution and the contrast.

In conclusion, the image quality of full-fan and half-fan acquisition modes of CBCT was evaluated using different reconstruction filters. The results demonstrated that the improvement in the spatial resolution was accompanied by an increase in noise for different reconstruction filters and the choice of reconstruction filter is a trade-off between the two depending upon the ROI. Thus the cone-beam image quality can be improved by using appropriate reconstruction filters.

Chapter 5

Implementation of the CBCT Image Reconstruction Algorithm

5.1 Introduction

In this study, CBCT projections of Catphan in full-fan mode were acquired from a Varian Clinac iX unit. Catphan was chosen because it is a standard CT quality assurance phantom containing a variety of structures that are useful for evaluating image quality. It is also small enough to fit in the full-fan field of view. The image was reconstructed analytically based on the FDK algorithm implemented in Matlab (The MathWorks Inc., Natick, MA). The algorithm was modified extensively by adding weights to projections to account for non-equal cone angles and for data redundancy. In addition, normalisation was done using an air norm image taken at different gantry angles; this differs from Varian's procedure which uses an air norm image at only one gantry angle. The various steps involved before and after reconstruction are described in detail in sections 5.2 and 5.3.

5.2 Cone-Beam Data Acquisition and Pre-processing

5.2.1 Projection Data Acquisition

On Varian iX unit, the CBCT projections of Catphan are acquired in full-fan mode at 100kVp tube voltage and 20 mA tube current and are stored as hnd files, which is a Varian-specific compressed format. Table 5.1 shows the scan and reconstruction parameters of the Varian iX CBCT mode used in this study. The data for each projection give an array of 1024×768 unsigned 32-bit integers. The pixel values represent the sensor read out values for an x-ray beam pulse and are saved with hnd extension. The hnd files contain header information such as x-ray source and detector precise position values, gantry rotation angle and pixel resolution. This information is then read using a Matlab function, ReadHeader.m (see Appendix A- Matlab code).

As the hnd files are in compressed binary format, Matlab cannot read them unless they are decompressed. Thus the hnd files are decompressed by converting them to another Varian-

specific format (viv), using Varian’s VIVA™ (Varian Medical Systems, Palo Alto, CA) application software. These viv files are then read through a Matlab function readviv.m (see Appendix A- Matlab code). However, the viv files do not contain header information. Thus to obtain all the information needed for reconstruction, the images must be read from viv files and the headers must be read from the hnd files.

Table 5.1 Default calibrated Varian CBCT full-fan mode summarising the scan and reconstruction parameters

Scan and Reconstruction Parameters	Varian iX full-fan
CBCT mode	Standard-dose head
X-ray Voltage (kVp)	100
X-ray Current (mA)	20
X-ray millisecond (ms)	20
Gantry rotation range (degrees)	200
Number of projections	360
Bow-tie filter	Full
Reconstruction filter	Sharp
Ring Suppression algorithm	Medium

5.2.2 Normalisation of Projections

Air normalisation or Intensity normalisation is a common calibration procedure where the incident intensity of photons (I_0) without the object is measured. A CT image provides a map of attenuation coefficient (μ) by measuring the attenuation of photons along different rays through the object. In order to calculate this attenuation, the ratio of intensity of photons with (I) and without (I_0) the object must be measured.

From Lambert-Beer’s law, the linear attenuation coefficient along the given ray is calculated as given in equation 5.1,

$$\frac{I}{I_0} = \exp\left(-\int_0^x \mu dx\right) \dots\dots\dots (5.1)$$

where x is the total distance the ray traverses through the object. Hence the preliminary step in pre-processing the projections is to divide each projection matrix I by I_0 .

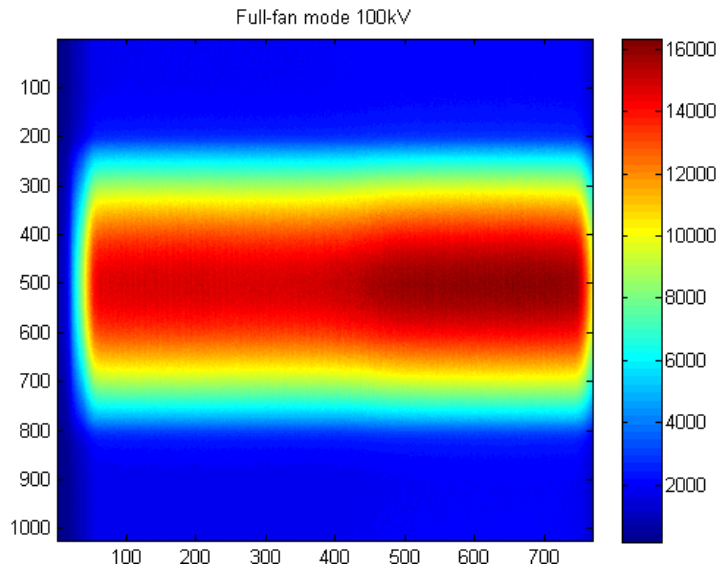


Figure 5.1 Typical I_0 calibration data (1024×768) for full-fan mode with bow-tie filter taken on a Clinac iX unit. The horizontal and vertical axes are the lateral and the longitudinal dimensions respectively. The colour bar shows the pixel values; the maximum occurs at the centre where the bow-tie filter is thinnest.

In this study, the air-normalisation procedure was performed in full-fan mode with full bow-tie filter being mounted to the x-ray source to obtain I_0 data (Figure 5.1). Recent publications (Giles et al. 2011; Zheng et al. 2011) have indicated that the single-angle air norm, combined with slight wobbling motion in the bowtie filter as the gantry rotates, is the cause of crescent-shaped artefacts commonly seen in images reconstructed on the Varian system. Hence in this study, during normalisation, each projection image (I) is divided by the I_0 image acquired from the corresponding angle to get the attenuation values.

5.2.3 Calculation of Weighting Factors

Once the image was normalised, the following weighting factors were estimated for each projection: (a) Parker weighting factor and (b) non-equal angle weighting factor.

- (a) **Parker weights:** Parker weights are applied for a set of divergent ray projections which covers 180° plus the angle of the divergent fan-beam (Parker 1982). Figure 5.2 illustrates the fan-beam scanning geometry utilised for data collection. If $p(u, \theta)$ is the projection measurement (line integral) specified by coordinates (u, θ) , where u is the relative angular position of an individual line integral from the source to a detector element and θ is the angle of rotation of source to axis segment, then the weighted data $p'(u, \theta)$ are defined as in equation 5.2.

$$p'(u, \theta) = p(u, \theta) w(u, \theta) \quad \dots\dots\dots (5.2)$$

where $w(u, \theta)$ are the Parker weights.

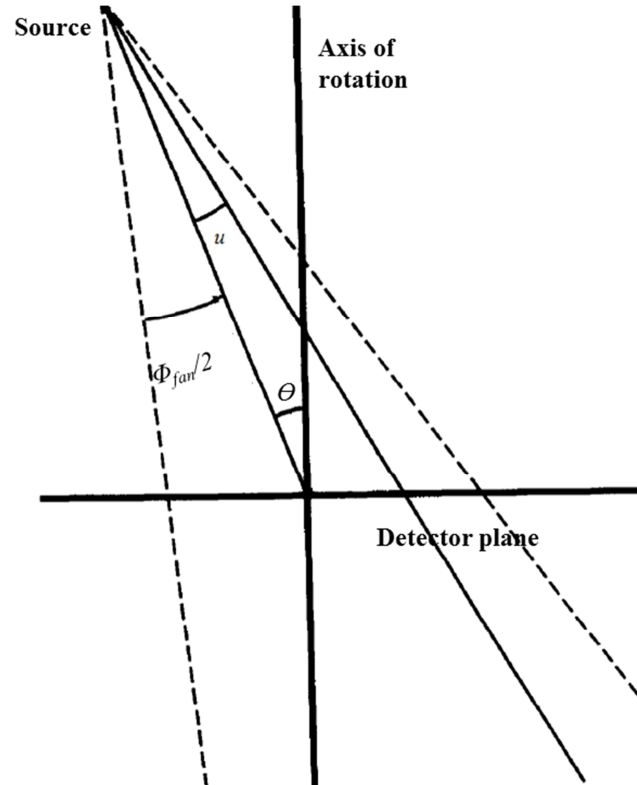


Figure 5.2 scanning geometry utilized for fan-beam

A virtual fan angle (ϕ_{fan}) defined as the difference between the angular range of the data collected and 180° is introduced. The coordinates are then calculated based on three constraints which are developed to provide smooth weighting of data in double scanned regions. The constraints on the weights are that the sum of the two weights corresponding to the same line integral must equal one; in regions of no data, the weights must equal zero; and the weights and their derivatives are required to be continuous at the boundaries. One set of weights that satisfies all three constraints is given in equation 5.3. These weights are then applied to each row of the projection data independently. (see Appendix A- Matlab code).

$$w(u, \theta) = \sin^2 \left(\frac{\pi}{4} \frac{\theta}{\left(\frac{\phi_{fan}}{2} - u \right)} \right) \quad \text{for } 0 \leq \theta \leq \phi_{fan} - 2u$$

$$w(u, \theta) = 1 \quad \text{for } \phi_{fan} - 2u \leq \theta \leq \pi - 2u$$

$$w(u, \theta) = \sin^2\left(\frac{\pi}{4} \frac{\pi + \phi_{fan} - \theta}{u}\right) \quad \text{for } \pi - 2u \leq \theta \leq \pi + \phi_{fan} \quad \dots\dots\dots (5.3)$$

(b) **Non-equal angle weighting factor:** Weighting factors for non-equal angles of cone-beam projections are applied by estimating the difference in angle between two successive projections for the entire data set. The mean of those set of angles is then used to calculate the weighting factor for each cone-beam projection by dividing each cone angle by the mean. During backprojection, each reconstruction matrix is multiplied with the weighting factor in order to account for variation in cone angles between each projection. (see Appendix A Matlab function- ‘CTRecon_Rcm’).

5.2.4 Wiener2 – Two-dimensional Adaptive Filter

Wiener filtering is a general way of adaptively filtering the noisy signals to find the best reconstruction. This adaptive filter produces better results than linear or median filtering in preserving edges and other high-frequency parts of an image. Linear filtering like average filter can remove only certain types of noise and reduces the sharpness of the image by averaging the pixels in its neighbourhood. Median filtering does a better job of removing noise than linear filtering. However, the blurring of edges still occurs. Wiener2 is more flexible in that it can be used in either Fourier basis, spatial basis or in wavelet basis. In spatial basis, the filter decomposes the image into a smoothed background image and then estimates the noise level before doing the filtering. Hence spatial adaptive filtering was applied in this study. Matlab has a built-in function for this filter called ‘Wiener2’, which is an 2D adaptive noise-removal filter that estimates the local mean ($\bar{\mu}$) and variance (σ^2) in the neighbourhood (N_{hood}) of size 3×3 around each pixel (x_{ij}) in the projection image as given in equations 5.4 and 5.5.

$$\bar{\mu} = \frac{1}{N_{hood}} \sum_{hood} x_{ij} \quad \dots\dots\dots (5.4)$$

$$\sigma^2 = \frac{1}{N_{hood}} \sum_{hood} (x_{ij} - \bar{\mu})^2 \quad \dots\dots\dots (5.5)$$

Using these estimates, a pixel-wise filter (\widehat{x}_{ij}) is created as,

$$\widehat{x}_{ij} = \bar{\mu} + \frac{\sigma^2 - v^2}{\sigma^2} (x_{ij} - \bar{\mu}) \quad \dots\dots\dots (5.6)$$

where v^2 is the noise variance; if this is not known, wiener2 uses the average of all the local estimated variances. Thus it acts as a low-pass adaptive filter, trying to compensate for loss of resolution while suppressing noise.

5.3 Cone-beam Reconstruction Algorithm

As described in chapter 2, the FDK algorithm is an extension to 3D of the 2D filtered back projection technique. It is used for reconstructing cone-beam projections acquired along a circular trajectory about a fixed isocentre. The term “back projection” refers to the projection of sensor pixel values along the ray back towards the kV source. The term “filtered” refers to the filtering part of the algorithm, where appropriately shaped filters are applied to pixel values before back projection in order to avoid excessive smoothing and to suppress aliasing. The FDK algorithm used in this study is also used in Varian reconstruction software.

5.3.1 Implementation of 3D Cone-beam Reconstruction – FDK Algorithm

The FDK code used in this study is obtained from the OSCaR software package (Rezvani 2012) developed for generating 3D reconstructions from x-ray data. The FDK code includes three major steps as described in chapter 2. They are:

- Cosine weighting of data;
- Filtering of weighted data in the frequency domain;
- 3D back projection of filtered data.

The code was further modified by adding weighting factors for data redundancy and non-equal cone-beam angles (refer 5.2.3) and by providing an option for using a bilinear interpolation method to find the detector coordinates. This resulted in computing the detector coordinates more accurately than the existing nearest neighbour method and is found in MATLAB function FDK.m (see Appendix A- Matlab code).

The reconstruction process included the following features:

- To account for non-equal angles of cone-beam projections, each projection was weighted depending upon the angular distance between two successive cone angles.
- The filter used during reconstruction was a conventional Ram-Lak filter which was applied using the available built-in Matlab function. However, an option is provided in the code to convolve with several other filters which reduce noise at the expense of image sharpness.

- During back projection, a bilinear interpolation method was used to find the detector coordinates (u,v) that are closest to the projection voxel (x,y,z) . However, an option for nearest neighbour interpolation is also provided.
- In principle, images can be reconstructed at an arbitrary set of points. For simplicity, this code allocates space for a reconstruction grid based on detector geometry. Within the limits of the reconstruction domain, the best possible grid size of 512×512 and pixel resolution with grid spacing in x and y directions of 0.488 mm and along the z direction of 1 mm were chosen to match the Varian image for comparison purposes.
- The information from the projection files was taken into account during back projection for optimal image quality.

5.3.2 Creation of C++ MEX files

Matlab functions written in C++ are called MEX files. MEX stands for Matlab Executable. Mex files are dynamically linked subroutines produced from C/C++ or FORTRAN code. A compiler and a MEX function are needed to build MEX files. The selected compiler compiles the source code into object code. The MEX function (`mex filename.cpp`) builds the binary MEX file.

The two main reasons to write a MEX file are:

- To use existing C/C++ routines in Matlab without having to recode them;
- To increase the speed more effectively on loops.

Matlab provides platform-specific extensions for MEX files. For the Linux 64-bit platform, the file extension for MEX files is `mexa64`. MEX files were created in this study in three situations. First, during FDK reconstruction, the cosine weighting of each projection was written in C++ as a source file (`getWeight.cpp`) and a MEX file (`getWeight.mexa64`) was then build using a C++ compiler. Second, during vectorised computation of back projection, a C++ source file (`getUV.cpp`) was written and the MEX file was then build by calling the MEX function (`getUV.mexa64`). Third, while implementing bilinear interpolation to find the detector coordinates, a C++ source file (`get_dR.cpp`) and the corresponding MEX file (`get_dR.mexa64`) were generated.

The creation of these MEX files have enormously speeded up the total reconstruction process and reduced the reconstruction time from almost 60 minutes to 2 minutes (See Appendix B - C++ code).

5.3.3 Hounsfield Unit Calibration

Once the 3D tomographic image is reconstructed, the HU values in the image need to be calibrated to density (as discussed in section 3.3). This calibration requires imaging of the CTP 404 module of the Catphan 504 phantom. This module contains inserts of several different materials for sensitometry measurements. Each material is assigned a nominal HU value, taken from the phantom documentation, as listed in Table 5.2 below.

Table 5.2 Nominal and measured HU values for sensitometry inserts in the CTP404 module of the Catphan 504 phantom and their relative density

Insert number	Materials	Physical density (g/cc)	Nominal HU	Measured HU \pm SD
1	Air	0	-1000	-992 \pm 30
2	Teflon	1.867	990	984 \pm 49
3	Delrin	1.319	340	367 \pm 42
4	Acrylic	1.146	120	121 \pm 43
5	Polystyrene	1.017	-35	-42 \pm 45
6	LDPE (low-density polyethylene)	0.944	-100	-88 \pm 37
7	PMP (polymethylpentene)	0.853	-200	-171 \pm 39

An axial slice containing the sensitometry inserts was taken from the reconstructed 3D image, and a region of interest of 1 cm diameter within each insert was drawn. Using the ImageJ software, the HU value averaged over 300 pixels within the region was measured. A typical reconstructed attenuation coefficient image of the CTP 404 module of the Catphan 504 phantom is shown in Figure 5.3. This image was reconstructed from a full-fan scan done on the Clinac iX unit at 100 kVp. The values shown in colour index are the attenuation coefficients in units of mm^{-1} . The pixel size is 0.488×0.488 mm, the image size is 25×25 cm^2 and the phantom diameter is 20 cm. Seven circular material inserts used in this study are numbered in the image. Clockwise from the top, the seven inserts are air, Teflon, Delrin, acrylic, polystyrene, LDPE (low-density polyethylene) and PMP (poly methyl pentene). The acrylic insert is difficult to see since it is very similar to the surrounding material. The CBCT HU calibration curve for full-fan mode, shown in Figure

5.4, was obtained using the Catphan phantom. This conversion of HU to density map was undertaken in order to use the images for determining dose distributions during planning.

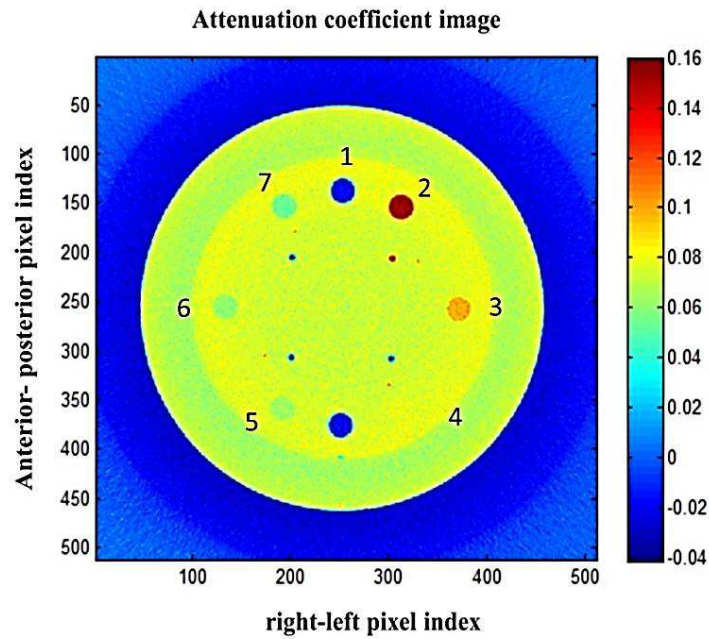


Figure 5.3 An axial attenuation coefficient image of the CTP404 module of the Catphan 504 phantom obtained from in-house reconstruction used for HU calibration

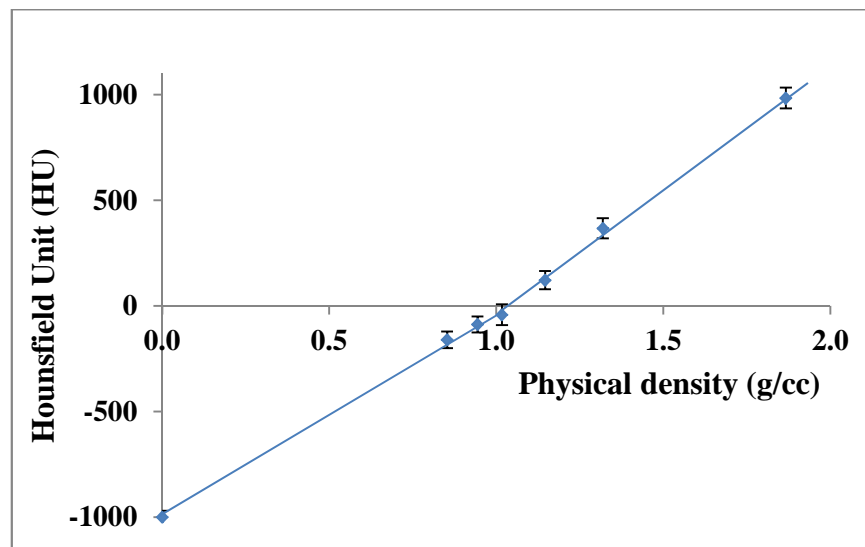


Figure 5.4 HU calibration curve for CBCT of Catphan in full-fan mode

Figure 5.5 below shows reconstructed images formed from HU values using the in-house algorithm developed for this project from two sections of the Catphan phantom: the sensitometry module (CTP 404) containing inserts of various materials and the line-pair module (CTP 528). These images were compared with Varian reconstructed images to show that the quality of the images obtained is comparable.

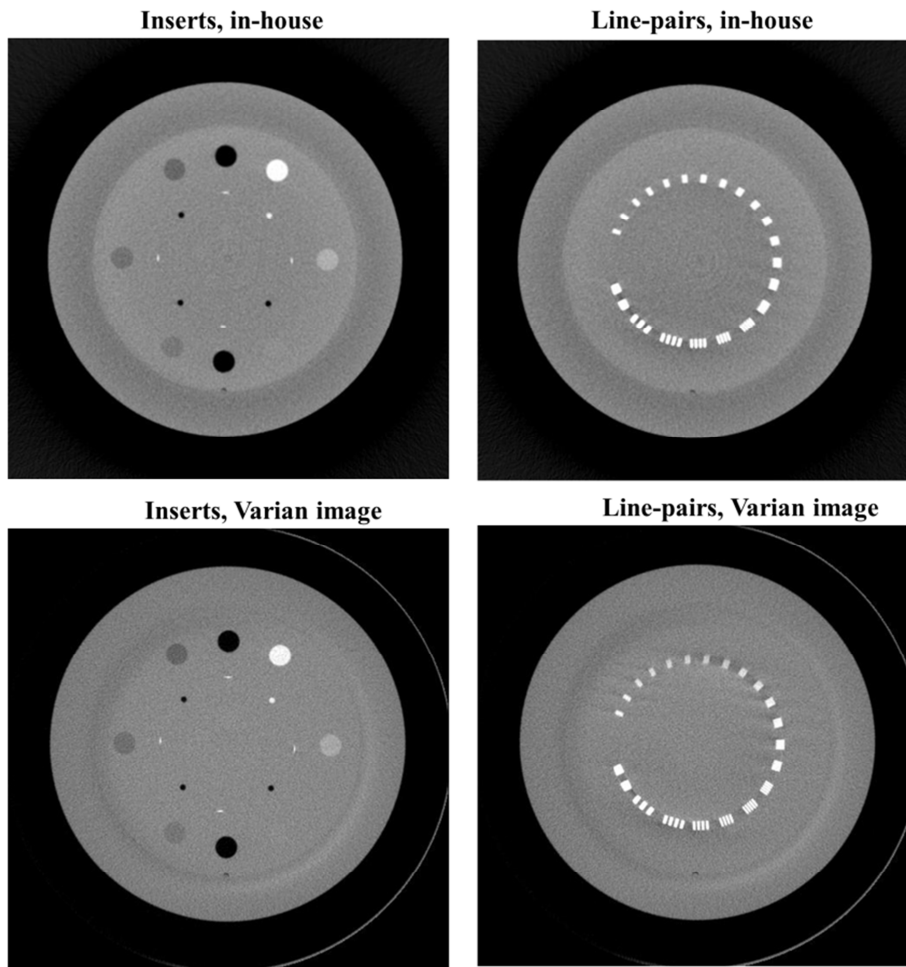


Figure 5.5 Reconstructed axial slices of Catphan in insert and line pair modules (top) and the same slices reconstructed by Varian software (bottom)

Each image is 250×250 mm, window width 1896, level 16. A crescent-shaped artefact is seen in both the Varian images due to mechanical instabilities. This artefact was completely controlled in in-house reconstructed slices as the normalisation procedure used air norm images taken at different gantry angles. Some dark smears are visible in both line-pair images.

5.3.4 Summary of 3D Image Reconstruction Procedure

3D images were reconstructed using the MATLAB script `CT_recon.m`, which incorporates the elements described above. Before reconstruction, the projection images were decompressed and stored as viv files.

The steps taken for reconstruction were:

1. Collect relevant scan parameters and header information (e.g. gantry angles, source and detector positions, and image resolution values) from each hnd projection files using the function `Readheader.m`.

2. Read the image from viv files using readviv.m
3. Load the air norm viv image to measure I_0 .
4. Define the reconstruction grid size to be within the detector limits; choose the thickness of the reconstructed volume and the number of slices to match the Varian image configuration.
5. Loop through the entire set of projection files one by one to:
 - Read the image from the viv file, take the logarithm and normalize it by taking log of (I/I_0) ;
 - Apply Parker weights and weighting factors for non-equal angles ;
 - Begin reconstruction by taking the cosine weighting of the projections and fourier filtering;
 - Backproject weighted projections onto the 3D grid of reconstruction points using the C++ MEX function getUV.cpp;
 - Obtain the reconstructed images (HU) of Catphan.
6. Save HU images as a DICOM file by using the function mat2dcm.m.
7. Convert the HU image to a density map using the calibration graph.

Regarding the processing time, the slowest part of the reconstruction process is generally the filtered back projection step. The time taken by the function CT_recon.m is proportional to the number of projection files in the scan, and also depends on the number of reconstruction grid points. On a 3.4 GHz Intel® Core™ i7-2600 processor, CT_recon.m took 9-10 seconds per projection, giving a total reconstruction time of almost an hour. However, use of MEX files reduced the processing time by a factor of 30.

5.4 Discussion of Image Reconstruction

All commercial CBCT scanners (including OBI) have implemented several correction processes to improve the image quality during reconstruction. The details of the Varian reconstruction software are not all available. Those corrections have not been performed in this study, as this will increase both the development time and the complexity. The Varian iX-CBCT reconstruction software includes a ring artefact suppression algorithm to reduce rings (as discussed in section 2.5.1) and also provides default beam hardening correction values for different CBCT modes. Thus in Figure 5.5, some concentric rings which are visible in the centre of the in-house reconstructed images are not seen in the Varian

images. However, the Varian full-fan scans in Figure 5.5 show a crescent-shaped artefact around the boundary between the inner and outer parts of the phantom. This artefact was not seen in images reconstructed for this project as the normalisation procedure was done using air norm images taken at different gantry angles.

One other visible difference in the two full-fan scans is that the Varian images show less contrast between the inner part of the phantom (15 cm diameter) and the outer ring (2.5 cm thick). In the Varian images, the difference in CT number between inner and outer parts is estimated to be about 65 HU whereas in the in-house images the difference is 115 HU. Nominal HU values are not available for these bulk plastic regions and so it is not clear which images are more accurate. However, the measured HU values for the sensitometry inserts were within the tolerance limits of ± 40 HU as specified by the Varian OBI for CT number accuracy (see Table 5.2).

The spatial resolution in the images was investigated using the line-pair module of the Catphan. To evaluate the spatial resolution, the Modulation Transfer Function (MTF) was measured based on the change of density across each line pair pattern using Droege's method (Droege & Morin 1982) as in equation 4.4.

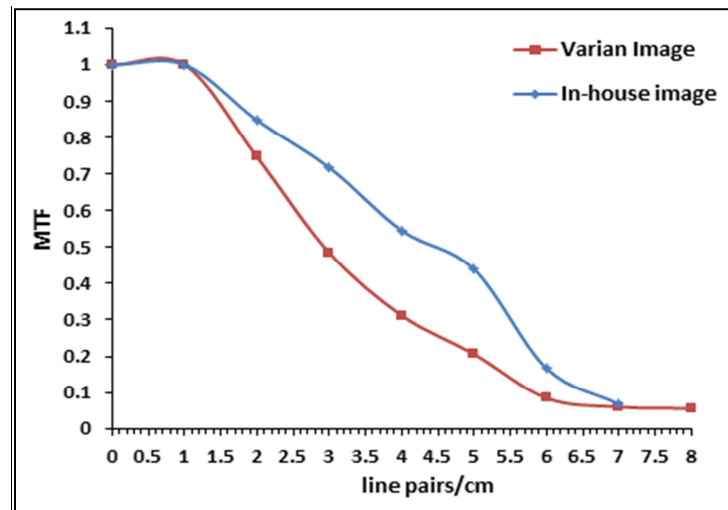


Figure 5.6 MTF calculated using Droege's method for Varian and in-house reconstructed images

The resolution obtainable for a given system is estimated by 50% and 10% MTF i.e., the frequency at which the contrast has dropped to 50% and 10% of the maximum value obtained at 0 line pair /mm respectively. In Varian images, at 50% MTF, the number of

line pairs measured is 3 lp/cm and at 10% MTF, the maximum number of line pairs seen is 5.9 lp/cm. Using in-house reconstructed images, at 50% MTF, the number of line pairs measured is 4.6 lp/cm and at 10% MTF is 6.7 lp/cm (Figure 5.6). The difference in resolution in spite of the same grid spacing may be due to the dark smears across the line pairs. This artefact affects the HU values and hence the density modulation across the line pair.

5.5 Conclusion

The in-house cone-beam reconstruction algorithm written in Matlab was developed for generating 3D reconstructions from x-ray data acquired from cone-beam scanning geometries. It is based on the FDK algorithm for 3D CBCT reconstruction. The implementation of this algorithm was intended to provide a platform for developing correction methods to account for artefacts seen in CBCT images and also to conduct image quality studies using several reconstruction filters and interpolation techniques. The speed of image reconstruction has been significantly increased by a factor of 30, so that the reconstruction process could be suitable for clinical practice.

With this algorithm, the crescent artefact seen on Varian images has been removed. The ring-like structure seen outside the Varian image is not visible in the in-house developed image. Using the default Ram-Lak filter, the contrast of the Catphan image is comparable to that of Varian's image. The resolution of 6.7 lp/cm at 10% MTF in the in-house image is found to be 13% better than that from Varian's image (5.9 lp/cm). The HU values measured for the insert materials of Catphan were within the tolerance limits. This shows that the cone- beam HU calibration curve is reliable and hence the CBCT datasets can be analysed for radiotherapy treatment planning.

Chapter 6

Analysis of Cone-beam Rando Images Reconstructed using In-house Software

6.1 Introduction

The in-house developed reconstruction algorithm described in Chapter 5 has been used to reconstruct several CBCT scans on the Varian iX unit at the Royal Adelaide Hospital. This chapter presents a representative sample of the resulting images. 3D CBCT scans of the male Rando phantom were taken during the development of the image reconstruction software to check that the quality of its images was comparable to that of Varian CBCT images.

6.2 Image Reconstruction

6.2.1 Rando Phantom

The Rando® Phantom (The Phantom Laboratory, NY, USA), is designed for use in a variety of radiation therapy applications including final quality verification of therapy dose delivery and comparison of delivered dose profiles for different treatment plans. The Rando phantom is available in male and female models. Both phantoms are constructed with a natural human skeleton which is cast inside two tissue simulating materials, the Rando® soft tissue material and the Rando® lung material. The lungs are moulded to fit the contours of the natural rib cage. The air spaces of the head, neck and stem bronchi are duplicated. The Rando materials are designed to have the same absorption as human tissue at normal radiotherapy exposure levels.

In this study, a Rando male phantom has been used to verify the image quality as well as the dose distribution. The Rando male model represents a 100 cm tall and 73.5 kg male which does not have arms or legs (Figure 6.1). The Rando phantom consists of several sections that have numbers corresponding to their positions located on the front upper side of the torso and left side of the head.

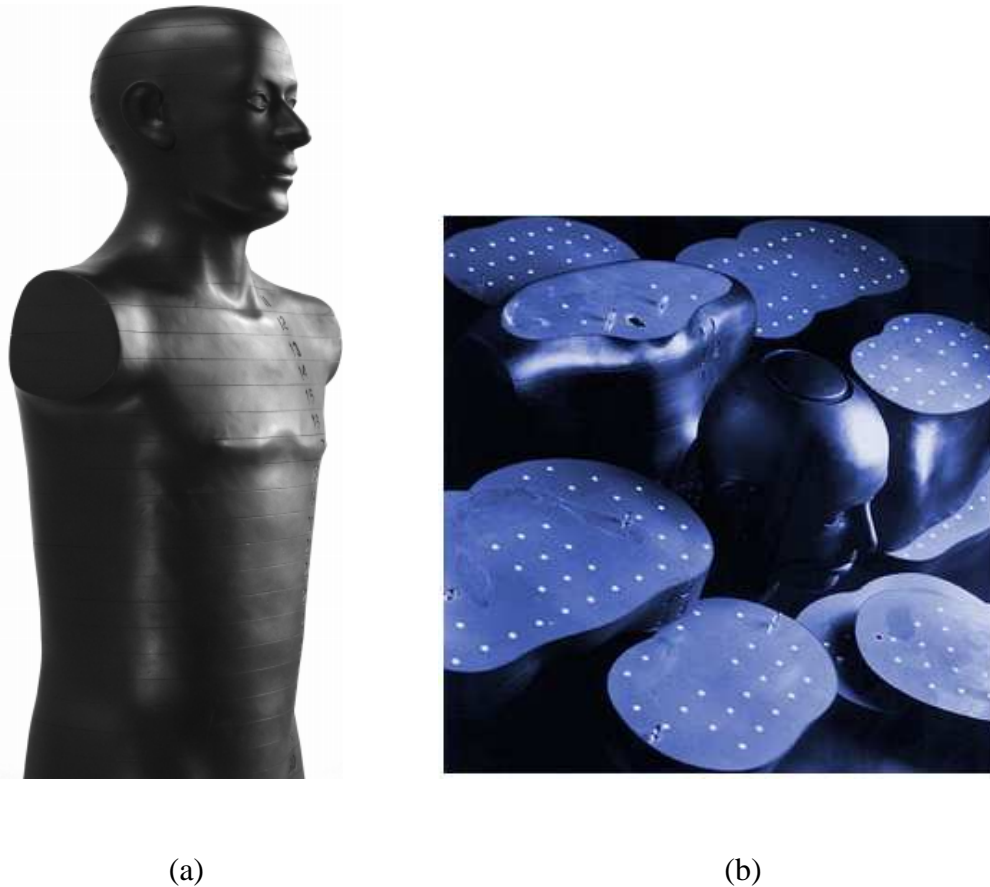


Figure 6.1 (a) Rando male phantom and (b) its sections

6.2.2 Reconstructed Rando Images

The Rando phantom was set up on the couch on the iX unit. The gantry was set up at 0° ; the linac head was above the phantom and the kV source was to the left with the full-fan bowtie filter attached to x-ray source. Three-dimensional CBCT scans of the Rando phantom were acquired to reconstruct the images using in-house developed software.

Table 6.1 summarises the scan and reconstruction parameters. The reconstruction grid spacing was chosen to be the same as that of Varian images. With a head first supine patient, the grid x direction is right-left, y is anterior-posterior and z is inferior-superior. The Varian reconstruction software applies ring suppression by default whereas this project's software has none.

Figure 6.2 shows representative examples of Rando full-fan scans acquired on a Varian iX unit. It shows axial slices of the Rando phantom reconstructed with the in-house software developed for this project and with the Varian CBCT reconstructor.

Table 6.1 CBCT scan and reconstruction parameters

Scan Parameters	iX full-fan
CBCT mode	Standard-Dose Head (100kVp, 20mA)
Bow-tie filter	Full bow-tie
Number of projections	360
Varian reconstruction parameters	
Reconstruction filter	Sharp
Ring Suppression	medium
Grid spacing in <i>x</i> and <i>y</i>	0.49 mm
Grid spacing in <i>z</i>	1 mm
In-house reconstruction parameters	
Parker weights	yes
Non-equal cone angle weights	yes
Adaptive filter	yes

Overall, the image quality is comparable to Varian reconstructions and good enough to distinguish the features in the Rando phantom. The crescent-shaped artefact which is visible in Varian images is not seen in reconstructed images. The reconstructed images were exported to the TPS for calculating the dose distribution for a given radiotherapy plan.

6.3 Radiotherapy Treatment Planning

6.3.1 Treatment Technique

One of the most important recent advances in radiotherapy has been the development of IMRT. It is an advanced high precision radiation delivery method during which highly conformal and non-uniform dose distributions are produced by modulating the intensity of the radiation beam within the radiation field. A multi-leaf collimator (MLC), which is a computer-controlled device to tightly conform the radiation field shape using high density Tungsten alloy leaves, helps in producing the intensity modulated beams. Step-and-shoot or segmented IMRT is a form of IMRT where the radiation field is divided into several sub-fields that are sequentially irradiated using planned amounts of radiation.

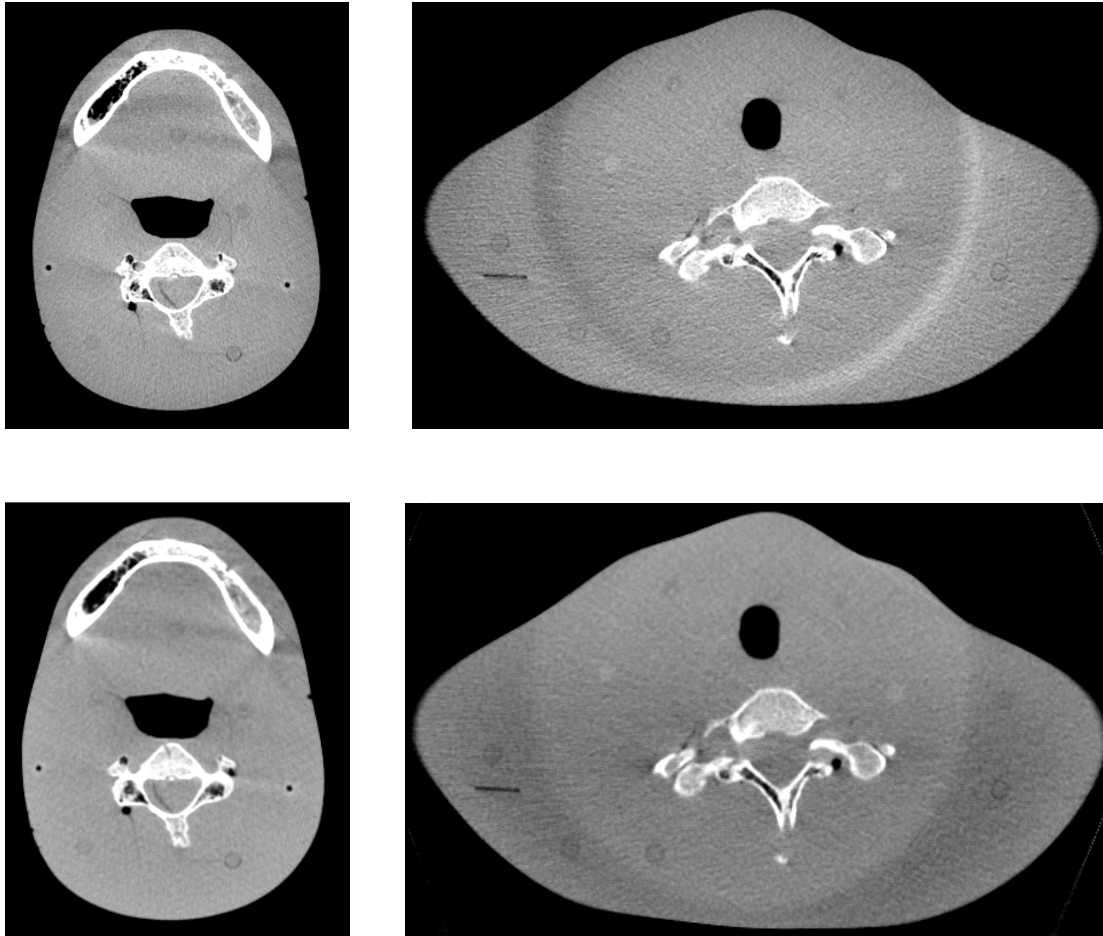


Figure 6.2 Reconstructed axial slices from head and neck regions of Rando using Varian software (top) and in-house (bottom)

After each sub-field irradiation, the MLC is moved to the position for the next irradiation. This step-and-shoot mode of IMRT was used in this study as it is quite straightforward to understand clinically and individual radiation fluence intensity patterns can be verified easily with 2D detector systems (Allen, Marcu & Bezak 2012).

Figure 6.3 shows the schematic diagram of the IMRT inverse planning process using the Pinnacle³ TPS (ADAC Laboratories, Milpitas, CA, USA) version 9.2m, used in this study. At first, the target volume and other relevant critical structures are carefully delineated on CT images in order to calculate and optimize the treatment plan. Before optimizing the plan, objectives and constraints are defined to achieve a desired treatment goal. During the optimization process the system determines the particular beam weights and radiation fluence distribution patterns to fulfill the clinical objectives. The results of the optimization process are in the form of radiation fluence that if delivered would best satisfy the clinical criteria/objectives.

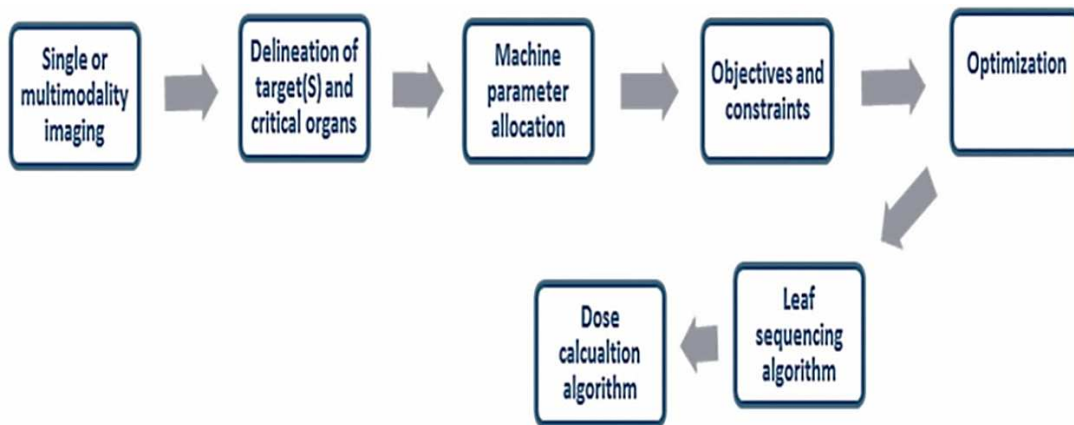


Figure 6.3 Schematic diagram of IMRT treatment planning process

6.3.2 Treatment Optimisation Parameters

Direct Machine Parameter Optimization (DMPO) is an approach to IMRT optimization in which, for a given linac beam model, beamlets can be calculated for radiation fluence from the actual leaf positions and the weights of each segment (Hårdemark et al. 2004). The fluence is then converted into a multilevel approximation distribution using *K-means Clustering method* (Wu, Y et al. 2001) enabling faster treatment delivery. Finally from the clustered intensity levels, MLC segments are formed to accurately deliver the dose to the target volume.

Before the dose calculations, the IMRT optimization parameters were set for DMPO and saved for each trial. Figure 6.4 shows the screen shot of IMRT parameters set for the DMPO optimisation in Pinnacle TPS. Once all the parameters are set, the plan is optimized.

6.3.3 Treatment Planning Parameters

As the purpose of this study was to compare CBCT-based dose planning with PCT-based planning (reference plan), a PCT scan of Rando was acquired and the images were exported to the Pinnacle TPS. An IMRT plan which includes seven 6-MV photon beams at gantry angles of 150°, 100°, 55°, 0°, 305°, 260° and 210° was performed on the PCT image sets. The PTV and the critical organs, namely Larynx, Parotid left, Parotid right and spine were delineated carefully. An isocentre labeled as 'iso' was defined at the centre of the PTV. A radiation absorbed dose of 2 Gy per fraction was prescribed to 100% of point dose at the isocentre for 30 fractions. The dose grid geometry was set to a resolution of 0.2 cm.

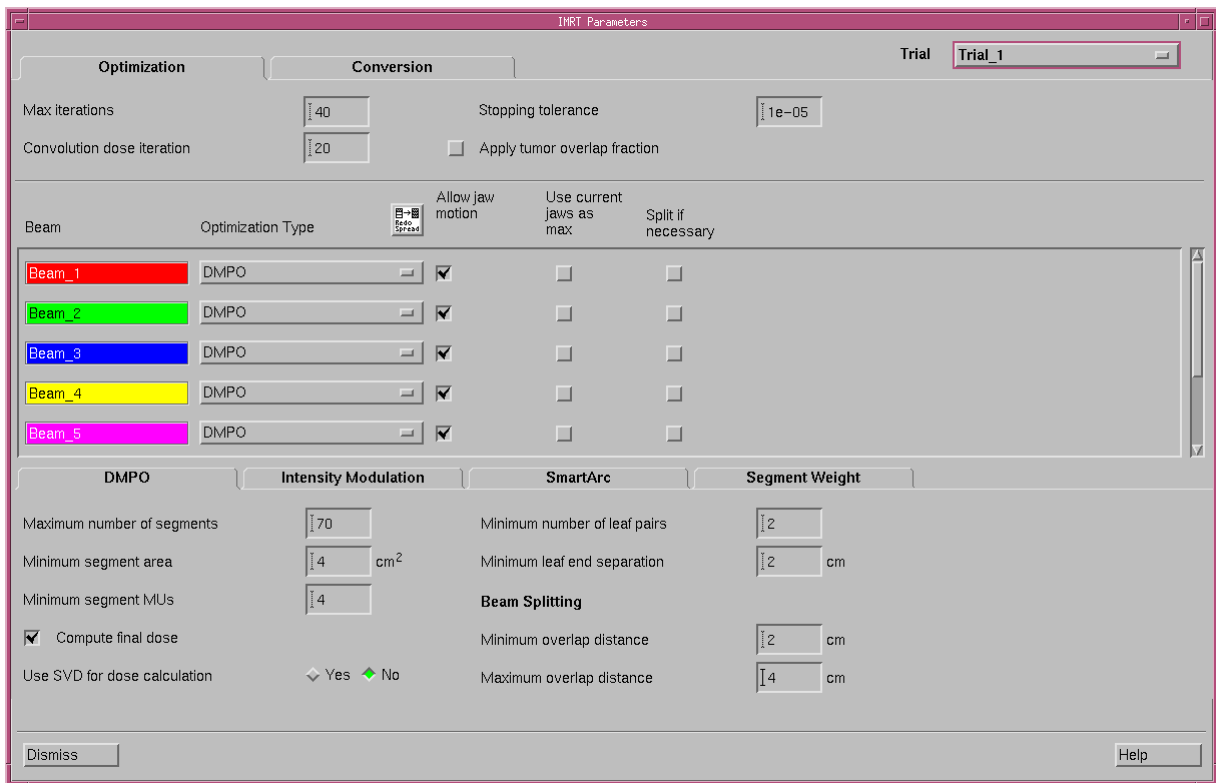


Figure 6.4 IMRT parameters window from Pinnacle TPS

The reconstructed and Varian CBCT Rando images were also exported to the Pinnacle TPS and a verification plan was created on CBCT datasets keeping the beam parameters, Monitor Unit² (MU) values and fluence maps of the reference plan. Table 6.2 gives the details of the planning parameters used in this study.

6.3.4 Dose Calculation Algorithm

Convolution/superposition algorithms are commonly applied in most modern radiotherapy treatment planning systems to calculate the dose distribution. This study used the Adaptive Convolution Algorithm (ACA), a model-based algorithm that calculates dose based on beam modifiers, tissue heterogeneities and surface of the patient. In this method, the speed of the computation is increased by adaptively varying the resolution of the dose computation grid depending on the curvature of Total Energy Released per unit Mass (TERMA) and dose distribution.

² Monitor Unit is the measure of radiation beam output by the ion chambers

Table 6.2 IMRT plan summary for Rando PCT and CBCT scans

Beam setup	Beam 1	Beam 2	Beam 3	Beam 4	Beam 5	Beam 6	Beam 7
Energy Modality SAD (cm) Isocentre	6MV Photons 100 iso	6MV Photons 100 Iso	6MV Photons 100 iso	6MV Photons 100 iso	6MV Photons 100 iso	6MV Photons 100 iso	6MV Photons 100 iso
Beam geometry							
Couch angle Gantry angle Collimator angle SSD (cm)	0.0 150.0 5.0 86.46	0.0 100.0 3.0 96.10	0.0 55.0 1.0 95.75	0.0 0.0 0.0 90.81	0.0 305.0 358.0 91.92	0.0 260.0 356.0 92.70	0.0 210.0 354.0 86.45
Collimators (cm)							
X1/X2 (lower jaws) Y1/Y2 (upper jaws)	3.50/6.00 4.50/15.50	4.50/8.45 4.50/14.50	6.50/6.00 4.50/13.50	6.00/3.50 4.50/13.50	8.00/4.00 4.50/14.50	7.50/5.50 5.00/15.5	5.0/6.5 5.0/15.5
Dose							
Dose Engine Density correction Reference point Dose rate (MU/min) Number of fractions MU/fraction	ACA Heterogeneous Isocentre 300 30 96	ACA Heterogeneous Isocentre 300 30 37	ACA Heterogeneous Isocentre 300 30 77	ACA Heterogeneous Isocentre 300 30 86	ACA Heterogeneous Isocentre 300 30 97	ACA Heterogeneous Isocentre 300 30 120	ACA Hetero Isocentre 300 30 86

The basic steps involved in ACA (McNutt 2007) are given below:

- The dose in a coarse 3D grid is computed and the curvature in the TERMA distribution is assessed.
- In regions of high curvature, the dose is computed at intermediate points to increase the resolution. The system adaptively increases the resolution until an acceptable resolution is used.
- In regions of low curvature, the dose is interpolated from the coarse dose grid.

In order to have an efficient optimization during IMRT planning, the dose computation must be fast. Thus ACA was used in this study to provide rapid dose computation on PCT and CBCT data sets without sacrificing its accuracy. Once the desired treatment goal was achieved, the plan is locked and ready for evaluation.

6.3.5 Treatment Plan Evaluation

A Dose Volume Histogram (DVH) is a tool for determining dose distribution within the defined volume of interest across multiple trials. DVHs provide plots of normalized or absolute dose versus normalized or absolute volume. However, the DVHs do not provide any spatial information about the dose distribution.

Another method for evaluating the plan is to generate the dose distribution for any beam at a given depth in a current image set. This study used planar dose distribution evaluation with the planar dose being computed in cGy/MU for the selected beam. The planar dose map was then exported to MapCHECK™ software for comparison against other measurements.

MapCHECK™ is a 2D system of 445 diode detectors intended for the measurements of dose distributions resulting from a treatment plan. The MapCHECK™ has associated software with which the dose distributions from two plans can be compared. MapCHECK™ uses Gamma analysis to compare the dose distributions between the planned and the measured dose map. Three parameters, threshold, percent difference and distance (mm) are defined to setup pass or fail criteria for the measurement point (detector position). Generally, the threshold is set at 10, which means that all measurement points that are below the 10% contour are excluded in Gamma analysis. By this we could exclude

detectors that are outside the region of interest. Percent difference and distance (mm) values are set by default as 3% and 3mm respectively. Percent difference is the allowed percentage dose difference between any measured point and the corresponding plan point normalized to a common point. Distance (mm) indicates the radius around the measured point such that if there exist at least one planned point within the radius of circle, then the measurement point passes.

In this study, the Gamma analysis technique was used to quantitatively evaluate the dose distributions by comparing them. This technique, developed by Low et al. (1998), uses both percent difference and distance criteria and calculates a unit-less 'Gamma index' (γ) value for each measured point. If the gamma index value is less than or equal to 1, then the measured point is said to pass the criteria. If the gamma index is greater than one, then the point fails. This analysis gives the number of passed, failed and % passed based on gamma index value. On the comparison dose map (gamma map), the failed points that record a higher value are shown in red and those that record a lower value are shown in blue. On the profile panel, profiles can be displayed along a line parallel to the X, Y and diagonal axes through any detector location.

6.4 Planning Results

The IMRT dose distributions were calculated based on PCT, Varian CBCT and in-house reconstructed CBCT images in the head & neck region of the Rando phantom. The dose distributions generated on these three image sets are shown in Figures 6.5, 6.6 and 6.7. The point dose calculated at 'iso' (indicated by red circle with a cross) on Varian and in-house reconstructed CBCT images were within 1% agreement. This shows that HU density calibration and HU linearity between both set of images were in good agreement.

Further, the point dose was in agreement with the PCT-based point dose. The 2D planar dose map was then extracted from all three image sets and was exported to MapCHECK™. Using Gamma analysis the dose distributions were compared between PCT and CBCT images and the profiles were generated

The planar dose calculated using the PCT image agreed with in-house reconstructed CBCT-based dose distributions and the percentage of dose points passed as per Gamma

analysis was found to be 99.8%. This is exactly the same agreement which was obtained comparing PCT and Varian planar dose maps.

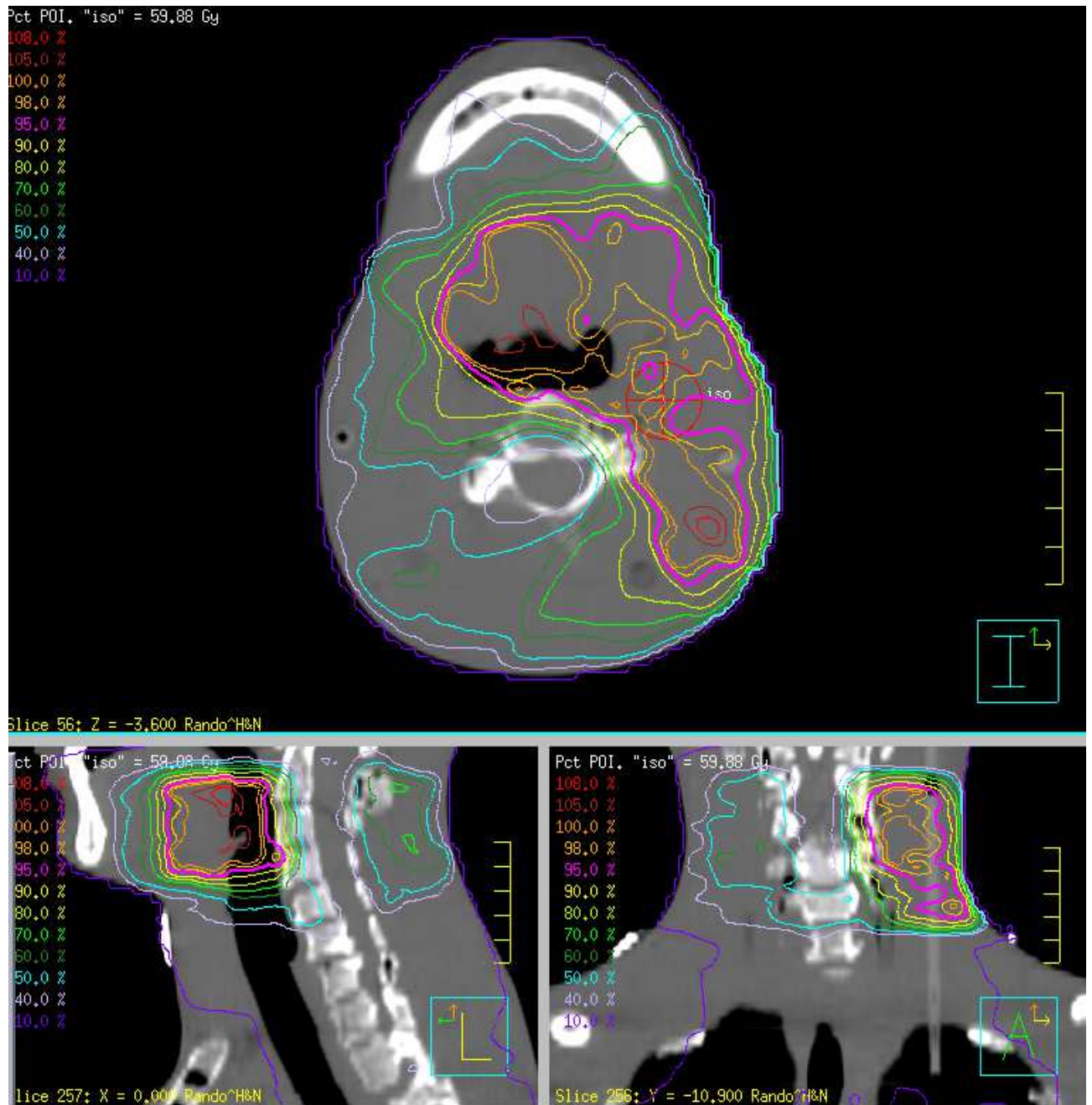


Figure 6.5 IMRT dose distributions computed on planning CT images in axial, sagittal and coronal slices

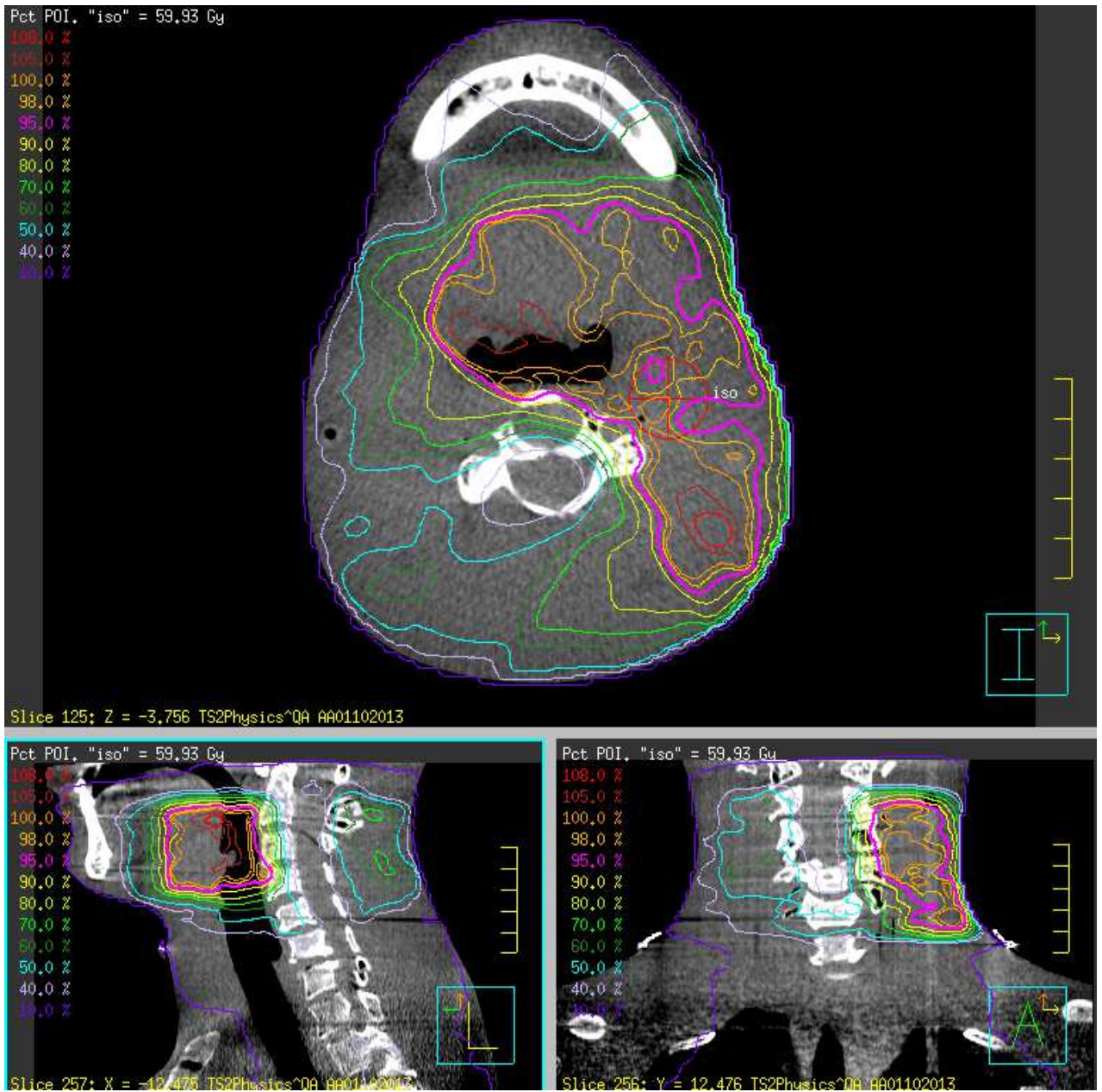
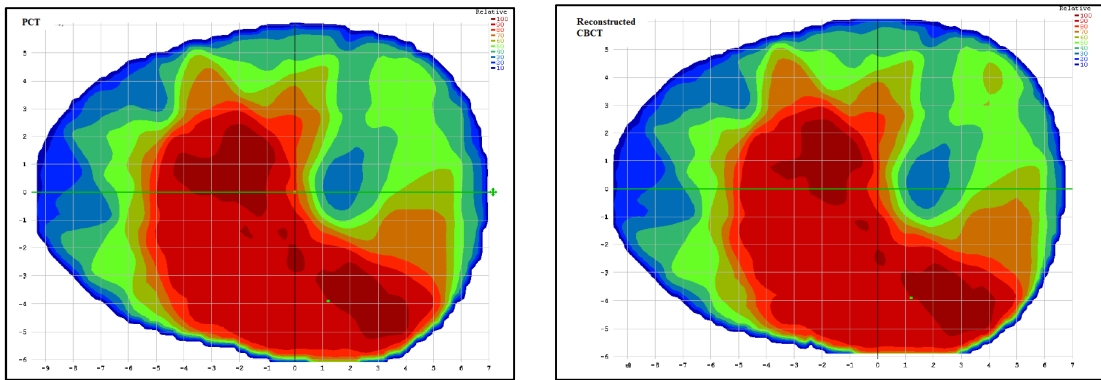


Figure 6.6 IMRT dose distributions computed on Varian CBCT images in axial, sagittal and coronal slices

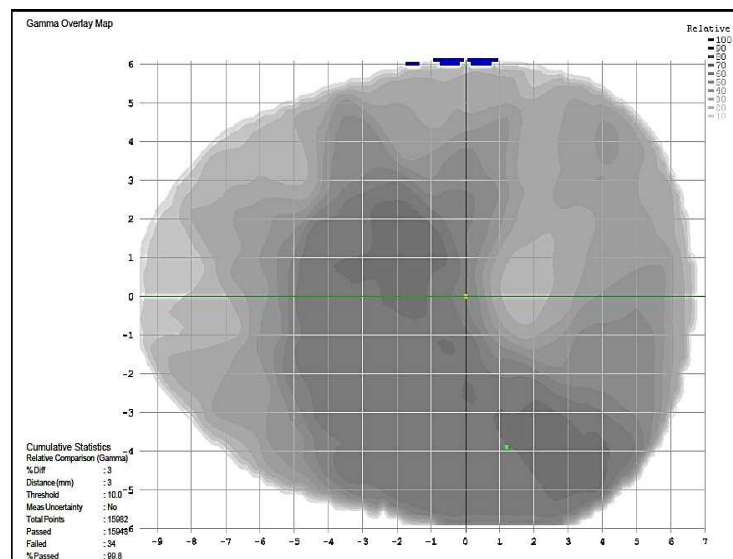


Figure 6.7 IMRT dose distributions computed on in-house reconstructed CBCT images in axial, sagittal and coronal slices

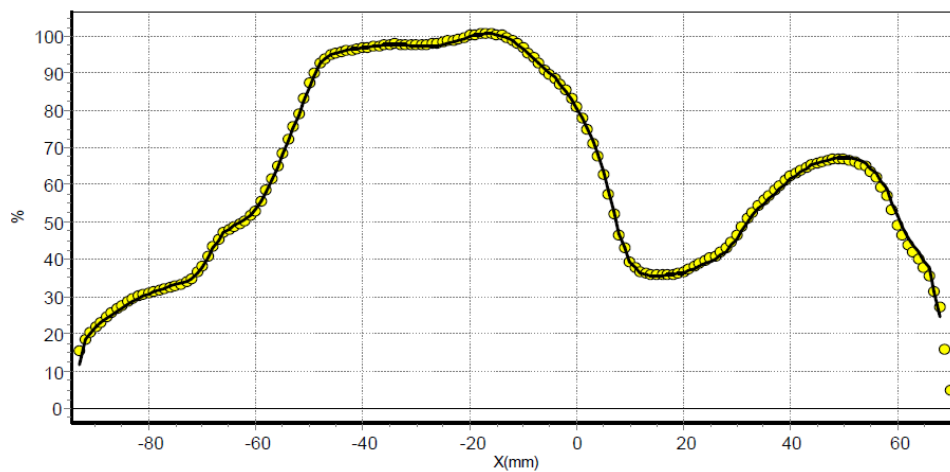


(a)

(b)



(c)



(d)

Figure 6.8 The planar dose maps from (a) PCT, (b) in-house reconstructed CBCT are compared to produce (c) Gamma dose map showing failed points in blue colour and (d) profiles generated across x-axis of the planar dose maps (black line- PCT; yellow circles- CBCT)

Figure 6.8a and 6.8b shows the planar dose maps extracted from PCT and reconstructed Rando image respectively. The Gamma analysis map in Figure 6.8c shows the difference in dose points between the two sets of planar images with failed dose points in blue colour (small blue area at the top of the map). The profiles along the x-axis of the two sets were compared and showed a good agreement (Figure 6.8d).

6.5 Conclusion

Cone-beam images of a Rando male phantom were reconstructed using the in-house developed algorithm. The images reconstructed were of good quality and better than Varian's image quality. All the Rando features which are visible in the Varian image are also visible in the reconstructed image. In addition, the crescent-shaped artefact which is seen in the Varian image is not seen in the reconstructed image (see Figure 6.2). This improves the HU uniformity and hence the image quality. This shows the potential of the in-house reconstruction algorithm as a research tool for implementing the FDK algorithm.

In order to investigate the effectiveness of reconstructed CBCT datasets for dose calculations, the dose distributions for PCT (reference image) and reconstructed CBCT Rando images were calculated using ACA. To evaluate the plan, the planar dose distributions from PCT and CBCT reconstructed images were extracted and exported to MapCHECK™ software to compare the dose distributions and to generate a typical profile. The dose distributions obtained from reconstructed images were in good agreement with that of the reference PCT image and found to have a 99.8% pass rate using Gamma analysis. This indicates the potential of reconstructed CBCT images using the in-house algorithm in spite of the fact that several pre-processing steps performed on Varian image have not been included. A hundred percent agreement may be possible by implementing the calibration procedures which Varian CBCT has performed.

Chapter 7

Iterative Reconstruction for Cone-beam

7.1 Iterative Reconstruction-Overview

Cone-beam computed tomography images can be reconstructed either analytically or iteratively. While an analytical method (such as FDK) results in fast reconstruction for CBCT images, its accuracy is limited by the approximations implicit in the line-integral model on which the reconstruction formulae are based. Insufficient cone-beam projections with truncated data and non-uniform volume coverage have also highly degraded the results of this algorithm. These cause artefacts in addition to the noise enhancement that is inherent in the reconstruction process.

An alternative approach to analytical methods is the use of iterative reconstruction techniques which can model complex photon production, transport and detection and therefore better accommodate assumptions regarding the acquired projections. In the CBCT context, iterative methods have the ability to model important physical factors including focal spot and detector geometry, photon statistics, x-ray beam spectrum and scattering, to yield lower image noise and higher spatial resolution compared with analytical methods (Thibault et al. 2007). As a result, they reduce streak artefacts that are common in analytical methods and are better able to handle missing (truncated) data. Thus recently iterative reconstruction algorithms have been investigated for CBCT image quality and have been shown to have better performance than FDK-based algorithms (Maass et al. 2010; Qiu et al. 2010; Wang, Li & Xing 2009).

An iterative image reconstruction algorithm based on penalized-weighted least squares (Wang, Li & Xing 2009) was developed to preserve edges in CBCT reconstructed images and produced a clinically acceptable image quality with as low as possible tube current. Jia et al. (2011) have developed a GPU-based iterative CBCT reconstruction using tight frame regularization to reconstruct high quality images from undersampled and noisy projection data. A recent clinical study on iterative reconstruction demonstrated a potential CT dose reduction of up to 65% (Hara et al. 2009) compared with FBP-based reconstruction

algorithms. Hence an iterative method is of high interest as it can potentially deliver reconstructions with improved uniformity and reduced artefacts from truncated acquisitions with tube current as low as 20mA.

This study used a Maximum Likelihood (ML) solution assuming Poisson noise distribution in tomographic reconstruction of cone-beam images of the Catphan phantom. The Expectation Maximisation (EM) algorithm was used to solve ML problems by computing the mean of the complete dataset, given the observed data and the current estimate of the image, and maximizing the probability of the complete dataset over the image space.

7.2 Maximum-Likelihood Algorithm

Expectation-Maximisation is a commonly used iterative reconstruction algorithm. It works by computing the projections from an initial estimate of a uniform grey image, generating a correction matrix relative to the observed projections and then by backprojection using it to update the current image estimate. As the number of iterations is increased, the image noise and computation time increase. Hence a decision has to be made to stop the algorithm using the number of iterations which influences the image quality. Equation 7.1 relates the measured projection pixels p_i to voxel f_j in tomographic space as

$$p_i = \sum_j a_{ij} f_j \quad \dots (7.1)$$

where a_{ij} is the system matrix or transition matrix which holds the result of extensive preliminary computations to yield the probability of detecting a transmitted photon originating from location j , at any particular location, i , on the detector. Subscripts i and j are a simplification of the multiple subscripts required to label each 2D projection pixel and acquisition angle, and each voxel in 3D tomographic space. The system matrix models the detection process and can be made more realistic by adding corrections for scatter and geometric detector response. This ability to model the system provides considerable flexibility in the type of data that can be reconstructed.

The basic Poisson probability distribution provides the probability of measuring a particular projection count, c , given an expected measurement, r as

$$Prob(c|r) = \frac{e^{-r}r^c}{c!} \quad \dots (7.2)$$

Using this probability model from equation 7.2, the probability of acquiring the projection data that was measured (p), given an estimated projection, f can be represented by the product of probabilities of individual projection pixels. This conditional probability, referred to as the likelihood function, L is given by the independent Poisson distribution as,

$$L(p|f) = \prod_i \exp(-\sum_j a_{ij}f_j) (\sum_j a_{ij}f_j)^{p_i} (p_i!)^{-1} \quad \dots (7.3)$$

Maximising the probability of $p|f$ gives the most likely distribution of intensity to provide reconstructed images that represents the original object. Thus the current estimate of reconstruction is updated to maximise the likelihood by multiplying the previous estimate by the back projection of the ratio of measured over estimated projections. The Maximum-Likelihood equation gives the new estimate (f_j^{new}) in terms of the old estimates (f_j^{old}) of the image, f_j as:

$$f_j^{new} = f_j^{old} \times \frac{1}{\sum_l a_{lj}} \times \sum_i a_{ij} \frac{p_i}{\sum_k a_{ik}f_k^{old}} \quad \dots (7.4)$$

The Maximum-Likelihood (ML) method was developed by Rockmore and Macovski (1976) to explicitly include a Poisson model. However, work on the Expectation Maximisation (EM) algorithm by Shepp and Vardi (1982) and Lange and Carson (1984) has resulted in widespread use of these ML approaches in clinical systems as it unifies various previous statistical approaches. Successive estimates of reconstruction f_j are adjusted according to the projection space correction matrix, which is converted to a tomographic correction using a_{ij} in an inverted equation 7.1 which sums over i instead of j (the right-most summation in equation 7.4). The new estimated projections are then calculated from equation 7.1 by forward projection, new corrections computed and applied in tomographic space, etc.

The EM algorithm has several properties that include guaranteed non-negative values due to the use of multiplicative updates and convergence at each of the iteration. However it also converges very slowly. A definite limitation of MLEM is the reconstruction time.

Each iteration involves a forward and backprojection step and takes approximately the same time as an entire FBP reconstruction. Hence computation time for iterative reconstruction algorithms is typically orders of magnitude longer than for FBP. Hence any improvement with iterative algorithms is obtained at the cost of increased calculation time. If high resolution is needed, then even more iterations may be necessary. Thus EM algorithms for cone-beam geometries are impractical with current computer hardware.

In order to accelerate the MLEM algorithm, many studies have investigated alternatives to the EM algorithm that converge faster. In the Ordered Subsets Expectation Maximisation (OSEM) method (Hudson & Larkin 1994), the data are divided into a number of subsets, and the EM algorithm applied sequentially to each of these data sets in turn. This produces remarkable improvements in the initial convergence rate compared to EM. Manglos et al (1995) have used the OSEM algorithm on CBCT transmission data acquired on a Triad Gamma camera. The algorithm was found to provide high-quality, nearly artefact-free reconstructions of untruncated CBCT data within 2 to 4 iterations and of truncated data in 8 iterations. This study has adopted the OSEM algorithm for CBCT reconstruction in order to handle the truncated acquisition geometry. Unfortunately, the particular OSEM implementation used here cannot model key physical features of CBCT such as the source geometry and X-ray spectrum.

7.3 Implementation of the OSEM Iterative Reconstruction Algorithm

The OSEM implementation used here was written by Hudson & Larkin (1994) primarily to reconstruct emission tomography (SPECT and PET) projections, although it does contain limited options for reconstruction of transmission projections. It reconstructs both parallel-beam and fan-beam projections. The central plane of a cone-beam projection gives an approximation for fan-beam projection with a slight difference in scatter contribution and beam divergence compared to a fan-beam. In order to acquire approximate fan-beam projections from CBCT, the spatial resolution elements of the phantom had been carefully positioned to be imaged by the central plane. Thus fan-beam reconstructions of the central plane of cone-beam projections were used to evaluate the potential of iterative reconstruction in CBCT.

It was possible to utilise distance dependent resolution (DDR) modelling in OSEM, originally intended for gamma camera collimators in SPECT, because the distance dependence was linear for both SPECT collimators and the CBCT x-ray tube when approximated by a point source. In emission projections the signal approximates the line sum of the activity levels, while in the transmission projections used here the signal approximates the line sum of the attenuation coefficient. Therefore the amplitude of the voxel signal to be reconstructed was the attenuation coefficient and the distance dependent resolution was measured and entered as input to the program.

Photon attenuation and Compton scattering of emitted photons have been modelled in the SPECT implementation. A transmission-dependent method for scatter correction was developed by Meikle et al. (1994) to incorporate planar transmission measurements in the estimation of photo peak scatter. These transmission measurements were found to achieve sufficient accuracy when combined with iterative techniques. Since CBCT includes a large amount of scatter (refer section 2.5.1) that significantly limits the image quality, this transmission-based scatter model in OSEM designed for the correction of scatter from emission sources was tested on (transmission) cone-beam images. In practice, transmission factors are obtained by dividing a planar transmission by a blank scan (air scan). The number of scattered photons that reach the detector in proportion to total photons (scatter fraction) is then determined for each point in the projections based on those transmission factors. This can then model the scatter in the reconstruction and thereby generate scatter-free tomographic images. However, because the scatter and detector geometries are so different for emission and transmission (Fig 7.4) this may be of limited value in the application here of emission scatter modelling to the CBCT transmission case.

7.4 Experimental Methods

7.4.1 Image Acquisition and Pre-processing

CBCT data of Catphan®504 (The Phantom Laboratory, New York, USA) were acquired using Varian CBCT system (Varian Medical Systems, Palo Alto, CA) with standard head protocols. The Catphan (Figure 7.1) has four different sections, which include HU uniformity (CTP 486 in Fig 7.1), HU linearity (CTP404), high contrast (CTP528) and low contrast (CTP515) sections, for performing different image quality tests. The scans were acquired after positioning Catphan to yield projections of the section of interest at the

central plane. The projections were acquired using standard-dose head protocol (refer Table 3.1) over 200° in a total scan time of 33 seconds. The projection matrix has an array of 1024×768 of pixel size 0.0388 cm. The full-fan bow-tie filter was mounted on the CBCT source head to equalise the intensity across the detector and to improve image quality. Each set of projections acquired was pre-processed using Matlab by taking the logarithmic ratio of Catphan projections to air-scan projections (refer section 5.2.2). This converted the intensity projections to attenuation coefficient projections (as per equation 5.1), suitable for image reconstruction.

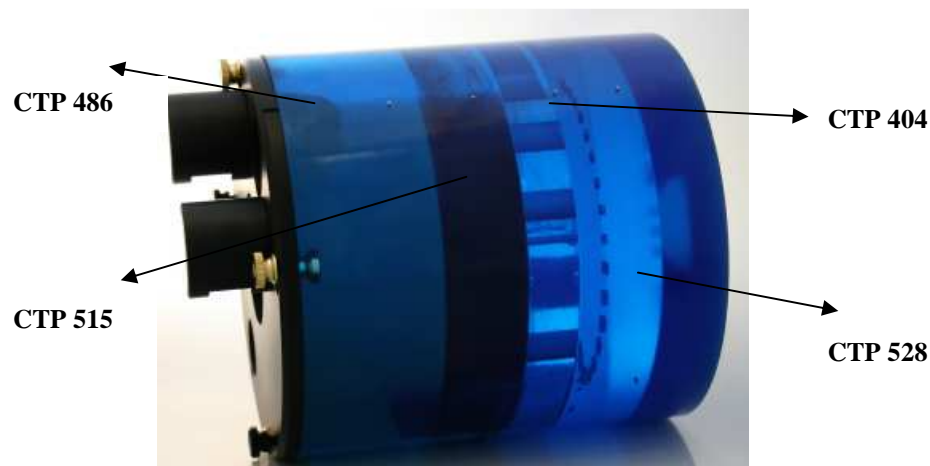


Figure 7.1 Catphan@504 phantom used for CBCT scans

7.4.2 Distance Dependent Resolution (DDR) Corrections

In order to accurately reconstruct the images, the distance dependence of the spatial resolution of the CBCT system for imaged objects must be included in the OSEM iterative image reconstruction model (Yokei, Shinohara & Onishi 2002). Spatial resolution was measured as the FWHM of a thin wire (about 1 mm diameter) in the projections for a range of wire to detector distances. Distance dependent resolution correction takes into account the geometric blurring which increases with distance from the detector. Modelling this effect during image reconstruction improves the final image quality at the expense of a large increase in computation time. For each scan, distance resolution was estimated by fitting a Gaussian distribution to the projection count profile for a line of pixels perpendicular to the direction of the line source using the Interactive Data Language (IDL) “GAUSSFIT” function. Figure 7.2 shows the cone-beam projections of a thin wire scanned at 500 mm from the detector.

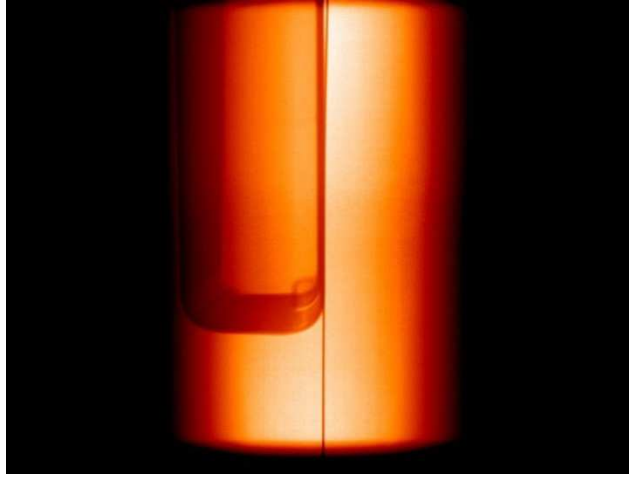


Figure 7.2 Cone-beam projection of a thin wire seen on IDL program

The FWHM of the line source with distance from the detector (d) was measured and results are listed in Table 7.1 and plotted in Figure 7.3. The slope of the linear regression line obtained is 0.0154 and the intercept is 0.7372, forming a linear equation describing the dependence of spatial resolution on distance. This is given as,

$$\text{FWHM} = 0.00154 \times d + 0.7372 \quad \dots (7.5)$$

The iterative reconstruction program requires input of this relationship in terms of σ (standard deviation) of the Gaussian that describes each point spread function. This is derived from FWHM via equation 7.6 as,

$$\text{FWHM} = 2\sqrt{2\ln 2} \sigma \quad \dots (7.6)$$

Thus the point spread function that describes the spread of the counts about the point is modelled by inputting σ as,

$$\sigma = \frac{\text{FWHM}}{2.3548} = \frac{0.00154 \times d + 0.7372}{2.3548} = (\text{CollScale}) \times d + (\text{CollConst}) \quad \dots (7.7)$$

where *CollScale* ($0.00154 \div 2.3548 = 0.00065$) denotes the slope and the *CollConst* ($0.7372 \div 2.3548 = 0.3130$) denotes the intercept of the line and are input as arguments in the OSEM program command line (section 7.5 below).

Table 7.1 FWHM measurements of a thin wire at various distances from the detector

Distance from detector (mm)	FWHM (mm)
300	1.19
350	1.29
400	1.36
450	1.45
500	1.49
550	1.54
600	1.65
650	1.75
700	1.83

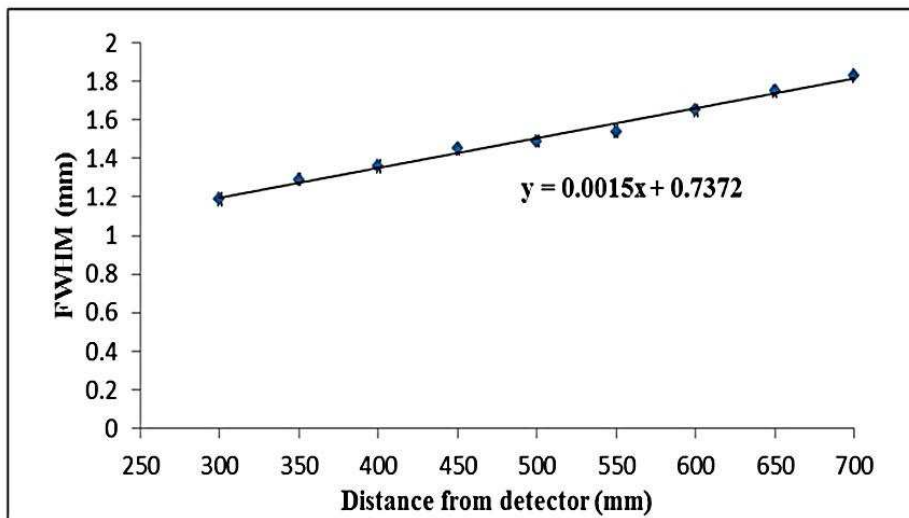


Figure 7.3 FWHM for the flat-panel detector as a function of distance between source and detector

7.4.3 Simple Transmission OSEM

The Macquarie OSEM software has limited option for transmission geometry. Figure 7.4 shows the difference between transmission-based and emission-based geometries. In the emission option on the right, the measured projections represent line integrals of the radioactivity distribution within the object, whereas, in transmission geometry at left, the measured projections represents the line integrals of attenuation coefficients along lines from the x-ray point source. This transmission option can only model a point source of X-rays and appears not to be able to model scatter in the object.

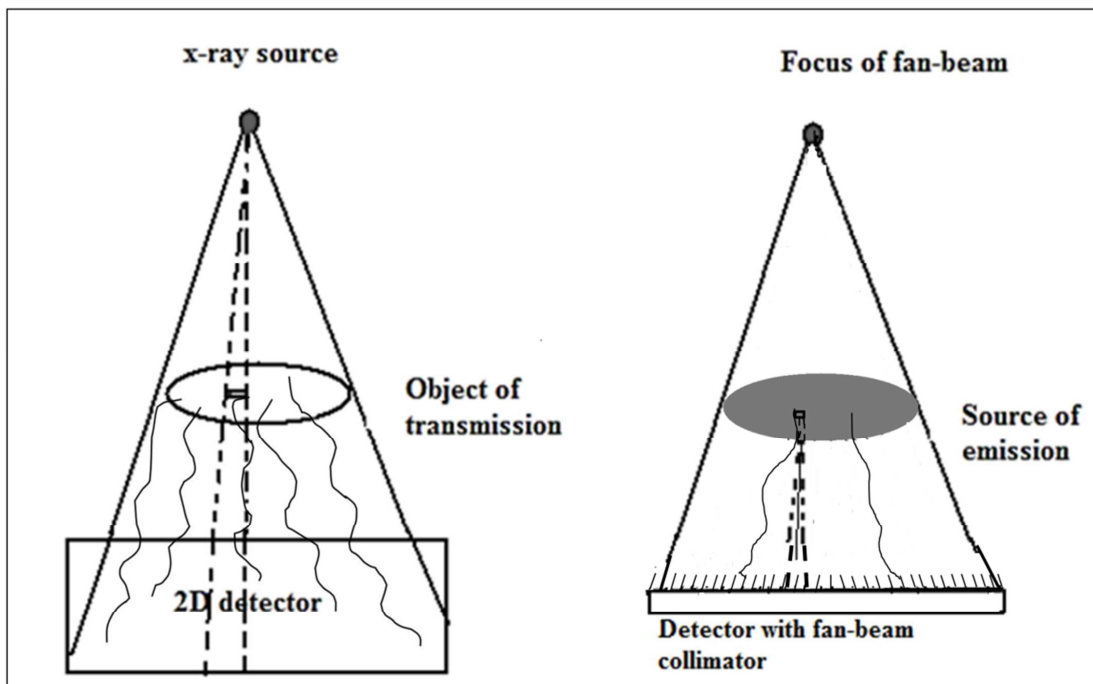


Figure 7.4 Transmission- and emission-based geometries

7.4.4 Centre of Rotation (COR) Offset

Another important parameter that must be specified is the 'centre of rotation'. Misalignment between beam isocentre and the central pixel of the detector influences image quality. Any offset must be corrected to avoid degradation of the reconstructed image. This is implemented by including the X and Y offsets in the header file of the projection dataset which is the input for iterative reconstruction. These values are used to translate the projections for all angles within the program before reconstruction. In order to measure this, a blade calibration plate (Figure 7.5a) was placed on the couch with its surface at 100 cm SSD, as shown in Figure 7.5b. The gantry angle was set to 90° and each collimator blade was opened to 3.5 cm and the image was acquired. The distance between the centre of the blade calibration plate and the graticule was measured to be 0.8 mm. This value was fed into the interfile header information as Centre of Rotation offset.

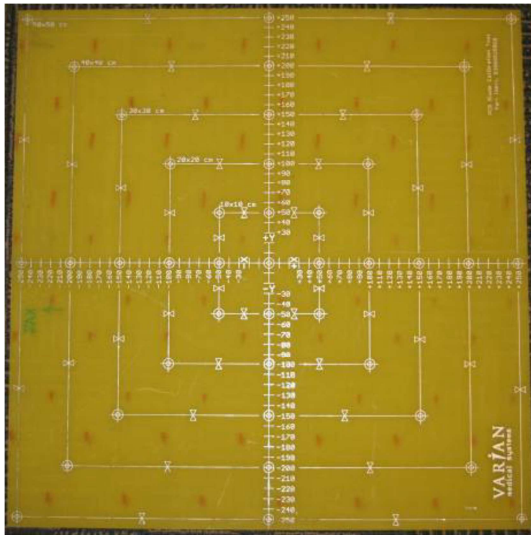


Figure 7.5 (a) Blade calibration plate and (b) setup

7.5 Practical Applications of OSEM and Results

The projections of Catphan were pre-processed using Matlab and concatenated into single file for input to the OSEM reconstruction program. A header file containing the details of acquisition, projection and detector geometry, pixel resolution and centre of rotation offset was created and an example is shown in Table 7.2. Once the interfile header was created, the projection data (Figure 7.6) can be displayed through an IDL program and saved as a sinogram (CBCT.s) file for reconstruction.

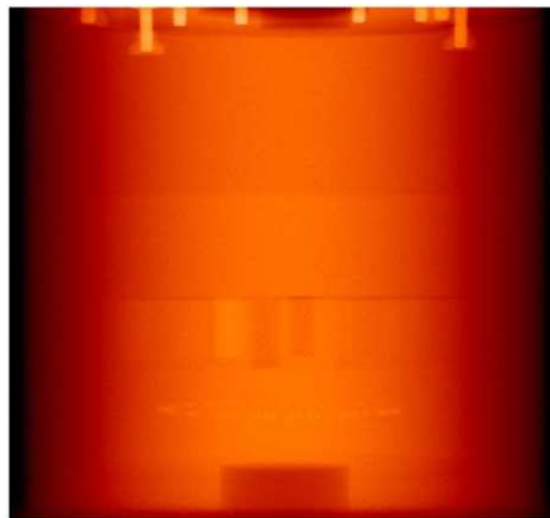


Figure 7.6 Catphan projection displayed using IDL program

All reconstruction processing used the Macquarie University program (v3.3) written in C. The scripts that permitted specification of different reconstruction parameters were generated with a text editor that permitted the user to specify all relevant parameters. The scripts were then run on the Linux system.

A sample script to reconstruct the projections contained in the file CBCT.s is shown below. It incorporates arguments (in order) that specify: 10 ordered subsets, 16 iterations, DDR correction (*collconst* and *collscale* variables are obtained from equation 7.5 after transformation to Gaussian width in σ), reconstructing parameters that includes the slice range (here slices from 1 to 12 in step of 1 are reconstructed), starting with an initial estimate of a cylinder described in the file 'circle512.r'. The reconstructed image output file in this example was named CBCT_recon.r as specified by the '-Recon:' argument in the script.

```
#!/bin/csh
echo "running fanCBCT12 on wiz..zzzzz at whishhhh-speed ++++"
r CBCT.s -OS:+10,0 -Iterations:16 \
-StartImage: circle512.r \
-Collconst: 0.3130 -CollScale: 0.00065 \
-Recon:CBCT_recon -NoStats
```

The reconstructions of the high contrast module of Catphan containing 21 lp/cm at various iterations are shown in Figure 7.7. The results show that for more than 8 iterations, more high spatial frequencies are recovered resulting in sharper images but with progressively increased noise. The images are dominated by a circular artefact which spans the same angular range as the blocks that comprise the resolution testing component of the phantom. It appears that this circular artefact is centred on the matrix rather than the phantom. Its origin is unknown. The reconstructed image with 16 iterations appeared to provide the best compromise between spatial resolution and noise and the circular artefact was much less pronounced. The background shows a uniform intensity with slight difference compared to outer ring of the Catphan. Ring-like artefacts are visible across the line pairs which pass through the inner side of the phantom blocks on the left and the outer side on the right.

Table 7.2 Interfile header created to feed into OSEM algorithm

<pre> !INTERFILE := !imaging modality := nucmed !originating system := none !version of keys := 3.3 !date of keys := 1992:01:01 !conversion program := QEH/UTS/Westmead !program author := !program version := V3.3 !program date := Oct 10 2001 !GENERAL DATA := data description := none !data offset in bytes := 0 !name of data file := CBCT.viv patient name := PHANTOM !patient ID := CATPHAN patient sex := !study ID := CBCT exam type := none data compression := none data encode := none !GENERAL IMAGE DATA := !type of data := tomographic !total number of images := 360 study date := 2013:2:28 study time := 15:16:17 imagedata byte order := littleendian !number of energy windows := 1 energy window [1] := flood corrected := n </pre>	<pre> decay corrected := n !SPECT STUDY (General) := !number of detector heads := 1 !process status := acquired number of images/energy window := 360 !matrix size [1] := 1024 !matrix size [2] := 768 !number format := short float !number of bytes per pixel := 4 !scaling factor (mm/pixel) [1] := 0.388 !scaling factor (mm/pixel) [2] := 0.388 !number of projections := 360 !extent of rotation := 193.41 !time per projection (sec) := 0.09 study duration (sec) := 33 !maximum pixel count := 4444 patient orientation := head in patient rotation := supine !SPECT STUDY (acquired data) := !direction of rotation := CCW start angle := 0 first projection angle in data set := -75.7 acquisition mode := continuous centre of rotation := single value x_offset := 0.8 y_offset := 0 radius of rotation := 500 crystal to focus := 1500 !END OF INTERFILE := </pre>
--	---

A transmission-based scatter model was also used in this algorithm to model the scatter components in the given object. The reconstructed image that includes scatter fraction does not appear to show any improvement. This showed that the algorithm could not model the scatter for transmission-based measurements as the scatter condition for transmission-based tomography is very different from that of emission-based tomography. Further modifications to this algorithm to include scatter of transmitted photons, X-ray spectrum; detector energy response and source geometry would be required to make its photon transport model appropriate for CBCT. The algorithm would, however, still be limited to fan-beam geometry. However, this would demonstrate its potential for its extension to cone-beam reconstruction.

The details showing the reconstruction parameters and the estimated time will appear on the terminal as below once the process begins.

Algorithm used	: OSEM
Time slices used	: 1
Sinogram Filename	: CBCT.s (512 360 12)
Lambda Filename	: CBCT_recon.r (512 512 12)
Starting Image Filename	: circle512.r
Attenuation	: none
Transmission Sinogram Scaling	: none
Maximum A Posteriori (OSL)	: none
Ordered Subset Pattern	: +10,0 (36 subsets)
Sweep degrees	: 195 Counter Clockwise
Sweep start angle (degrees)	: 0
Radii of projection x, y (mm)	: 500.000 500.000
Camera Centre Offset x, y (mm)	: 0.800 0.000
Width slice, bin, pixel (mm)	: 0.775, 0.775, 0.775
Collimator Model	: 0.001xDistance+0.313
Fan-beam focus in mm	: 1500.000, 0.000
Maximum iteration	: 16
Projection bins, slices	: 3, 1
Set up time	: 1.5 seconds

Total 413.6 seconds ; Average/iteration 25.9 seconds

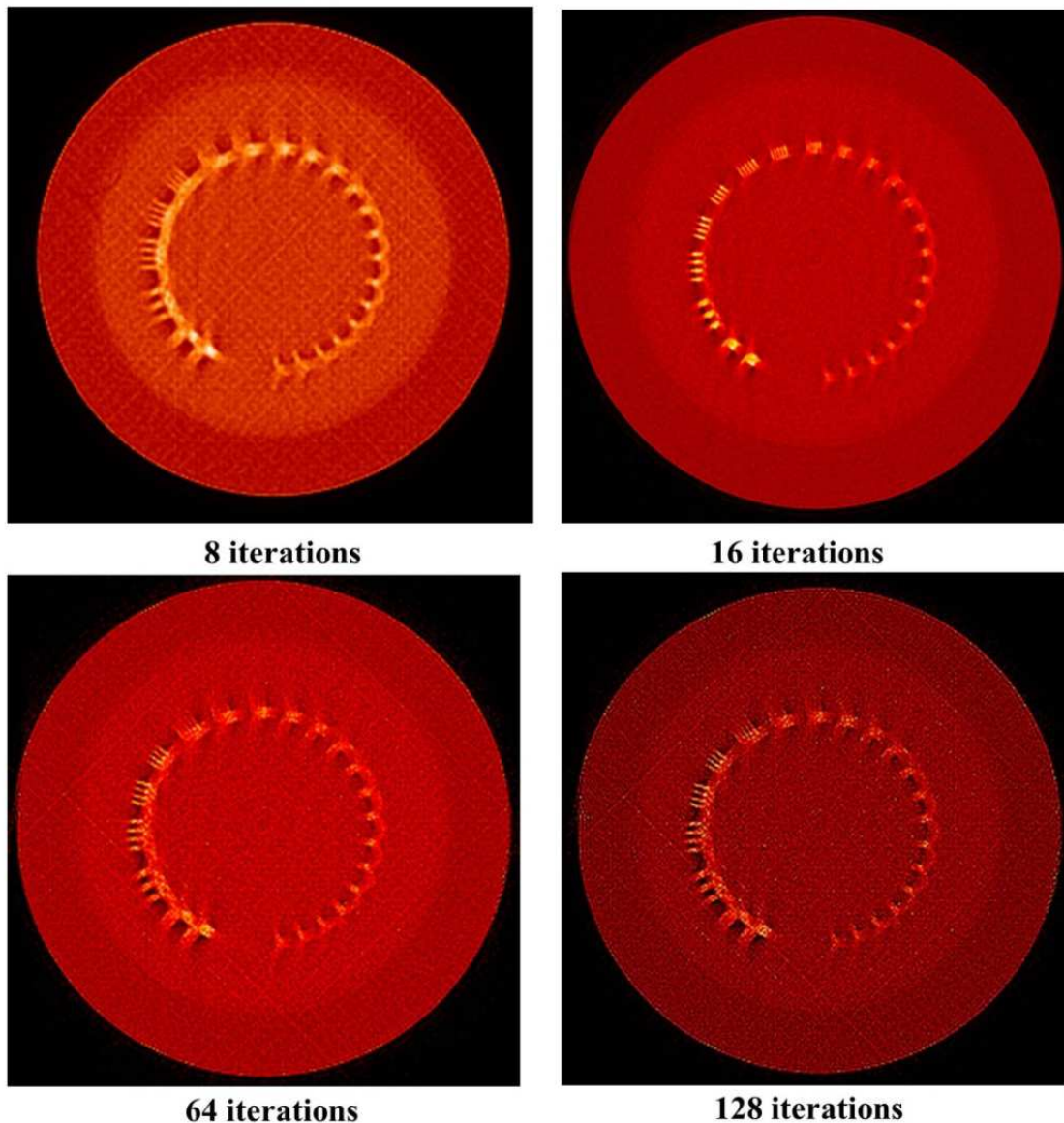


Figure 7.7 Reconstructed axial slices of high contrast section of Catphan (containing line pairs) with DDR and COR corrections

7.6 Discussion

Cone-beam CT provides attenuation coefficient maps for anatomical correlation. The OSEM package used in this study is intended for fan-beam geometry. With CBCT, the rays away from the central axis do not converge to produce accurate reconstruction with fan-beam geometry. Hence slices from the central plane were chosen and fed into the OSEM reconstruction program. The main drawback with this method is that since only a portion of volume is reconstructed at any time; the volumetric images cannot be obtained. The use of DDR and COR corrections in image reconstruction was necessary to obtain spatial resolution comparable with that from FDK reconstruction. The inclusion of scatter fraction

for transmission-based measurements showed no improvement in the reconstructed image when compared to that of the image obtained without scatter correction. Figure 7.8 shows the reconstructed axial slice of the Catphan using transmission-based scatter correction for 16 iterations and the image was found to be similar to that of image obtained for 16 iterations in Figure 7.7. This showed that the program can only model the processes of emission photon transport.

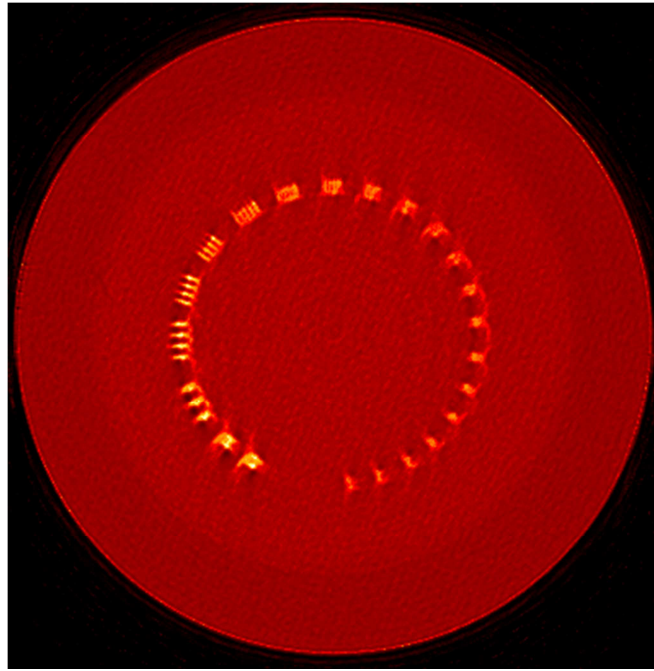


Figure 7.8 Reconstructed axial slice of high contrast section of Catphan (containing line pairs) with scatter correction

This study was an attempt to investigate the effect of iterative reconstruction on CBCT images when compared to the FDK algorithm. It is seen from the results that the image obtained using 16 iterations converges well with uniform background and is smoother than those from a higher number of iterations. However, ring-like artefacts were visible around line pairs and persist for all numbers of iterations. These artefacts were most likely due to the absence of source geometry and scatter from the model. Hence the spatial resolution of the CBCT images reconstructed from this algorithm is not comparable to FDK-based reconstruction which is shown in Figure 7.9. Due to the intrinsic differences in data handling between FDK and iterative reconstruction, images from iterative reconstruction may have a different appearance (e.g., noise texture) from those using FDK reconstruction. In the FDK-based reconstruction image, crescent-shaped artefacts (refer section 2.5.1) were seen around the periphery of the phantom along with the streaks across line pairs in

the upper half of the phantom. However, the spatial resolution of FDK-based reconstruction was higher and measured up to 7 lp/cm. As modifying the entire OSEM program would be more time consuming, the intermediate results of fan-beam reconstruction with incomplete modelling of photon transport were taken as a potential step for possible future work in this regard.

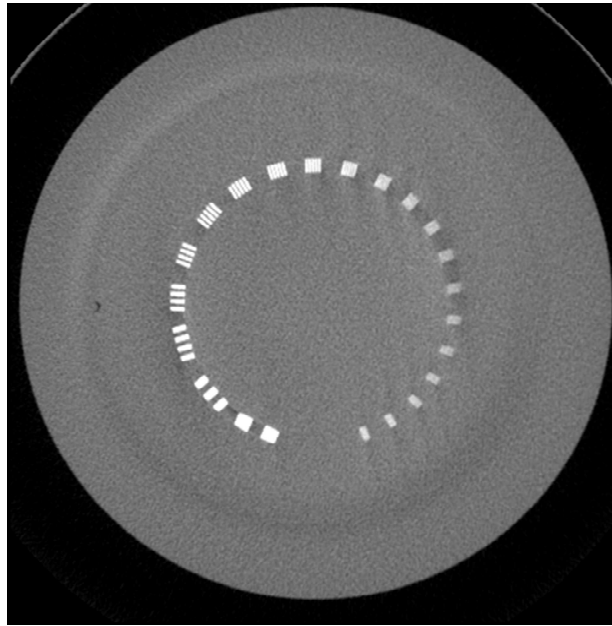


Figure 7.9 FDK-based reconstruction of high contrast section of Catphan (containing line pairs)

High computation load has always been the greatest challenge for iterative reconstruction and has impeded its use in clinical imaging. Software and hardware methods are being investigated to accelerate iterative reconstruction. With further advances in computational technology, iterative reconstruction may be incorporated into routine clinical practice in the future.

Chapter 8

Conclusions

8.1 Summary and Conclusions

This thesis has presented the implementation of modifications to a cone-beam reconstruction algorithm for full-fan scans, and different tests were performed to investigate the applications of CBCT in radiotherapy treatment planning. The tests were divided into the following parts: (i) study of current status of Varian CBCT-based treatment planning, (ii) CBCT image quality assessment based on varying reconstruction filters and number of projections, (iii) CBCT image reconstruction algorithm development, (iv) investigation of an in-house reconstructed CBCT-based dose distribution for treatment planning and comparison to that of PCT-based planning, and (v) iterative-based CBCT reconstruction using the OSEM algorithm.

With significant modifications to the in-house developed FDK algorithm including the weighting factors for data redundancy, non-equal cone angles, various interpolation methods, several choice for reconstruction filters and creation of Mex files to speed up the reconstruction process, the experimental results confirmed the potential of CBCT images for radiotherapy treatment planning.

In Appendix A, Matlab codes that were used to implement an existing FDK algorithm, and a modified filtered back-projection algorithm for cone-beam geometry are given. In Appendix B, C++ codes that were developed to generate a MEX file for faster computation are given.

8.1.1 Current Status of Varian OBI-based Treatment Planning

The Varian CBCT images were investigated for treatment planning using several available phantoms in the department of Medical Physics at RAH and the dose distributions were compared quantitatively using Gamma analysis. Further, the results were extended to a patient study to demonstrate the use of CBCT datasets for treatment planning. It was demonstrated from the results that the treatment plans created with CBCT images using a Catphan calibration curve agreed well with that of PCT plans. However the dose

distributions of plans created from CBCT images were found to depend on the calibration phantom dimensions. This indicates the need for calibration phantoms that match the size of the treatment site to be imaged.

8.1.2 Effect of Reconstruction Filters on CBCT Image Quality

The effect of reconstruction filters on the full-fan and half-fan acquisition modes of CBCT was investigated and the image quality parameters of CNR, spatial resolution, pixel stability and uniformity were assessed. The results of this study show the relationship between the noise and resolution of a CBCT image by using different reconstruction filters and provide possible estimations of the impact of filters on image quality and subsequent optimization for image-guided radiotherapy purposes. From the results, it was demonstrated that the spatial resolution given by the Ram-Lak filter is the highest and that given by the Hann filter is the lowest. The Hamming filter was found to be the optimal filter for noise reduction by providing the least variation in the average pixel values. Thus this study provides us a protocol to optimise the choice of reconstruction filter depending upon the anatomical site of interest.

8.1.3 CBCT Image Reconstruction Algorithm Development

Based on a practical method to reconstruct cone-beam images, an algorithm was developed using Matlab. The algorithm was extensively modified and all the pre-processing steps including weighting factors for data redundancy and non-equal cone angles were developed. To reduce reconstruction time dramatically, MEX files were generated to increase the computational speed by a factor of 30. From the results of image reconstruction, it was demonstrated that the image quality of cone-beam images can be improved by using Parker weighting correction and a correction for non-equal cone angles. Further, the use of air-scan projections for each gantry angle reduced the wobbling effect of the bow-tie filter during acquisition and as a result, the crescent-shaped artefact evident in the Varian reconstruction algorithm was not seen on images from the in-house developed algorithm. The use of 2D adaptive filters helps in reducing the noise level without significant loss of high frequency components in the image. The spatial resolution of the in-house reconstructed image estimated at 10% MTF was about 13% better than that of Varian images.

8.1.4 Investigation of In-house Reconstructed Images for Treatment Planning

Cone-beam images of the Rando phantom were reconstructed using the in-house developed algorithm and the image quality was compared with Varian reconstructed images. The reconstructed images were then investigated for treatment planning. It was found that the in-house reconstructed CBCT dose distributions were in good agreement with those of PCT-based planning with 99.8% pass using the Gamma criteria/analysis. Although the developed reconstruction method produced cone-beam image quality slightly superior to the Varian images, the IMRT dose distributions obtained from in-house reconstructed images could not produce a 100% pass rate when compared with the PCT image. This is possibly due to the fact that the in-house algorithm does not include several artefact correction steps, such as beam hardening correction, ring artefact suppression and scatter reduction that were included in the Varian reconstruction, due to complexity in development and the time it would take. The results thus demonstrate the potential of the in-house reconstruction algorithm as a research tool for implementing various artefact corrections such as scatter, beam hardening, and ring suppression. The implementation provides a useful base platform for developing artefact correction algorithms and for conducting image quality tests by changing the interpolation methods or reconstruction filters.

8.1.5 Iterative-based CBCT Reconstruction

An approach to reconstructing cone-beam images iteratively based on an expectation-maximisation algorithm was studied. Though the reconstruction package is intended for fan-beam CT, the central plane of a cone-beam projection - which is equivalent to a fan-beam projection - was used in this study to investigate the potential of iterative reconstruction in CBCT. The image reconstructed using 16 iterations converge well with uniform background and is smoother compared to higher number of iterations.

8.2 Future Work

As CBCT has become more popular for IGRT purposes, the results of this study underline the need for further investigations into the effects of using different cone-beam reconstruction methods and filtration. A rigorous clinical study of CBCT-based treatment

planning using the in-house developed reconstruction images would be a useful extension of this work. Additional measurements imaging a torso-sized object could be considered, as this study used a head-sized phantom with full-scan geometry. Torso-sized objects would require half-fan geometry. In order to reconstruct half-fan scans further modifications to the code to acquire large volume objects would be required.

Further work could be done on improving the FDK reconstruction speed in order to use CBCT datasets for adaptive radiotherapy. On Varian OBI, reducing the imager frame rate from the present 30 fps should be possible, although it is not currently used and assistance from Varian would be needed to enable this in clinical mode. The benefit of this would be in providing fewer projections to handle, and hence faster image reconstruction. The code can also be made to run faster by parallel computations. Hence an effective, parallel, GPU-based implementation of this algorithm can possibly be built for user friendly operations. Development of various artefact corrections such as scatter, beam hardening, cupping, ring and noise suppression would greatly improve the cone-beam image quality, making this research tool useful in the clinic.

The iterative-based CBCT reconstruction method used in this study has to be modified in terms of the photon transport model in order to be appropriate for cone-beam geometry. To do this, further modifications to the algorithm to include cone-beam source geometry, scatter of transmitted photons, x-ray spectrum and detector energy response would be required. This would demonstrate the potential of this algorithm for cone-beam reconstruction.

References

- Ahnesjo, A 1989, 'Collapsed cone convolution of radiant energy for photon dose calculation in heterogeneous media', *Medical Physics*, vol. 16, no. 4, pp. 577-592.
- Allen, B, Marcu, L & Bezak, E 2012, *Biomedical physics in radiotherapy for cancer*, CSIRO Publishing.
- Amer, A, Marchant, T, Sykes, J, Czajka, J & Moore, C 2007, 'Imaging doses from the Elekta Synergy X-ray cone beam CT system', *British Journal of Radiology*, vol. 80, no. 954, pp. 476-482.
- Anas, EMA, Kim, J, Lee, SY & Hasan, MK 2011, 'Ring artifact corrections in flat-panel detector based cone beam CT', in NJ Pelc, E Samei & RM Nishikawa (eds), Lake Buena Vista, Florida, USA, vol. 7961, pp. 79612S-79610.
- Ashrafuzzaman, ANM, Lee, SY & Hasan, MK 2011, 'A self-adaptive approach for the detection and correction of stripes in the sinogram: suppression of ring artifacts in CT imaging', *EURASIP Journal on Advances in Signal Processing*, vol. 2011, pp. 1-13.
- Baker, GR 2006, 'Localization: conventional and CT simulation', *British Journal of Radiology*, vol. 79, no. Special Issue 1, September 1, 2006, pp. S36-S49.
- Bissonnette, J-P, Franks, KN, Purdie, TG, Moseley, DJ, Sonke, J-J, Jaffray, DA, Dawson, LA & Bezjak, A 2009, 'Quantifying interfraction and intrafraction tumor motion in lung stereotactic body radiotherapy using respiration-correlated cone beam computed tomography', *International Journal of Radiation Oncology Biology Physics*, vol. 75, no. 3, pp. 688-695.
- Bissonnette, JP, Moseley, DJ & Jaffray, DA 2008, 'A quality assurance program for image quality of cone-beam CT guidance in radiation therapy', *Medical Physics*, vol. 35, no. 5, May, pp. 1807-1815.
- Blessing, M, Stsepankou, D, Wertz, H, Arns, A, Lohr, F, Hesser, J & Wenz, F 2010, 'Breath-hold target localization with simultaneous kilovoltage/megavoltage cone-beam computed tomography and fast reconstruction', *International Journal of Radiation Oncology Biology Physics*, vol. 78, no. 4, Nov 15, pp. 1219-1226.
- Boda-Heggemann, J, Lohr, F, Wenz, F, Flentje, M & Guckenberger, M 2011, 'kV Cone-beam CT-based IGRT', *Strahlentherapie und Onkologie*, vol. 187, no. 5, pp. 284-291.
- Bushberg, J, Seibert, J, Leidholdt, E & Boone, J 2002, *The essential physics of medical imaging*, LIPPINCOTT WILLIAMS & WILKINS.
- Chen, L, Shaw, CC, Altunbas, MC, Lai, CJ & Liu, X 2008, 'Spatial resolution properties in cone beam CT: a simulation study', *Medical Physics*, vol. 35, no. 2, Feb, pp. 724-734.

- Den, RB, Doemer, A, Kubicek, G, Bednarz, G, Galvin, JM, Keane, WM, Xiao, Y & Machtay, M 2010, 'Daily image guidance with cone-beam computed tomography for head-and-neck cancer intensity-modulated radiotherapy: a prospective study', *International Journal of Radiation Oncology Biology Physics*, vol. 76, no. 5, Apr, pp. 1353-1359.
- Depuydt, T, Slagmolen, P, Van den Heuvel, F & Hrbacek, J 2006, 'Cone-beam CT Hounsfield unit correction method and application on images of the pelvic region', *Radiotherapy and Oncology*, vol. 81, p. S29.
- Dietrich L, JSTTNS & Oelfke, U 2006, 'Linac-integrated 4D cone beam CT: first experimental results', *Physics in Medicine and Biology*, vol. 51, no. 11, p. 2939.
- Ding, GX & Coffey, CW 2009, 'Radiation dose from kilovoltage cone beam computed tomography in an image-guided radiotherapy procedure', *International Journal of Radiation Oncology Biology Physics*, vol. 73, no. 2, pp. 610-617.
- Ding, GX, Duggan, DM & Coffey, CW 2008, 'Accurate patient dosimetry of kilovoltage cone-beam CT in radiation therapy', *Medical Physics*, vol. 35, no. 3, pp. 1135-1144.
- Ding, GX, Duggan, DM, Coffey, CW, Deeley, M, Hallahan, DE, Cmelak, A & Malcolm, A 2007, 'A study on adaptive IMRT treatment planning using kV cone-beam CT', *Radiotherapy and Oncology*, vol. 85, no. 1, pp. 116-125.
- Downes, P, Jarvis, R, Radu, E, Kawrakow, I & Spezi, E 2009, 'Monte Carlo simulation and patient dosimetry for a kilovoltage cone-beam CT unit', *Medical Physics*, vol. 36, no. 9, pp. 4156-4167.
- Droege, RT & Morin, RL 1982, 'A practical method to measure the MTF of CT scanners', *Medical Physics*, vol. 9, no. 5, pp. 758-760.
- Elstrøm, UV, Muren, LP, Petersen, JBB & Grau, C 2011, 'Evaluation of image quality for different kV cone-beam CT acquisition and reconstruction methods in the head and neck region', *Acta Oncologica*, vol. 50, no. 6, pp. 908-917.
- Elstrom, UV, Wysocka, BA, Muren, LP, Petersen, JB & Grau, C 2010, 'Daily kV cone-beam CT and deformable image registration as a method for studying dosimetric consequences of anatomic changes in adaptive IMRT of head and neck cancer', *Acta Oncologica*, vol. 49, no. 7, pp. 1101-1108.
- Endo, M, Tsunoo, T, Nakamori, N & Yoshida, K 2001, 'Effect of scattered radiation on image noise in cone beam CT', *Medical Physics*, vol. 28, no. 4, pp. 469-474.
- Feldkamp, LA, Davis, LC & Kress, JW 1984, 'Practical cone-beam algorithm', *Journal of the Optical Society of America A*, vol. 1, no. 6, pp. 612-619.
- Foroudi, F, Wong, J, Kron, T, Rolfo, A, Haworth, A, Roxby, P, Thomas, J, Herschtal, A, Pham, D, Williams, S, Tai, KH & Duchesne, G 2011, 'Online adaptive radiotherapy for muscle-invasive bladder cancer: results of a pilot study', *International Journal of Radiation Oncology Biology Physics*, vol. 81, no. 3, pp. 765-771.

Giles, W, Bowsher, J, Li, H & Yin, FF 2011, 'Crescent artifacts in cone-beam CT', *Medical Physics*, vol. 38, no. 4, pp. 2116-2121.

Gottlieb, KL, Hansen, CR, Hansen, O, Westberg, J & Brink, C 2010, 'Investigation of respiration induced intra- and inter-fractional tumour motion using a standard cone beam CT', *Acta Oncologica*, vol. 49, no. 7, pp. 1192-1198.

Graham, SA, Moseley, DJ, Siewerdsen, JH & Jaffray, DA 2007, 'Compensators for dose and scatter management in cone-beam computed tomography', *Medical Physics*, vol. 34, no. 7, pp. 2691-2703.

Grills, IS, Hope, AJ, Guckenberger, M, Kestin, LL, Werner-Wasik, M, Yan, D, Sonke, JJ, Bissonnette, JP, Wilbert, J, Xiao, Y & Belderbos, J 2012, 'A collaborative analysis of stereotactic lung radiotherapy outcomes for early-stage non-small-cell lung cancer using daily online cone-beam computed tomography image-guided radiotherapy', *Journal of Thoracic Oncology*, vol. 7, no. 9, pp. 1382-1393.

Guan, H & Dong, H 2009, 'Dose calculation accuracy using cone-beam CT (CBCT) for pelvic adaptive radiotherapy', *Physics in Medicine and Biology*, vol. 54, no. 20, pp. 6239-6250.

Guckenberger, M, Meyer, J, Wilbert, J, Baier, K, Sauer, O & Flentje, M 2007, 'Precision of image-guided radiotherapy (IGRT) in six degrees of freedom and limitations in clinical practice', *Strahlentherapie und Onkologie*, vol. 183, no. 6, pp. 307-313.

Hara, AK, Paden Rg Fau - Silva, AC, Silva Ac Fau - Kujak, JL, Kujak JI Fau - Lawder, HJ, Lawder Hj Fau - Pavlicek, W & Pavlicek, W 2009, 'Iterative reconstruction technique for reducing body radiation dose at CT: feasibility study', no. 1546-3141 (Electronic), 20090821 DCOM- 20090929.

Hårdemark, B, Liander, A, Rehbinder, H & Johan Löf 2004, *P3IMRT® Direct machine parameter optimization*, Pinnacle3 white Paper, RaySearch Laboratories AB, Stockholm Sweden.

Hatton, J, McCurdy, B & Greer, PB 2009, 'Cone beam computerized tomography: the effect of calibration of the hounsfield unit number to electron density on dose calculation accuracy for adaptive radiation therapy', *Physics in Medicine and Biology*, vol. 54, no. 15, pp. N329-346.

Hawkins, MA, Brooks, C, Hansen, VN, Aitken, A & Tait, DM 2010, 'Cone beam computed tomography-derived adaptive radiotherapy for radical treatment of esophageal cancer', *International Journal of Radiation Oncology Biology Physics*, vol. 77, no. 2, pp. 378-383.

Houser, C, Nawaz, A & Galvin, J 2006, 'Quantitive evaluation of cone beam ct data used for treatment planning', *Medical Physics*, vol. 33, pp. 2285 - 2286.

Hsieh, J, Molthen, RC, Dawson, CA & Johnson, RH 2000, 'An iterative approach to the beam hardening correction in cone beam CT', *Medical Physics*, vol. 27, no. 1, pp. 23-29.

Hudson, HM & Larkin, RS 1994, 'Accelerated image reconstruction using ordered subsets of projection data', *IEEE Transactions on Medical Imaging*, vol. 13, no. 4, pp. 601-609.

Hyer, DE, Serago, CF, Kim, S, Li, JG & Hintenlang, DE 2010, 'An organ and effective dose study of XVI and OBI cone-beam CT systems', *Journal of Applied Clinical Medical Physics*, vol. 11, no. 2, p. 3183.

Islam, MK, Purdie, TG, Norrlinger, BD, Alasti, H, Moseley, DJ, Sharpe, MB, Siewerdsen, JH & Jaffray, DA 2006, 'Patient dose from kilovoltage cone beam computed tomography imaging in radiation therapy', *Medical Physics*, vol. 33, no. 6, pp. 1573-1582.

Jaffray, D & Siewerdsen, J 2000, 'Cone-beam computed tomography with a flat-panel imager: initial performance characterization', *Medical Physics*, vol. 27, no. 6, pp. 1311-1323.

Jaffray, D, Siewerdsen, J, Wong, J & Martinez, A 2002, 'Flat-panel cone-beam computed tomography for image-guided radiation therapy', *International Journal of Radiation Oncology Biology Physics*, vol. 53, no. 5, p. 1337.

Jia, X, Dong, B, Lou, Y & Jiang, SB 2011, 'GPU-based iterative cone-beam CT reconstruction using tight frame regularization', *Physics in Medicine and Biology*, vol. 56, no. 13, pp. 3787-3807.

Kak, AC 2001, *Principles of computerized tomographic imaging*, Avinash C. Kak, Malcolm Slaney, ed. M Slaney, Philadelphia : Society for Industrial and Applied Mathematics, Philadelphia.

Kalender, WA 2011, *Computed tomography : fundamentals, system technology, image quality, applications*, Publicus Publishing, Erlangen, Germany.

Kamath, S, Song, W, Chvetsov, A, Ozawa, S, Lu, H, Samant, S, Liu, C, Li, JG & Palta, JR 2011, 'An image quality comparison study between XVI and OBI CBCT systems', *Journal of Applied Clinical Medical Physics*, vol. 12, no. 2, p. 3435.

Kan, MWK, Leung, LHT, Wong, W & Lam, N 2008, 'Radiation dose from cone beam computed tomography for image-guided radiation therapy', *International Journal of Radiation Oncology Biology Physics*, vol. 70, no. 1, pp. 272-279.

Kim, S, Yoshizumi, TT, Toncheva, G, Yoo, S & Yin, FF 2008, 'Comparison of radiation doses between cone beam CT and multi detector CT: TLD measurements', *Radiation Protection Dosimetry*, vol. 132, no. 3, pp. 339-345.

Lagerwaard, FJ, Van Sornsen de Koste, JR, Nijssen-Visser, MR, Schuchhard-Schipper, RH, Oei, SS, Munne, A & Senan, S 2001, 'Multiple "slow" CT scans for incorporating lung tumor mobility in radiotherapy planning', *International Journal of Radiation Oncology Biology Physics*, vol. 51, no. 4, pp. 932-937.

Lange, K & Carson, R 1984, 'EM reconstruction algorithms for emission and transmission tomography', *Journal of Computer Assisted Tomography*, vol. 8, no. 2, pp. 306-316.

- Lawson, JD, Jani, AB, Schreibmann, E & Fox, T 2007, 'Quantitative evaluation of a cone-beam computed tomography-planning computed tomography deformable image registration method for adaptive radiation therapy', *Journal of Applied Clinical Medical Physics*, vol. 8, no. 4, pp. 96-113.
- Létourneau, D, Kim, LH, Oldham, M, Wong, JW, Lockman, D, Watt, L, Martinez, A, Hugo, G, Chen, PY & Yan, D 2005, 'Cone-beam-CT guided radiation therapy: a model for on-line application', *Radiotherapy and Oncology*, vol. 75, no. 3, pp. 271-278.
- Li, Xing, L, Chao, M, Yang, Y, Loo, B, Koong, A, Munro, P & McGuinness, C 2006, 'Four-dimensional cone-beam computed tomography using an on-board imager', *Medical Physics*, vol. 33, no. 10, p. 3825.
- Li, Zhu, XR, Zhang, L, Dong, L, Tung, S, Ahamad, A, Chao, KS, Morrison, WH, Rosenthal, DI, Schwartz, DL, Mohan, R & Garden, AS 2008, 'Comparison of 2D radiographic images and 3D cone beam computed tomography for positioning head-and-neck radiotherapy patients', *International Journal of Radiation Oncology Biology Physics*, vol. 71, no. 3, pp. 916-925.
- Lo, T, Yang, Y, Schreibmann, E, Li, T & Xing, L 2005, 'Mapping electron density distribution from planning ct to cone-beam CT (CBCT): a novel strategy for accurate dose calculation based on CBCT', *International Journal of Radiation Oncology Biology Physics*, vol. 63, Supplement 1, no. 0, p. S507.
- Low, DA, Harms, WB, Mutic, S & Purdy, JA 1998, 'A technique for the quantitative evaluation of dose distributions', *Medical Physics*, vol. 25, no. 5, pp. 656-661.
- Lu, J, Guerrero, TM, Munro, P, Jeung, A, Chi, PC, Balter, P, Zhu, XR, Mohan, R & Pan, T 2007, 'Four-dimensional cone beam CT with adaptive gantry rotation and adaptive data sampling', *Medical Physics*, vol. 34, no. 9, pp. 3520-3529.
- Maass, C, Dennerlein, F, Noo, F & Kachelriess, M 2010, 'Comparing short scan CT reconstruction algorithms regarding cone-beam artifact performance', *Nuclear Science Symposium Conference Record (NSS/MIC), 2010 IEEE*, pp. 2188-2193.
- Mail, N, Moseley, D, Siewerdsen, J & Jaffray, D 2008, 'The influence of bowtie filtration on cone-beam CT image quality', *Medical Physics*, vol. 36, no. 1, pp. 22-32.
- McCarthy, C, MacBain, C, Moore, CJ, Sykes, JR, Price, P, Stratford, J, Amer, A, Henry, A, Davies, J, Williams, PC & Marchant, T 2006, 'Developments in and experience of kilovoltage X-ray cone beam image-guided radiotherapy', *British Journal of Radiology*, vol. 79, Sp. Iss. pp. S66-S78.
- McNutt, T 2007, *Pinnacle³ Dose calculations*, Philips Medical systems, Netherlands.
- Meikle, SR, Hutton, BF & Bailey, DL 1994, 'A transmission-dependent method for scatter correction in SPECT', *Journal of Nuclear Medicine*, vol. 35, no. 2, pp. 360-367.

Morin, O, Chen, J, Aubin, M, Gillis, A, Aubry, J-F, Bose, S, Chen, H, Descovich, M, Xia, P & Pouliot, J 2007, 'Dose calculation using megavoltage cone-beam CT', *International Journal of Radiation Oncology Biology Physics*, vol. 67, no. 4, pp. 1201-1210.

Mueller, K, Yagel, R & Wheller, JJ 1999a, 'Anti-aliased three-dimensional cone-beam reconstruction of low-contrast objects with algebraic methods', *IEEE Transactions on Medical Imaging*, vol. 18, no. 6, pp. 519-537.

Mueller, K, Yagel, R & Wheller, JJ 1999b, 'Fast implementations of algebraic methods for three-dimensional reconstruction from cone-beam data', *IEEE Transactions on Medical Imaging*, vol. 18, no. 6, pp. 538-548.

Murphy, MJ, Balter, J, Balter, S, BenComo, JA, Jr., Das, IJ, Jiang, SB, Ma, CM, Olivera, GH, Rodebaugh, RF, Ruchala, KJ, Shirato, H & Yin, FF 2007, 'The management of imaging dose during image-guided radiotherapy: report of the AAPM Task Group 75', *Medical Physics*, vol. 34, no. 10, pp. 4041-4063.

Nijkamp, J, Pos, FJ, Nuver, TT, de Jong, R, Remeijer, P, Sonke, J-J & Lebesque, JV 2008, 'Adaptive radiotherapy for prostate cancer using kilovoltage cone-beam computed tomography: first clinical results', *International Journal of Radiation Oncology Biology Physics*, vol. 70, no. 1, pp. 75-82.

Ning, R, Tang, X & Conover, D 2004, 'X-ray scatter correction algorithm for cone beam CT imaging', *Medical Physics*, vol. 31, no. 5, pp. 1195-1202.

Ning, W, Huaqun, G, Rabih, H, Deepak, P, Nurushev, T, Shidong, L & Benjamin, M 2007, 'Dose delivered from Varian's CBCT to patients receiving IMRT for prostate cancer', *Physics in Medicine and Biology*, vol. 52, no. 8, p. 2267.

Padmanaban, S, Nagarajan, V & Sukumar, P 2010, 'A study on evaluation of kv cone beam CT image based treatment planning using anthropomorphic phantom', *Journal of Medical and Biological Engineering*, vol. 31, no. 6, pp. 429-435.

Palm, A, Nilsson, E & Herrnsdorf, L 2010, 'Absorbed dose and dose rate using the Varian OBI 1.3 and 1.4 CBCT system', *Journal of Applied Clinical Medical Physics*, vol. 11, no. 1, p. 3085.

Parker, DL 1982, 'Optimal short scan convolution reconstruction for fanbeam CT', *Medical Physics*, vol. 9, no. 2, pp. 254-257.

Pawlowski, JM, Yang, ES, Malcolm, AW, Coffey, CW & Ding, GX 2010, 'Reduction of dose delivered to organs at risk in prostate cancer patients via image-guided radiation therapy', *International Journal of Radiation Oncology Biology Physics*, vol. 76, no. 3, pp. 924-934.

Petit, SF, van Elmpt, WJC, Lambin, P & Dekker, ALAJ 2010, 'Dose recalculation in megavoltage cone-beam CT for treatment evaluation: removal of cupping and truncation artefacts in scans of the thorax and abdomen', *Radiotherapy and Oncology*, vol. 94, no. 3, pp. 359-366.

- Petit, SF, van Elmpt, WJC, Nijsten, SMJJG, Lambin, P & Dekker, ALAJ 2008, 'Calibration of megavoltage cone-beam CT for radiotherapy dose calculations: correction of cupping artifacts and conversion of CT numbers to electron density', *Medical Physics*, vol. 35, no. 3, pp. 849-865.
- Polat, B, Wilbert, J, Baier, K, Flentje, M & Guckenberger, M 2007, 'Nonrigid patient setup errors in the head-and-neck region', *Strahlentherapie und Onkologie*, vol. 183, no. 9, pp. 506-511.
- Poludniowski, G, Evans, PM, Hansen, VN & Webb, S 2009, 'An efficient Monte Carlo-based algorithm for scatter correction in keV cone-beam CT', *Physics in Medicine and Biology*, vol. 54, no. 12, pp. 3847-3864.
- Qiu, W, Tong, JR, Mitchell, CN, Marchant, T, Spencer, P, Moore, CJ & Soleimani, M 2010, 'New iterative cone beam CT reconstruction software: Parameter optimisation and convergence study', *Computer Methods and Programs in Biomedicine*, vol. 100, no. 2, pp. 166-174.
- Rezvani, N 2012, 'Iterative reconstruction algorithms for polyenergetic x-ray computerized tomography', University of Toronto.
- Richter, A, Hu, Q, Steglich, D, Baier, K, Wilbert, J, Guckenberger, M & Flentje, M 2008, 'Investigation of the usability of conebeam CT data sets for dose calculation', *Radiation Oncology*, vol. 3, no. 1, p. 42.
- Rinkel, J, Gerfault, L, Esteve, F & Dinten, JM 2007, 'A new method for x-ray scatter correction: first assessment on a cone-beam CT experimental setup', *Physics in Medicine and Biology*, vol. 52, no. 15, pp. 4633-4652.
- Rockmore, AJ & Macovski, A 1976, 'A maximum likelihood approach to emission image reconstruction from projections', *IEEE Transactions on Nuclear Science*, vol. 23, no. 4, pp. 1428-1432.
- Scarfe, W & Farman, A 2007, 'Cone beam computed tomography: a paradigm shift for clinical dentistry', *Australasian Dental Practice*, pp. 102-110.
- Schulze, R, Heil, U, Gross, D, Bruellmann, D, Dranischnikow, E, Schwanecke, U & Schoemer, E 2011, 'Artefacts in CBCT: a review', *Dentomaxillofacial Radiology*, vol. 40, no. 5, pp. 265-273.
- Sharpe, MB, Moseley, DJ, Purdie, TG, Islam, M, Siewerdsen, JH & Jaffray, DA 2006, 'The stability of mechanical calibration for a kV cone beam computed tomography system integrated with linear accelerator', *Medical Physics*, vol. 33, no. 1, pp. 136-144.
- Shepp, LA & Vardi, Y 1982, 'Maximum likelihood reconstruction for emission tomography', *IEEE Transactions on Medical Imaging*, vol. 1, no. 2, pp. 113-122.
- Siewerdsen, J & Jaffray, D 2001, 'Cone-beam computed tomography with a flat-panel imager: magnitude and effects of x-ray scatter', *Medical Physics*, vol. 28, pp. 220 - 231.

Siewerdsen, JH, Daly, MJ, Bakhtiar, B, Moseley, DJ, Richard, S, Keller, H & Jaffray, DA 2006, 'A simple, direct method for x-ray scatter estimation and correction in digital radiography and cone-beam CT', *Medical Physics*, vol. 33, no. 1, pp. 187-197.

Siewerdsen, JH, Jaffray, DA, Richard, S, Moseley, DJ & Bakhtiar, B 2004, 'The influence of antiscatter grids on soft-tissue detectability in cone-beam computed tomography with flat-panel detectors', *Medical Physics*, vol. 31, no. 12, pp. 3506-3515.

Soimu, D, Buliev, I & Pallikarakis, N 2008, 'Studies on circular isocentric cone-beam trajectories for 3D image reconstructions using FDK algorithm', *Computerized Medical Imaging and Graphics*, vol. 32, no. 3, pp. 210-220.

Song, WY, Kamath, S, Ozawa, S, Ani, SA, Chvetsov, A, Bhandare, N, Palta, JR, Liu, C, Li, JG, Rong, Y, Tewatia, D & Paliwal, B 2008, 'A dose comparison study between XVI and OBI CBCT systems, SU-EE-A3-05: Evaluation of Kilo-Voltage Cone Beam CT Image Quality in Context to Dose Re-Computation', *Medical Physics*, vol. 35, no. 2, pp. 480-486.

Sonke, J, Zijp, L, Remeijer, P & van Herk, M 2005, 'Respiratory correlated cone beam CT', *Medical Physics*, vol. 32, no. 4, p. 1176.

Srinivasan, K, Mohammadi, M & Shepherd, J 2014, 'Applications of linac-mounted kilovoltage Cone-beam Computed Tomography in modern radiation therapy: A review', *Polish Journal of Radiology*, vol. 79, pp. 181-193.

Srinivasan, K, Mohammadi, M & Shepherd, J (in press), 'Cone Beam Computed Tomography (CBCT) for adaptive radiotherapy treatment planning', *Journal of Medical and Biological Engineering*, Retrieved 11 June 2014 from <http://jmbe.bme.ncku.edu.tw/AIP/AIP-JMBE%201372.pdf>.

Steinke, MF & Bezak, E 2008, 'Technological approaches to in-room CBCT imaging', *Australasian Physics & Engineering Sciences in Medicine*, vol. 31, no. 3, pp. 167-179.

Sykes, JR, Amer, A, Czajka, J & Moore, CJ 2005, 'A feasibility study for image guided radiotherapy using low dose, high speed, cone beam X-ray volumetric imaging', *Radiotherapy and Oncology*, vol. 77, no. 1, pp. 45-52.

Tang, X, Ning, R, Yu, R & Conover, D 2001, 'Cone beam volume CT image artifacts caused by defective cells in x-ray flat panel imagers and the artifact removal using a wavelet-analysis-based algorithm', *Medical Physics*, vol. 28, no. 5, pp. 812-825.

Thibault, JB, Sauer, KD, Bouman, CA & Hsieh, J 2007, 'A three-dimensional statistical approach to improved image quality for multislice helical CT', *Medical Physics*, vol. 34, no. 11, pp. 4526-4544.

Tucking, T, Nill, S & Oelfke, U 2006, 'Dose calculation on linac integrated KV-cone beam CT', *Radiotherapy and Oncology*, vol. 81, no. Supplement 1, p. S26.

van Kranen, S, van Beek, S, Rasch, C, van Herk, M & Sonke, JJ 2009, 'Setup uncertainties of anatomical sub-regions in head-and-neck cancer patients after offline CBCT guidance',

- International Journal of Radiation Oncology Biology Physics*, vol. 73, no. 5, pp. 1566-1573.
- van Zijtveld, M, Dirkx, M & Heijmen, B 2007, 'Correction of conebeam CT values using a planning CT for derivation of the "dose of the day"', *Radiotherapy and Oncology*, vol. 85, no. 2, pp. 195-200.
- Wang, J, Li, T & Xing, L 2009, 'Iterative image reconstruction for CBCT using edge-preserving prior', *Medical Physics*, vol. 36, no. 1, pp. 252-260.
- Wei, Z, Guo-Tao, F, Cui-Li, S, Yan-Fang, W, Cun-Feng, W, Da-Quan, C, Jie-Min, Q, Xiao, T, Rong-Jian, S, Long, W & Zhong-Qiang, Y 2011, 'Beam hardening correction for a cone-beam CT system and its effect on spatial resolution', *Chinese Physics C*, vol. 35, no. 10, p. 978.
- Wertz, H, Stsepankou, D, Blessing, M, Rossi, M, Knox, C, Brown, K, Gros, U, Boda-Heggemann, J, Walter, C, Hesser, J, Lohr, F & Wenz, F 2010, 'Fast kilovoltage/megavoltage (kVMV) breathhold cone-beam CT for image-guided radiotherapy of lung cancer', *Physics in Medicine and Biology*, vol. 55, no. 15, pp. 4203-4217.
- Wong, R, Moseley, D, Gospodarowicz, M, Jaffray, D, Sharpe, M, Letourneau, D & Ansell, S 2007, 'Online planning and delivery technique for radiotherapy of spinal metastases using cone-beam CT: image quality and system performance', *International Journal of Radiation Oncology Biology Physics*, vol. 67, no. 4, pp. 1229-1237.
- Wu, Thongphiew, D, Wang, Z, Mathayomchan, B, Chankong, V, Yoo, S, Lee, WR & Yin, FF 2008, 'On-line re-optimization of prostate IMRT plans for adaptive radiation therapy', *Physics in Medicine and Biology*, vol. 53, no. 3, pp. 673-691.
- Wu, Y, Yan, D, Sharpe, M, Miller, B & Wong, J 2001, 'Implementing multiple static field delivery for intensity modulated beams', *Medical Physics*, vol. 28, no. 11, pp. 2188-2197.
- Yan, H, Cervino, L, Jia, X & Jiang, SB 2012, 'A comprehensive study on the relationship between the image quality and imaging dose in low-dose cone beam CT', *Physics in Medicine and Biology*, vol. 57, no. 7, pp. 2063-2080.
- Yang, K, Kwan, AL, Huang, SY, Packard, NJ & Boone, JM 2008, 'Noise power properties of a cone-beam CT system for breast cancer detection', *Medical Physics*, vol. 35, no. 12, pp. 5317-5327.
- Yang, Y, Schreibmann, E & Li, T 2007, 'Evaluation of on-board kV cone beam CT (CBCT)-based dose calculation', *Physics in Medicine and Biology*, vol. 52, pp. 685 - 705.
- Yokei, T, Shinohara, H & Onishi, H 2002, 'Performance evaluation of OSEM reconstruction algorithm incorporating three-dimensional distance-dependent resolution compensation for brain SPECT: A simulation study', *Annals of nuclear medicine*, vol. 16, no. 1, pp. 11-18.
- Yoo, S, Kim, G, Hammoud, R, Elder, E, Pawlicki, T, Guan, H, Fox, T, Luxton, G, Yin, F & Munro, P 2007, 'A quality assurance program for the On-Board Imager®', in R

Magjarevic & JH Nagel (eds), *World Congress on Medical Physics and Biomedical Engineering 2006*, vol. 14, Springer Berlin Heidelberg, pp. 1793-1796.

Yoo, S & Yin, F 2006, 'Dosimetric feasibility of cone-beam CT-based treatment planning compared to CT-based treatment planning', *International Journal of Radiation Oncology Biology Physics*, vol. 66, no. 5, pp. 1553-1559.

Yu, L, Pan, X & Pelizzari, CA 2004, 'Image reconstruction with a shift-variant filtration in circular cone-beam CT', *International Journal of Imaging Systems and Technology*, vol. 14, no. 5, pp. 213-221.

Zheng, D, Ford, JC, Lu, J, Lazos, D, Hugo, GD, Pokhrel, D, Zhang, L & Williamson, JF 2011, 'Bow-tie wobble artifact: effect of source assembly motion on cone-beam CT', *Medical Physics*, vol. 38, no. 5, pp. 2508-2514.

Zhu, Xie, YQ, Wang, J & Xing, L 2009, 'Scatter correction for cone-beam CT in radiation therapy', *Medical Physics*, vol. 36, no. 6, pp. 2258-2268.

Zhu, Wang, J & Xing, L 2009, 'Noise suppression in scatter correction for cone-beam CT', *Medical Physics*, vol. 36, no. 3, pp. 741-752.

Appendix A Matlab Codes

This Appendix gives the listing of main files and codes written for this thesis project in Matlab. The Matlab codes are presented below with the headings (in red) describing the evaluation in each case.

1. Read/write files to read the header information using ReadHeader.m and to read the cone-beam projection files using readviv.m

%% Function to read the header information of Varian CBCT projections that are stored as *.HND files

```
function [Filename,Theta,N_rows,N_col,du,dv,SAD,SDD,IAD]=ReadHeader(fn)
fid=fopen(fn);
HND.FileType = fread(fid,32,'*char'); %Reading File Type
HND.nFileLength = fread(fid,1,'uint32');
HND.sChecksum = fread(fid,4,'char');
HND.nChecksum = fread(fid,1,'uint32');
HND.CreationDate = (fread(fid,8,'*char'));
HND.CreationTime = (fread(fid,8,'*char'));
HND.sPatientID = (fread(fid,16,'*char'));
HND.nPatientSerial = fread(fid,1,'uint32');
HND.sSeriesID = (fread(fid,16,'*char'));
HND.nSeriesSerial = fread(fid,1,'uint32');
HND.sSliceID = fread(fid,16,'*char');
HND.nSliceSerial= fread(fid,1,'uint32');
HND.SizeX = fread(fid,1,'uint32');
HND.SizeX;
HND.SizeY = fread(fid,1,'uint32');
HND.SizeY;
HND.dSliceZPos= fread(fid,1,'double');
HND.sModality = fread(fid,16,'*char');
HND.nWindow = fread(fid,1,'uint32');
HND.nLevel = fread(fid,1,'uint32');
HND.nPixelOffset = fread(fid,1,'uint32');
HND.sImageType = fread(fid,4,'*char');
HND.dGantryRtn = fread(fid,1,'double');
HND.dSAD = fread(fid,1,'double');
HND.dSFD = fread(fid,1,'double');
HND.dCollX1 = fread(fid,1,'double');
HND.dCollX2 = fread(fid,1,'double');
HND.dCollY1 = fread(fid,1,'double');
HND.dCollY2 = fread(fid,1,'double');
HND.dCollRtn = fread(fid,1,'double');
HND.dFieldX = fread(fid,1,'double');
HND.dFieldY = fread(fid,1,'double');
HND.dBladeX1 = fread(fid,1,'double');
HND.dBladeX2 = fread(fid,1,'double');
HND.dBladeY1 = fread(fid,1,'double');
HND.dBladeY2 = fread(fid,1,'double');
HND.dIDUPosLng = fread(fid,1,'double');
HND.dIDUPosLat = fread(fid,1,'double');
HND.dIDUPosVrt = fread(fid,1,'double');
```

```

HND.dIDUPosRtn = fread(fid,1,'double');
HND.dPatientSupportAngle = fread(fid,1,'double');
HND.dTableTopEccentricAngle = fread(fid,1,'double');
HND.dCouchVrt = fread(fid,1,'double');
HND.dCouchLng = fread(fid,1,'double');
HND.dCouchLat = fread(fid,1,'double');
HND.dIDUResolutionX = fread(fid,1,'double');
HND.dIDUResolutionY = fread(fid,1,'double');
HND.dImageResolutionX = fread(fid,1,'double');
HND.dImageResolutionY = fread(fid,1,'double');
HND.dEnergy = fread(fid,1,'double');
HND.dDoseRate = fread(fid,1,'double');
HND.dXRayKV = fread(fid,1,'double');
HND.dXRayMA = fread(fid,1,'double');
HND.dMetersetExposure = fread(fid,1,'double');
HND.dAcqAdjustment = fread(fid,1,'double');
HND.dCTProjectionAngle = fread(fid,1,'double');
HND.dCTNormChamber = fread(fid,1,'double');
HND.dGatingTimeTag = fread(fid,1,'double');
HND.dGating4DInfoX = fread(fid,1,'double');
HND.dGating4DInfoY = fread(fid,1,'double');
HND.dGating4DInfoZ = fread(fid,1,'double');
HND.dGating4DInfoTime = fread(fid,1,'double');
fclose(fid);
Filename=HND.FileType;
Theta=HND.dCTProjectionAngle;
N_rows=HND.SizeX;
N_col=HND.SizeY;
du=HND.dIDUResolutionX;
dv=HND.dIDUResolutionY;
SAD=HND.dSAD;
% X-ray source and detector setting
SDD = 150; %source to detector distance = 150 cm
%SAD = 100; %X-ray source to axis distance = 100 cm
IAD=HND.dIDUPosVrt;
.....
....
%% Matlab function to open viv file
function A = readviv(fn) % fn is the directory containing the VIV files
fp = fopen(fn,'r');
if (fp == -1)
    error('Cannot open viv file for reading');
end;
dd = dir(fn);
A = [];
ext = fn(end-2:end);
if (strcmpi(ext,'viv'))
    isviv = 1;
else
    disp('Not a viv file');
end;
if (dd.bytes >= 2048*1536*2)
    xres = 2048;
    yres = 1536;
else

```

```

xres = 1024;
yres = 768;
end;
hdr_size = dd.bytes - xres*yres*2; % since VIV file is 16-bit integer
fseek(fp,hdr_size,'bof');
[A,count] = fread(fp,[xres,yres],'*uint16');
fclose(fp);

```

.....
2. Pre-processing steps required to get the log ratio of intensity maps and to use adaptive filter to reduce noise with edge preserving is obtained using the function `proc_Projection.m`

%% **Matlab function for pre-processing**

```
function f = proc_Projection()
```

```
% Get the directory path containing air-scan and phantom scan viv projections for cone-beam full-fan scans
```

```
AIR_directory = '/home/medphys/.../AIR-scan-VIV/';
```

```
CBCT_directory = '/home/medphys/.../VIV_DIR_NEW/';
```

```
fa = dir([AIR_directory,'*.viv']);
```

```
fc = dir([CBCT_directory,'*.viv']);
```

```
N_proj = 370; % number of projections
```

```
isdown = 0; % flag for down sampling
```

```
% use 'for' loop to read in all the data
```

```
for k=1:N_proj
```

```
    % get air scan data
```

```
    air = double(readviv( [AIR_directory,'/',fa(k).name] ));
```

```
    % if( isdown ~= 0 )
```

```
    %     % down sampling
```

```
    %     air = downSampling( air, 1 );
```

```
    % end;
```

```
    % get object scan data
```

```
    proj = double(readviv( [CBCT_directory,'/',fc(k).name] ));
```

```
    % if( isdown ~= 0 )
```

```
    %     % down sampling
```

```
    %     proj = downSampling( proj, 1 );
```

```
    % end;
```

```
%% Calculate logarithmic ratio of object scan to air scan projections
```

```
logP = -log(min(max(proj./air,0),1));
```

```
logP(isnan(logP)) = 0; % equate any nans to zero
```

```
logP(isinf(logP)) = 0; % equate any infinities to zero
```

```
% apply 2D adaptive wiener filter for edge preserve smoothing
```

```
if( isdown ~= 0 )
```

```
    logP = wiener2( logP, [3 3] );
```

```
else
```

```
    logP = wiener2( logP, [5 5] );
```

```
end;
```

```
end;
```

```
% Save the pre-processed log image as mat file in the mentioned directory
```

```
rs = strcat( '/home/medphys/.../', num2str(k), '.mat' );
```

```
save( rs, 'logP' );
```

```
return;
```

```
% Down sampling function to reduce the projection size if required
```

```
function Q = downSampling( P, flag )
```

```
if( flag ~= 0 )
```

```

Q = (P(1:2:end, 1:2:end) + P(1:2:end, 2:2:end) + P(2:2:end,1:2:end)+P(2:2:end,2:2:end))/4;
else
Q = P(1:2:end, 1:2:end);
end;
return;

```

.....

3. Files containing the core functions of CBCT reconstruction, such as, **CTRecon_Rcm.m** and **FDK.m** that includes application of Parker weights and weights for non-equal cone angles.

```

% code for CBCT reconstruction
function f = CTRecon_Rcm()

```

```

% load Header information of CBCT projections from hnd files
% save the information as mat file and load them

```

```

%load Preprocessed.mat % projection header info
proj_param = experiment.param;
% determines whether downsampling or not
isdown = 0;
% isdown = 1;
if( isdown~=0 )
% number of rows and columns of downsampled image
% is half of original size
proj_param.N_row = proj_param.N_row/2;
proj_param.N_col = proj_param.N_col/2;

% pixel size is twice of original pixel size
proj_param.du = proj_param.du*2;
proj_param.dv = proj_param.dv*2;
% u_off , v_off resetting
proj_param.u_off(:) = proj_param.N_col/2 + 0.5;
proj_param.v_off(:) = proj_param.N_row/2 + 0.5;
end;

```

```

%% For 512 X 512 reconstruction matrix

```

```

Nx = 512; % width of reconstructed image
Ny = 512; % height of reconstructed image
Nz = 158; % number of slices for catphan
NzStep = 31; % To save memory we can do in bunches
proj_param.proj1st = 1; % id of first projection file that is used for reconstruction
proj_param.N_proj = 370; % number of projection files

```

```

%% Define reconstructed volume
MinX = -12.5; MaxX = +12.5; % in cm
MinY = -12.5; MaxY = +12.5; % in cm
MinZ = -8; MaxZ = +6; % for 512 matrix
proj_param.x_size = Nx; % width of reconstructed image
proj_param.y_size = Ny; % height of reconstructed image
proj_param.z_size = Nz; % number of slices

```

```

% Construct Projection Matrices

```

```

A =
ProjectionMatrix(proj_param.theta,proj_param.du,proj_param.dv,proj_param.u_off,proj_param.v_
off,proj_param.SDD,proj_param.SAD);

```

```

% coordinates of reconstruction grid
proj_param.x = linspace( MinX, MaxX, proj_param.x_size );
proj_param.y = linspace( MinY, MaxY, proj_param.y_size );
proj_param.z = linspace( MinZ, MaxZ, proj_param.z_size );
% reconstruction filter selection
filterName = 'ram-lak'; % choice of filter

% fraction of filter window width
d = 1.0;
proj_param.Phihat = Filter( filterName, proj_param.N_col , proj_param.du, d );

%% Weighting factors for non-equal cone angles
dtheta = [proj_param.theta(2)-proj_param.theta(1) ; ( proj_param.theta(3:end)-
proj_param.theta(1:end-2) )/2 ; proj_param.theta(end)-proj_param.theta(end-1)];
dtheta_bar = mean(dtheta);
Wt = dtheta/dtheta_bar;
Wt = Wt./mean(Wt);
Wr = pi/proj_param.N_proj;
Figure(1);

% Parker weighting for data redundancy
phiFan = abs( proj_param.theta( proj_param.proj1st ) - proj_param.theta( proj_param.N_proj) );
phiFan = phiFan - 180;
Nz = length(proj_param.z);
for iz = 1:NzStep:Nz
    zidx = iz:min(iz+NzStep-1, Nz);

% memory allocation
try
    R = zeros(length(proj_param.y), length(proj_param.x), length(zidx));
    dR=R;
catch
    error('Out of Memory!');
end

for k=proj_param.proj1st:proj_param.N_proj
    k % to show progress

% calc parker weight
W = parkerW( proj_param.N_col, proj_param.u_off(k), proj_param.du,
    proj_param.SDD,abs(proj_param.theta(k) - proj_param.theta(proj_param.proj1st)),...
    phiFan );

% make parker weight matrix
W = repmat( W, [proj_param.N_row, 1] );

% get pre-processed log image from the directory
rs = strcat( '/home/medphys/...', num2str(k), '.mat' );
% This '.mat' file is obtained using 'proc_Projection.m'
load(rs);

if Wr ~= 0
    % to apply FDK
    % modified FDK function by adding Parker Weight

```

```

    dR = FDK( proj_param.x, proj_param.y, proj_param.z(zidx), proj_param.u_off(k),
proj_param.v_off(k), proj_param.du, proj_param.dv, ...
    proj_param.theta(k), logP, A(:,k), ...
    proj_param.SDD, proj_param.SAD, W, proj_param.Phihat );
    % back projection
    R = R + Wt(k) * Wr*dR; % R is the rotation matrix computed
    Cmin=min(min(min(R)));
    Cmax=max(max(max(R)));
end;
cla;
imagesc(proj_param.x,proj_param.y,R(:,round(length(zidx)/2)))
caxis([Cmin Cmax]);
colormap('gray');
pause(0.1);
end;

    % save reconstructed result
    save( '/home/medphys/.../recon.mat', 'R' );
end;
return;

%%%%%%%%%%%%%%%%%%%%%%%%%%%%%%%%%%%%%%%%%%%%%%%%%%%%%%%%%%%%%%%%%%%%%%%%
% parkerWeight
% Input:
% nu : horizontal pixel count
% u_off : horizontal offset
% du : pixel size, unit - cm
% SDD : source to detector distance, unit - cm
% theta : projection angle, unit - degree
% fan : fan width, unit - degree
%%%%%%%%%%%%%%%%%%%%%%%%%%%%%%%%%%%%%%%%%%%%%%%%%%%%%%%%%%%%%%%%%%%%%%%%

function w = parkerW( nu, u_off, du, SDD, theta, fan )
w = ones(1, nu); % make row vector
% get angle between direction of source to each pixel and central ray
phi = atan2( ((1:nu) - u_off ) * du, SDD ) * 180 / pi;
% calc parker weight for each pixel
for u=1:nu;
    if( theta + 2 * phi(u) < fan )
        w(u) = sin( pi * theta / 4 / (fan/2 - phi(u)) )^2;
    elseif( (180 - 2 * phi(u) <= theta) && ( theta <= 180 + fan ) )
        w(u) = sin( pi * ( 180 + fan - theta ) / 4 / ( fan /2 + phi(u) ) )^2;
    end;
end;
return;

.....

%% Modified FDK reconstruction function for cone-beam reconstruction ( source: from OSCaR
software package)
function dR = FDK(x,y,z,u_off,v_off,du,dv,Beta,P,A,SDD,SAD,PARKERW, varargin)
%% Inputs:
%% Beta: the projection angle which is fixed for the whole function
%% P: 2-D Matrix of size nu*nv
%% u_off, v_off: give us the farthest point from the origin of the detector in horizontal and
vertical axes respectively or detector is of size [2*u_off]*[2*v_off]}

```

```

%% du, dv: step size
%% x,y,z: The 3-D grid for reconstructing the image
%% A: Projection Matrix
%% SDD: distance from source to detector
%% PARKERW: parker weight
%% Phihat: 1-D Ramp Filter
% Dimensions of reconstruction grid
nx = length(x);
ny = length(y);
nz = length(z);
[nv,nu] = size(P);
u = (-u_off + [0:nu-1])*du;
v = (-v_off + [0:nv-1])*dv;

%% Pre-weighting factor
% [uu,vv] = meshgrid(u,v);
% weight = SDD./sqrt(SDD^2 + vv.^2 + uu.^2);

% for speed up, getWeight function is used to replace above two commented
% lines

weight = getWeight(double(SDD), u, v);
% Remark: P is over-written to conserve memory in following computations.
% The interpretation at each stage should be clear from context
P = P .* weight;
P = P .* PARKERW; % apply parker weight

%% Filtering
Phihat = varargin{1};
if ~isempty(Phihat), % Skip to backprojection if filter is empty

P = fft( P, length(Phihat), 2 ); % Rows zero-padded automatically
% Remark: This loop can likely be vectorised using repmat
for j=1:nv
    P(j,:) = P(j,:) .* Phihat ;
end;

P = real( ifft( P, [], 2 ) );
P = P(:,1:nu); % Trim zero-padding on rows
end % of if-block
% Increment to add to reconstruction in backprojection stage
dR = zeros(ny,nx,nz);

%% Vectorised computation of backprojection
% [yy, xx, zz] = ndgrid( y, x, z);
% % Use projection matrix to project reconstruction (x,y,z) grid
% % into detector (u,v) grid
% UV = A * [ xx(:); yy(:); zz(:)'; ones(1,nx*ny*nz) ];

% for speed up, getUV function is used
UV = getUV(A, x(:), y(:), z(:));
isUsingBiLinear = 1;
if (isUsingBiLinear ~= 1)
    % Nearest neighbour interpolation method is used to find detector coordinates (u,v)
    U = round( UV(1,:)./UV(3,:) ) + 1 ;

```

```

V = round( UV(2,:)./UV(3,:) ) + 1 ;
% identify indices of voxels with projections strictly within detector grid
ind = find( (U>=1) & (V>=1) & (U<=nu) & (V<=nv) );
% Remark: This will have to be changed if P is transposed
P_ind = ( U(ind) - 1 ) * nv + V(ind) ;
co = cos(Beta*pi/180);
si = sin(Beta*pi/180);
% Grid-dependent weighting factors (only computed for voxels needed)
W = ( SAD ./ ( SAD - co*xx(ind) - si*yy(ind) ) ).^2;
dR( ind ) = W .* P( P_ind );

else
%% Bi-linear interpolation to find detector coordinates (u,v) using get_dR function
dR = get_dR(SAD, Beta, UV, x(:), y(:), double(P));
end;
return % after fixing the projection angle, the routine returns the value calculated by FDK equation
for each voxel

```

.....

4. The conversion of *.mat to DICOM files using CBCT_metadata_copy.m helps write the file as DICOM with required header information.

%% To write in-house reconstructed files as dicom files along with metadata information required for exporting to TPS

```

fS=dicomreaddir('/home/medphys/.../');
[garb nooffiles]=size(fS);
for i=1:nooffiles
filenamecurrent = fS(i).name;
metadata(1,i) = dicominfo(filenamecurrent); % store all metadata
end;

```

%% To write in-house reconstructed slices as dicom images with metadata

```

for i= 1:158
L = 158;
% Parameters
mu_water = 0.2; % mu stands for linear attenuation coefficient [in cm-1]
CT_gain = 1000;
pfitfull = [ -0.000000171836907 0.001867921677187 -3.027888248800242] * 10000;
dgts=floor(log10(L))+1;
istr= num2str(i);
for j=1:dgts-(floor(log10(i))+1)
istr=strcat('0',istr);
end;
load('/home/medphys/.../recon.mat');
slicei = R(:, :, i);
maxi= max(max(slicei));
mini = min(min(slicei));
slicei = ( slicei * 1000 + 2000 );
slicei = uint16( polyval( pfitfull, slicei) );
slicei=rot90(slicei); % flip matrix up to down in order to match Varian image
filename=['/home/medphys/.../CT' istr '.dcm'];
status = dicomwrite(slicei,filename,metadata(1,159-i),'CreateMode','copy', 'WritePrivate',true);
end;

```

.....

Appendix B C++ Codes

(1) get_dR.cpp

This function is written in C++ and has one source file that use Bilinear Interpolation to find the detector coordinates

```
#include <math.h>
#include "mex.h"
#include <iostream>
#define PI 3.1415926535897932384626433832795
// Input
// SAD : source-to-axis distance
// beta : projection angle
// UV : 3 by nx*ny projected coordinate matrix
// x, y : reconstruction grid
// P : 2-D Matrix of size nu*nv
// nu, nv : size of P

// Output
// dR : nx*ny by 1 column vector

void get_dR(double SAD, double beta, double* UV, int len, double* x, double* y,
            int nx, int ny, double* P, int nu, int nv, double* dR)
{
    double co = cos(beta*PI/180.0);
    double si = sin(beta*PI/180.0);
    int N = len;

    double* cosx = new double[nx];
    double* siny = new double[ny];
    int i;
    for (i = 0; i < nx; i++)
        cosx[i] = co * x[i];
    for (i = 0; i < ny; i++)
        siny[i] = si * y[i];
    for (i = 0; i < N; i++)
    {
        int j = i * 3;
        double u = UV[j] / UV[j+2];
        double v = UV[j+1] / UV[j+2];

        if ( u < 0.5 || u >= nu || v < 0.5 || v >= nv )
            continue;
        int u1 = (int)u;
        if (u1 < 1) u1 = 1;
        int u2 = (int)u + 1;
        if (u2 > nu) u2 = nu;
        int v1 = (int)v;
        if (v1 < 1) v1 = 1;
        int v2 = (int)v + 1;
        if (v2 > nv) v2 = nv;
        int ind1 = (u1 - 1) * nv + v1 - 1;
        int ind2 = (u1 - 1) * nv + v2 - 1;
```

```

int ind3 = (u2 - 1) * nv + v1 - 1;
int ind4 = (u2 - 1) * nv + v2 - 1;

double pp;
if ( ind1 == ind4 )
    pp = P[ind1];
else if( u1 == u2 )
    pp = P[ind1] * (v2-v) + P[ind2] * (v-v1);
else if( v1 == v2 )
    pp = P[ind1] * (u2-u) + P[ind3] * (u-u1);
else
    pp = (P[ind1] * (v2-v) + P[ind2] * (v-v1) ) * (u2-u) +
          (P[ind3] * (v2-v) + P[ind4] * (v-v1) ) * ( u-u1);
int ix = (i % ( nx*ny)) / ny;
int iy = (i % ( nx*ny)) % ny;
// mexPrintf("ix=%d\tnx=%d\n", ix, nx);
// mexPrintf("iy=%d\tny=%d\n", iy, ny);
double W = ( SAD / ( SAD - cosx[ix] - siny[iy] ) );
dR[i] = W * W * pp;
}
delete[] cosx;
delete[] siny;
return;
}
void mexFunction(int nlhs, mxArray *plhs[], int nrhs, const mxArray *prhs[] )
{
double SAD; double beta; double* UV; double* x; double* y; int nx, ny; double* P; int nu,nv;
double* dR;
/* Check for proper number of arguments */
if (nrhs != 6)
{ mexErrMsgIdAndTxt("MATLAB:mexcpp:nargin",
    "This function requires 6 input arguments."); }
else if (nlhs >= 2)
{ mexErrMsgIdAndTxt("MATLAB:mexcpp:nargout",
    "This function requires 1 output argument.");}
SAD = mxGetScalar(prhs[0]);
beta = mxGetScalar(prhs[1]);
UV = (double*) mxGetPr(prhs[2]);
x = (double *) mxGetPr(prhs[3]);
y = (double *) mxGetPr(prhs[4]);
P = (double *) mxGetPr(prhs[5]);
nx = mxGetM(prhs[3]);
ny = mxGetM(prhs[4]);
int len = mxGetN(prhs[2]);
nv = mxGetM(prhs[5]);
nu = mxGetN(prhs[5]);
int ndim = 3;
int dim[3] = { ny, nx, len / ny / nx };
plhs[0] = mxCreateNumericArray(ndim, dim, mxDOUBLE_CLASS, mxREAL);
dR = (double*)mxGetPr(plhs[0]);
get_dR(SAD, beta, UV, len, x, y, nx, ny, P, nu, nv, dR);
return;
}
.....

```

(2) getUV.cpp

This function is written in C++ and has one source file that is used to project reconstruction grid of size (x,y,z) into detector grid of size (u,v)

```
#include <math.h>
#include "mex.h"
// Input
// A : a 3 by 4 projection matrix
// x, y, z : nx by 1, ny by 1 and nz by 1 column vector
// Output
// UV : 3 by nx*ny projected coordinate matrix
```

```
void getUV(double* A, double* x, double* y, double* z, int nx, int ny, int nz, double* UV)
{
    int ix, iy, iz, k;
    int count = 0;
    int indUV = 0;
    double(*Ax)[3] = new double[nx][3];
    double(*Ay)[3] = new double[ny][3];
    double(*Az)[3] = new double[nz][3];

    // pre-calculation of A[k]x[ix]
    for (ix = 0; ix < nx; ix++)
        for (k = 0; k < 3; k++)
            Ax[ix][k] = A[k] * x[ix];

    // pre-calculation of A[k]y[iy]
    for (iy = 0; iy < ny; iy++)
        for (k = 0; k < 3; k++)
            Ay[iy][k] = A[k+3] * y[iy];

    // pre-calculation of A[k]z[iz]
    for (iz = 0; iz < nz; iz++)
        for (k = 0; k < 3; k++)
            Az[iz][k] = A[k+6] * z[iz];
    for (iz = 0; iz < nz; iz++)
        for (ix=0; ix<nx; ix++)
            for (iy = 0; iy<ny; iy++)
                for (k = 0; k < 3; k++, indUV++)
                    UV[indUV] = Ax[ix][k] + Ay[iy][k] + Az[iz][k] + A[k+9];
    delete[] Ax;
    delete[] Ay;
    delete[] Az;
    return;
}
```

```
void mexFunction(int nlhs, mxArray *plhs[], int nrhs, const mxArray *prhs[])
{
    double* A;
    double* x;
    double* y;
    double* z;
    double* UV;
    int nx, ny, nz;
    /* Check for proper number of arguments */
    if (nrhs != 4) {
```

```

mexErrMsgIdAndTxt("MATLAB:mexcpp:nargin",
    "This function requires 4 input arguments.");
} else if (nlhs >= 2) {
    mexErrMsgIdAndTxt("MATLAB:mexcpp:nargout",
        "This function requires 1 output argument.");
}

A = (double *) mxGetPr(prhs[0]);
x = (double *) mxGetPr(prhs[1]);
y = (double *) mxGetPr(prhs[2]);
z = (double *) mxGetPr(prhs[3]);
nx = mxGetM(prhs[1]);
ny = mxGetM(prhs[2]);
nz = mxGetM(prhs[3]);
plhs[0] = mxCreateDoubleMatrix((mwSize)3, (mwSize)nx*ny*nz, mxREAL);
// int ndim = 3;
// int dim[3] = {ny, nx, nz};
// plhs[0] = mxCreateNumericArray(ndim, dim, mxDOUBLE_CLASS, mxREAL);
UV = mxGetPr(plhs[0]);
getUV(A, x, y, z, nx, ny, nz, UV);
return;
}

```

.....

(3) getWeight.cpp

This function is written in C++ and has one source file that is used to compute FDK preweighting factors for cone-beam projections before filtration step

```

#include <math.h>
#include "mex.h"
void getWeight(double SDD, int nu, int nv, double* u, double* v, double* W)
{
    int i, j;
    int count = 0;
    double SDD2 = SDD * SDD;
    double* u2 = new double[nu];
    double* v2 = new double[nv];
    for (i = 0; i < nu; i++)
        u2[i] = u[i] * u[i];
    for (j = 0; j < nv; j++)
        v2[j] = v[j] * v[j];
    for (i = 0; i < nu; i++)
    {
        for (j = 0; j < nv; j++)
        {
            W[count] = SDD / sqrt(SDD2 + u2[i] + v2[j]);
            count++;
        }
    }
    delete[] u2;
    delete[] v2;
    return;
}
void mexFunction(int nlhs, mxArray *plhs[], int nrhs, const mxArray *prhs[])
{
    double SDD;

```

```

size_t nu, nv;
double* u;
double* v;
double* w;
/* Check for proper number of arguments */
if (nrhs != 3) {
    mexErrMsgIdAndTxt("MATLAB:mexcpp:nargin",
        "getWeight requires 3 input arguments.");
} else if (nlhs >= 2) {
    mexErrMsgIdAndTxt("MATLAB:mexcpp:nargout",
        "getWeight requires 1 output argument.");
}
if ((mxGetN(prhs[1]) != 1) || (mxGetN(prhs[2]) != 1)) {
    mexErrMsgIdAndTxt("MATLAB:mexcpp:nargin",
        "getWeight requires input argument of column vector.");
}

SDD = mxGetScalar(prhs[0]);
nu = mxGetM(prhs[1]);
nv = mxGetM(prhs[2]);
u = (double *) mxGetPr(prhs[1]);
v = (double *) mxGetPr(prhs[2]);
plhs[0] = mxCreateDoubleMatrix((mwSize)nv, (mwSize)nu, mxREAL);
w = mxGetPr(plhs[0]);
getWeight(SDD, nu, nv, u, v, w);
return;
}

```

.....

.....

Srinivasan, K., Mohammadi, M. & Shepherd, J. (2014) Applications of linac-mounted kilovoltage cone-beam computed tomography in modern radiation therapy: a review.
Polish Journal of Radiology, v. 79, pp. 181-193

NOTE:

This publication is included on pages 158-170 in the print copy of the thesis held in the University of Adelaide Library.

It is also available online to authorised users at:

<http://doi.org/10.12659/PJR.890745>

Srinivasan, K., Mohammadi, M. & Shepherd, J. (2013) Cone beam computed tomography for adaptive radiotherapy treatment planning.
Journal of Medical and Biological Engineering, v. 34(4), pp. 377-385

NOTE:

This publication is included on pages 172-180 in the print copy of the thesis held in the University of Adelaide Library.

It is also available online to authorised users at:

<http://doi.org/10.5405/jmbe.1372>

Srinivasan, K., Mohammadi, M. & Shepherd, J. (2014) Investigation of effect of reconstruction filters on cone-beam computed tomography image quality.
Australasian Physical and Engineering Science in Medicine, v. 37(3), pp. 607-614

NOTE:

This publication is included on pages 182-189 in the print copy of the thesis held in the University of Adelaide Library.

It is also available online to authorised users at:

<http://doi.org/10.1007/s13246-014-0291-8>